STRUCTURAL AND PHYSICAL PROPERTIES

OF THE $La_{1-x}TiO_3$ SYSTEM

STRUCTURAL AND PHYSICAL PROPERTIES OF THE $La_{1-x}TiO_3$ SYSTEM

BY

MARLENE J. MACEACHERN, B.Sc.

A Thesis

Submitted to the School of Graduate Studies

in Partial Fulfillment of the Requirements

for the Degree

Master of Science

McMaster University

September 1993

MASTER OF SCIENCE 1993 MCMASTER UNIVERSITY
(Chemistry) Hamilton, Ontario

TITLE: Structural and Physical Properties of the $La_{1-x}TiO_3$ System

AUTHOR: Marlene J. MacEachern, B.Sc.(UPEI)

SUPERVISOR: Professor J.E. Greedan

NUMBER OF PAGES: xiv, 142

Abstract

Compounds in the series $La_{1-x}TiO_3$ have been prepared in the powder and single crystalline forms. The structures of these compounds were studied with x-ray, neutron, and electron diffraction techniques. In all cases, a distortion from the ideal perovskite structure was found.

Throughout the series, transitions occur in structural, magnetic, and electrical properties. The structure of $La_{.67}TiO_3$ was found to be of a distorted perovskite type arising from distortions in the titanium octahedra as a result of an ordering of the lanthanum positions and A-site cation vacancies. Although this phase has been reported many times, the crystal structure has not been determined. The $La_{.67}TiO_3$ and $La_{.70}TiO_3$ phases have the same structure and were assigned to the Pmmn space group. At $La_{.75}TiO_3$, a Ti^{3+} concentration of 28%, the symmetry of the structure changes from Pmmn to Imma, and distortion of the perovskite structure is caused by octahedral tilting within the lattice. A further structural transition occurs at a Ti^{3+} concentration of 64%, $La_{.88}TiO_3$, where the symmetry changes from Imma to Pnma. Again distortions from the ideal perovskite structure are caused by

octahedral tilts within the system.

Transitions were also observed in electrical and magnetic properties. These transitions occur at the same Ti^{3+} concentrations as the transitions observed in the structural properties, which suggests a correlation between properties based on Ti^{3+} concentration.

The occurrence of A-site cation vacancies within the lattice is directly related to the Ti^{3+} concentrations within the individual materials. Changes in the Ti^{3+} concentration affect the size of the unit cell as well as the electrical and magnetic properties which range from insulators at low Ti^{3+} concentrations to metals at high Ti^{3+} concentrations.

Acknowledgements

I would like to thank my supervisor, Dr.J.E.Greedan for his encouragement, help, and understanding. I am greatful for all of the support and assistance he has given me in the past two years.

I would like to thank Dr. James F. Britten for invaluable help with obtaining and understanding the x-ray data. I would also like to thank Jim, his wife Debbie, and his children, Nicole, Andrew, and Kelly for the friendship and trust they have shown me.

Thank you to Hania Dabkowski, Wenhe Gong, and Jim Garrett for helping me obtain samples to analyze. Thank you also to Bruce Collier and H.Frank Gibbs for technical assistance.

I would like to thank Dr. Guo Liu for all of his help when teaching me new things, and all of his patience when I wasn't so quick to learn. I would also like to thank Dr. Jacques Barbier, Dr. Ragu Nandyala, Abdul Nakua, Edmond Fok, Byron DeLaBarre, Gisele Amow, and Rob Hammond for useful and enlightening conversations.

Thank you goes out to the friends I have made during my time in Hamilton. A special thank you to Lisa Chao, Stephanie Palerme, and Theresa Fauconnier for always knowing where to find cheesecake, and to Andreas Decken and Luc Girard for their help and great friendship.

I would also like to thank my parents, Mary and Eldon, and my brother, Ian, for all the support they have given me right from the very beginning.

A special thank you to Mark P. Walker for believing in me when I had almost lost belief in myself, and most importantly for his support, friendship, and love.

Table of Contents

List of Tables

List of Figures

Chapter 1

Introduction

The family of perovskite compounds is large and quite well known. The $SrTiO_3$ structure is described as the ideal perovskite structure with a cubic cell edge of a_o = 3.905Å and belonging to the space group Pm3m. The structure contains cubic close packed oxygen ions with strontium cations in place of one fourth of the oxygen ions. The titanium cations occupy one fourth of the octahedral holes in the cubic close packed array of oxygen and strontium which are not adjacent to the strontium cations. The final structure is made up of corner shared strings of TiO_6 octahedra extending infinitely in three dimensions. The TiO_6 octahedra have perfect 90° angles and six equal titanium-oxygen bonds of 1.952Å.

The conventional choice for assignment of atomic positions within the cubic unit cell is to place titanium on the origin. A strontium is assigned to the body center in a pseudo-body-centered arrangement of metal cations. The oxygens occupy the centers and edges of the cubic unit cell so that there are twelve equidistant oxygens from the central

strontium cation, Figure 1.[1]

Recent studies on the $LaTiO_3$ structure, once believed to be a cubic perovskite, have shown that the actual structure is of the $GdFeO_3$ type, Figure 2.[2] This structure arises from an orthorhombic distortion of the ideal perovskite type structure.[3,4,5,6] The $LaTiO_3$ structure has been assigned to the Pbnm space group with reported unit cell parameters being a = 5.633(10)Å, b = 5.614(9)Å, c = 7.940(8)Å and a cell volume of 251.1(9)Å^3.[7]

Early reports on the $LaTiO_3$ system doped with basic cations report the unit cells as cubic perovskite.[8,9,10] However, a later study by Sunstrom et al.[11] shows that doping of the $La_{1-x}TiO_3$ system with strontium cations does change the structure. Addition of Sr^{2+} changes the Ti^{3+} concentration present in the compound, and in turn changes in symmetry throughout the series are observed.

At a Ti^{3+} concentration of 26%, $La_{.2}Sr_{.8}TiO_{2.97}$, a transition in symmetry is observed from Pm3m to Imma. A further transition from Imma to Pbnm is observed for a Ti^{3+} at approximately 80%, $La_{.74}Sr_{.31}TiO_{3.02}$. The observed unit cell parameters are given in Table 1.1.

The magnetic properties are also altered when the $La_{1-x}TiO_3$ system is doped with strontium cations. As the symmetry increases with a decreasing level of Ti^{3+}, the d_{xy}, d_{yz}, and d_{xz}

Table 1.1 Unit cell parameters for $La_{1-x}Sr_xTiO_3$ reported by Sunstrom et al.[11]

x	a(Å)	b(Å)	c(Å)	Vol.(Å^3)
0.00	5.629(2)	5.612(1)	7.915(1)	250.02(12)
0.05	5.601(3)	5.595(1)	7.912(1)	247.91(12)
0.10	5.592(5)	5.581(2)	7.900(2)	246.56(23)
0.20	5.586(4)	5.568(3)	7.885(3)	245.04(24)
0.30	5.577(5)	5.555(3)	7.961(3)	243.52(24)
0.40	5.575(1)	5.555(1)	7.842(1)	242.72(7)
0.50	5.573(1)	5.542(1)	7.827(2)	241.74(8)
0.60	5.561(1)	5.536(1)	7.824(2)	240.86(8)
0.70	5.552(1)	5.529(2)	7.814(2)	239.74(9)
0.80	3.9079(6)			59.68(3)
0.90	3.9064(6)			59.61(4)
1.00	3.9056(6)			59.57(3)

orbitals become degenerate (t_{2g}) and there is a drop in the magnitude of the temperature dependent susceptibilities. This is consistent with a narrow band (d_{xy}) in the case of the Pbnm structure and a wider band (t_{2g}) in the Pm3m case.

$LaTiO_3$, 100% Ti^{3+}, was found to be a canted ferromagnet and $La_{.95}Sr_{.05}TiO_3$, 95% Ti^{3+}, was found to have a net ferromagnetic moment below 150K. The susceptibilities were found to be temperature independent in the temperature range 150K to 300K. All of the other compounds showed temperature independent magnetism from 160K to 300K, where samples with a Ti^{3+} concentration below 50% showed paramagnetism in the lower temperature range.

The electrical properties for the strontium doped $LaTiO_3$ system of Sunstrom et al.[11] were varied. Compounds with a Ti^{3+} concentration greater than 36% were metallic, and those with a Ti^{3+} concentration of 16% were semiconducting. The point at which the transition occurs from a semiconductor to a metal was found to be 26%.

Studies on the $La_{1-x}Ba_xTiO_3$ system have been similar to those done on the strontium doped system. Early reports on the barium doped system involve cubic perovskite structures for all of the compounds involved.[12] Later reports have identified the unit cells as being of a distorted perovskite structure with unit cells parameters comparable to those found for the

Table 1.2 Unit cell assignments for $La_{1-x}Ba_xTiO_3$ (Sunstrom et al.)[13]

Compound	Ti^{3+} (%)	a(Å)	b(Å)	c(Å)	Vol(Å^3)
$La_{.10}Ba_{.90}TiO_3$	10	3.985(1)			63.29(5)
$La_{.20}Ba_{.80}TiO_3$	20	3.981(1)			63.09(4)
$La_{.30}Ba_{.70}TiO_3$	30	3.968(2)			62.47(7)
$La_{.40}Ba_{.60}TiO_3$	40	5.590(1)	5.661(5)	7.932(3)	250.98(37)
$La_{.50}Ba_{.50}TiO_3$	50	5.578(4)	5.629(3)	7.920(1)	248.67(21)
$La_{.60}Ba_{.40}TiO_3$	60	5.595(2)	5.590(2)	7.921(2)	247.75(29)
$La_{.70}Ba_{.30}TiO_3$	70	5.588(1)	5.589(1)	7.913(2)	247.30(19)
$La_{.80}Ba_{.20}TiO_3$	80	5.592(2)	5.587(3)	7.891(2)	246.58(15)
$La_{.90}Ba_{.10}TiO_3$	90	5.599(2)	5.586(1)	7.895(3)	246.90(21)
$La_{.95}Ba_{.05}TiO_3$	95	5.593(3)	5.570(3)	7.903(5)	247.25(25)

Table 1.3 Unit cell assignments for $La_{1-x}Ba_xTiO_3$ (Eylem et al.)[14]

Compound	Ti^{3+} (%)	a(Å)	b(Å)	c(Å)	Vol(Å^3)
$La_{.15}Ba_{.85}TiO_3$	15	3.985(3)			63.28(7)
$La_{.20}Ba_{.80}TiO_3$	20	3.984(1)			63.24(2)
$La_{.33}Ba_{.67}TiO_3$	33	3.976(2)			62.85(5)
$La_{.40}Ba_{.60}TiO_3$	40	3.965(2)			62.33(5)
$La_{.50}Ba_{.40}TiO_{2.9}$	50	3.955(2)			61.86(5)
$La_{.60}Ba_{.30}TiO_{2.9}$	60	3.954(2)			61.82(5)
$La_{.70}Ba_{.20}TiO_{2.9}$	70	3.944(2)			61.35(5)
$La_{.85}Ba_{.15}TiO_3$	85	5.598(4)	5.601(6)	7.918(8)	248.26(39)
$La_{.90}Ba_{.10}TiO_3$	90	5.592(2)	5.592(3)	7.914(6)	247.47(21)

distorted persovskite structure of $LaTiO_3$.[7,13,14] The unit cell assignments for the individual studies are given in Tables 1.2 and 1.3.

In the $La_{1-x}Ba_xTiO_3$ system of Sunstrom et al.[13], there are two structural transitions noted. The first transition occurs at a Ti^{3+} concentration of 80%. At this point, the orthorhombic symmetry moves from Pbnm to Ibmm. The second transition occurs at a Ti^{3+} concentration of 30%, where the symmetry is changed from the orthorhombic Ibmm to the cubic Pm3m symmetry.

Transitions in magnetic properties coincide with structural transitions based on Ti^{3+} concentration. The magnetic ordering found for $LaTiO_3$ is lost at the structural change between orthorhombic symmetries at a Ti^{3+} concentration of 80%. There was an increase in the room temperature magnetic susceptibility of $La_{.30}Ba_{.70}TiO_3$, which was consistent with the shift to cubic symmetry found at this Ti^{3+} concentration of 30%.

From the reports of Eylem et al.[14], there are two structural transitions in the system. The first transition occurs at a Ti^{3+} concentration around 15%. At this point there is change in symmetry from P4mm to Pm3m. The second transition occurs at a Ti^{3+} concentration between 70% and 85%, where the symmetry changes from the cubic Pm3m to orthorhombic Pbnm.

Four probe resistivity measurements showed metallic conductivities for a majority of the compounds in the temperature range 300K to 4K. Room temperature resistivities were in the range of 10^{-2} and 10^{-4} Ωcm. When the Ti^{3+} concentration was below 20%, the samples showed properties of semiconductors and insulators.

The magnetic ordering of $LaTiO_3$ is destroyed at a composition of $La_{.95}Ba_{.05}TiO_3$, Ti^{3+} concentration of 95%. The compounds in the series are found to have Pauli paramagnetism where the data can be fit by the Curie-Weiss Law,

$$\chi = \chi_o + C/(T-\theta)$$

where χ_o is the temperature independent magnetic susceptibility.

The purpose of this study is to look at the structure and properties of the $LaTiO_3$ system doped with A-site cation vacancies as compared with those results found for the strontium and barium doped systems.

Compounds in the series $La_{1-x}TiO_3$ have been prepared by various groups,[15,16,17,18,19,20] but a definitive structural characterization has not been carried out except for $LaTiO_3$.[7]

The first report of $La_{.67}TiO_3$ was made by G.H. Jonker and N.V. Philips in a private communication to Michael Kestigan and Roland Ward.[15] The structure was said to be of a deformed perovskite type, but no structural characterization was given.

In 1955, Kestigan and Ward[15] prepared a series of compounds, $La_{.67+x}TiO_3$ with x ranging from 0.03 to 0.33 by the equation;

$$(1/3 + x/2)La_2O_3 + (3/2x)Ti_2O_3 + (1-3x)TiO_2 = La_{(.67+x)}TiO_3$$

The compounds of this series were all found to be of the cubic perovskite type as determined from x-ray diffraction analysis on prepared powders. The unit cell parameters are given in Table 1.4. It was found that the unit cell size increased with increasing lanthanum content and density measurements indicated that there was one $La_{.67+x}TiO_3$ unit per unit cell. A sample in this series was obtained which corresponded to $La_{.67}TiO_3$. The x-ray diffraction pattern was complex and was not interpreted.

Table 1.4 Unit cell parameters for $La_{1-x}TiO_3$ as reported by Kestigan and Ward.[15]

x	a(Å)	Vol.(Å^3)
0.00	3.926(2)	60.51(5)
0.08	3.918(2)	60.14(5)
0.18	3.904(2)	59.50(5)
0.24	3.896(2)	59.14(5)
0.30	3.888(2)	58.77(5)

In 1974, Abe and Uchino prepared $La_{.67}TiO_3$ in a powder form.[16] From the x-ray data, a cell was determined to be of the perovskite type which was distorted to orthorhombic symmetry and involved a doubling of the unit cell along the c-axis. A structural model was proposed which called for an ordered arrangement of the A-site vacancies along the c-axis. Abe and Uchino report the unit cell parameters as a=3.869Å, b=3.882Å, and c=7.782Å, but no detailed structure was proposed.

Single crystals of $La_{.67}TiO_3$ were prepared by Yokoyama et al. in a KF-Borax flux.[19] The crystals obtained were of two symmetry groups, cubic and tetragonal. The reported cubic crystals were obtained above 1000°C with a=3.880(1)Å, and the tetragonal crystals were obtained below 1000°C with $a = \frac{1}{2}c =$ 3.881(1)Å. Both the cubic and tetragonal crystals were of the perovskite type. Structures were not determined from x-ray analysis on either of the crystal types. Superstructure lines were observed from x-ray diffraction for the crystals grown below 1000°C. The predominant superstructure line was found at a 2θ value of 11.34° and was indexed to $(00\frac{1}{2})$. From the x-ray data, no distortions in the structures were found and the doubling of the c-axis to produce the tetragonal crystals was not explained.

The perovskite type $La_{.67}TiO_3$ crystals were formed by a coprecipitation reaction by Sych et al.[17] The crystals obtained

were orthorhombic with a = 4.06Å, b = 4.11Å, and c = 8.00Å. The cell parameters reported here are larger than those of previous references. The increase in cell parameters was attributed to the openness and rigidity of the $La_{.67}TiO_3$ lattice obtained by moderate heating of the coprecipitated hydroxides.

Electron diffraction measurements reported did not include the superstructure line attributed to the doubling of the c-axis, but the recorded lines were indexed based on its existence. Sych et al. attributed the superstructure of the distorted perovskite to an alternation of filled and vacant layers of the cubo-octahedra along the c-axis, but again a detailed structure for $La_{.67}TiO_3$ was not reported.

Compounds of variable composition $La_{⅔+x}TiO_3$ were prepared and studied with x-ray diffraction by Bazuev et al.[18] The compounds $La_{.70}TiO_3$, $La_{.80}TiO_3$, $La_{.90}TiO_3$, and $La_{.95}TiO_3$ were prepared in the powder form from sintering of La_2O_3, TiO_2, and Ti_2O_3 at 1400°C for 48 hours. The unit cell parameters were assigned as given in Table 1.5.

Table 1.5 Cell parameters as determined by Bazuev et al.[18]

Composition	Unit Cell Paramters, Å
$La_{.70}TiO_3$	3.888
$La_{.80}TiO_3$	3.904
$La_{.90}TiO_3$	3.928
$La_{.95}TiO_3$	3.963

The increase in the unit cell parameters was thought to be dependent upon the oxygen content of each compound. Although x-ray diffraction studies were carried out on each compound, results were not published and no structural assignments were made.

The analogous system containing Ce^{3+}, $Ce_{\frac{2}{3}+x}TiO_3$ was also studied by Bazuev et al. The compound $Ce_{.67}TiO_3$ in this series was observed as having a doubled c-axis, and was assigned an orthorhombic unit cell with a = 3.586(2)Å, b = 3.877(2)Å, and c = 7.754(5)Å. Published x-ray data for $Ce_{.67}TiO_3$ shows the observed superstructure line responsible for the assignment of the unit cell.

The superstructural reflections of $Ce_{.67}TiO_3$ were believed to arise from an ordered arrangement of the vacancies in the rare earth metal sublattice. The proposed structure of this compound, with the doubled c-axis, can be achieved by the alternation, along the c-axis, of layers consisting of cubo-octahedra completely filled by Ce^{3+} ions and layers of partly filled cubo-octahedra. Although this structure is proposed, no evidence was reported to confirm the structure.

Work done by Lichtenberg et al. reports that $LaTiO_{3+x}$ compounds were prepared from the following reaction;[20]

$$\tfrac{1}{2}\ La_2O_3 + (\tfrac{1}{2}-x)\ TiO + (\tfrac{1}{2}+x)\ TiO_2 \longrightarrow LaTiO_{3+x}$$

The series of compounds were reported to have a decrease in

unit cell volume for increasing x values. This seems unreasonable because the excess oxygen would be interstitial since the perovskite structure contains no empty sites large enough to accommodate the O^{2-} anions. It has been proposed by Crandles[21] that Lichtenberg et al. have prepared samples with lanthanum vacancies rather than excess oxygen. This would explain the observed decrease in unit cell volume. By transforming the compounds from the oxygen excess model of Lichtenberg et al. to the lanthanum vacancy model of Crandles, based on thermogravimetric analysis, selected compounds can be rewritten as given in Table 1.6.

The structural data reported by Lichtenberg et al.[20] involves two transition points like those described previously. It was reported that a change from a monoclinic unit cell to a mixture of orthorhombic and 2D layered monoclinic cells was observed at a Ti^{3+} concentration of 21%. A second transition was observed from the mixture of orthorhombic and 2D layered monoclinic cells to a single phase of the orthorhombic cell at a Ti^{3+} concentration of 57%. The unit cell parameters reported are given in Table 1.7.

Table 1.7 Unit cell parameters for $LaTiO_{3+x}$ as reported by Lichtenberg et al.[20]

Compound	a(Å)	b(Å)	c(Å)	β(°)
$LaTiO_{3.5}$	7.80	5.55	13.0	98.6
$LaTiO_{3.4}$	7.86	5.53	13.5	97.2
$LaTiO_{3.2}$	5.56	5.55	7.87	
$LaTiO_{3.0}$	5.62	5.61	7.91	

Table 1.6 Conversion table for oxygen excess model of Lichtenberg et al.[20] to lanthanum vacancy model of Crandles.[21]

$LaTiO_{3+x}$	Ti^{3+}(%)	$La_{1-x}TiO_3$
$LaTiO_{3.50}$	0	$La_{.67}TiO_3$
$LaTiO_{3.45}$	10	$La_{.70}TiO_3$
$LaTiO_{3.40}$	19	$La_{.73}TiO_3$
$LaTiO_{3.35}$	28	$La_{.76}TiO_3$
$LaTiO_{3.30}$	40	$La_{.80}TiO_3$
$LaTiO_{3.25}$	49	$La_{.83}TiO_3$
$LaTiO_{3.20}$	61	$La_{.87}TiO_3$
$LaTiO_{3.15}$	70	$La_{.90}TiO_3$
$LaTiO_{3.10}$	79	$La_{.93}TiO_3$
$LaTiO_{3.05}$	91	$La_{.97}TiO_3$
$LaTiO_{3.00}$	100	$LaTiO_3$

Electrical resistivity measurements done on this system show transitions as well. When the Ti^{3+} concentration is below 45%, the compounds are found to be semiconductors. At approximately 45% there is a semiconductor-metal transition. Compounds with a Ti^{3+} concentration greater than 46% have metallic like properties up until the Ti^{3+} concentration reaches 84%. At this point a second transition occurs from a metallic state to a semiconducting state. Above 84%, the compounds are semiconductors.

Magnetic susceptibility measurements were made on compounds with a Ti^{3+} concentration greater than 15%. The compounds between 20% and 80% were reported to have a complex behavior which was not reported nor explained. The compounds with a Ti^{3+} concentration greater than 80% were found to have temperature independent regions with paramagnetism showing up in the lower temperature ranges.

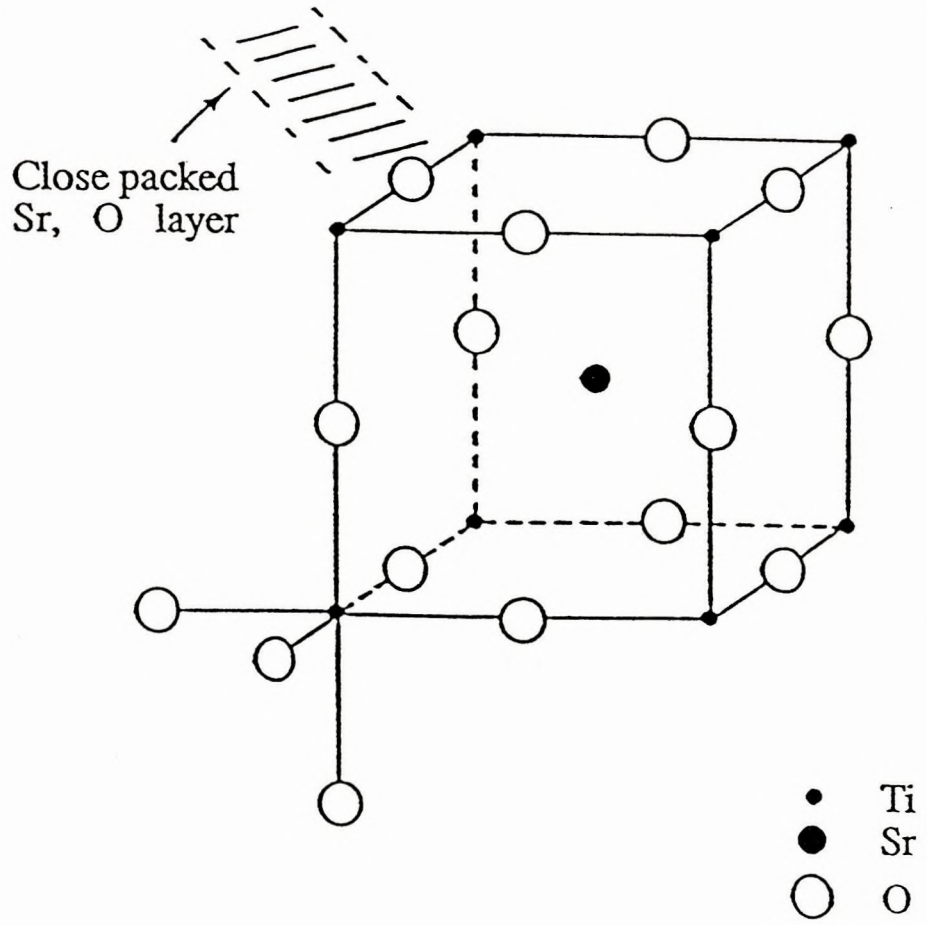

Figure 1.1 Ideal perovskite structure of $SrTiO_3$

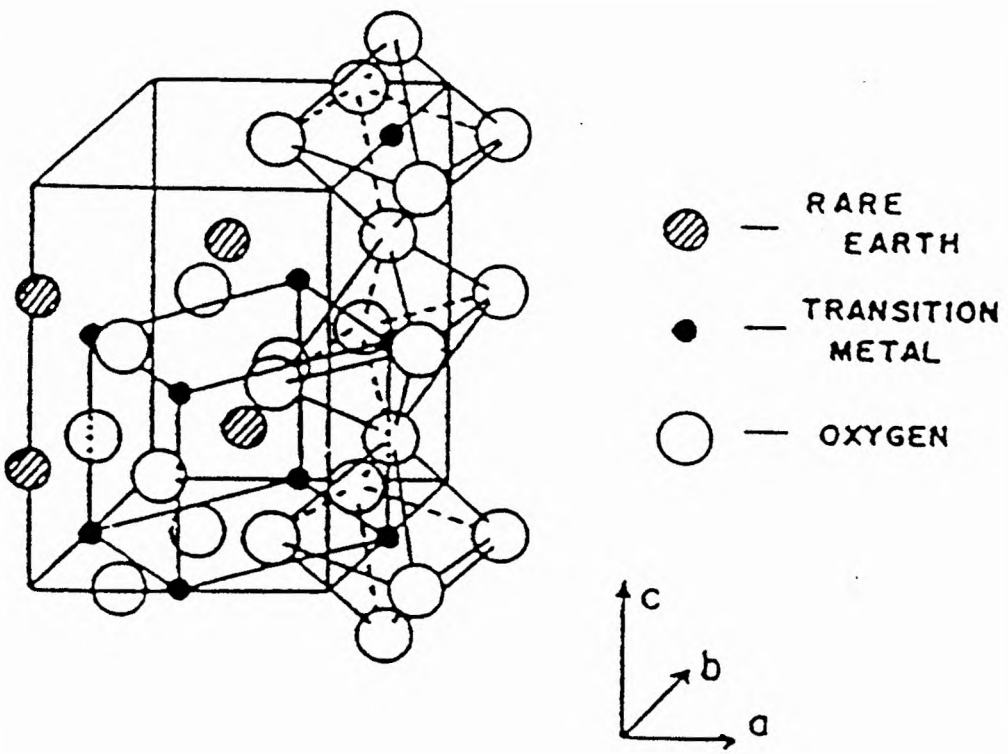

Figure 1.2 $GdFeO_3$ structure

Chapter 2

Description of Experiments

2.1 Sample Preparation

2.1.1 $La_{.67}TiO_3$ Powder

The starting materials for the preparation of $La_{.67}TiO_3$ were La_2O_3 and TiO_2. The La_2O_3 was fired at 900°C for 24 hours to remove any hydroxides or carbonates that may be present.

The La_2O_3 and TiO_2 were weighed in a stoichiometric ratio of 1:3. The mixture was well ground in acetone with a agate mortar and pestle. After evaporating the acetone, approximately 11 grams of the powder were pressed into half inch diameter pellets, each containing 2 to 3 grams of sample. The pellets were then placed into a covered alumina crucible and heated to 1430°C for one hour. After cooling, the inner portions of the sample were grey in color while the outer portions of the pellets were yellow. The grey sections

indicated that some of the sample may have been reduced during the heating process.

The entire sample was reground in acetone and pressed into pellets of the same size as described previously. The pellets were heated to a temperature of 1400°C for one hour. Again upon cooling, the inner portions of the pellets were grey in color while the outer regions remained yellow. Another attempt was made at reheating the sample. The third firing was done at a lower temperature in order to keep the sample from reducing. The sample was heated to 1390°C for one hour. This firing allowed the complete oxidation of the powder to yield the $La_{.67}TiO_3$ phase which was uniformly yellow in color.

$$La_2O_3 + 3\ TiO_2 \longrightarrow La_2Ti_3O_9$$

2.1.2 $La_{.70}TiO_3$

The starting materials for the preparation of $La_{.70}TiO_3$ were La_2O_3, Ti_2O_3, and TiO_2. The La_2O_3 was fired at 900°C for 24 hours to remove any hydroxides or carbonates that might be present. The Ti_2O_3 was analyzed by thermogravimetric analysis (TGA) to determine the actual composition. TGA results showed the actual composition to be $Ti_2O_{3.024}$. This composition was used when calculating the required quantities of the starting materials.

In order to achieve a product with the proper oxidation state, a mixture of Ti^{3+} and Ti^{4+} had to be used. It was

previously established by a co-worker that the remaining oxygen pressure in the evacuated chamber of the furnace was enough to oxidize some of the Ti^{3+} present in the mixture. Therefore, it was necessary to add an excess of $Ti_2O_{3.024}$ in the range of 30%.

The starting materials were mixed according to the following reaction scheme in order to have the required excess of $Ti_2O_{3.024}$.

$$.35\ La_2O_3 + .065\ Ti_2O_{3.024} + .87\ TiO_2 \longrightarrow La_{.70}TiO_3$$

The mixture was ground in acetone with an agate mortar and pestle. After evaporation of the acetone, the powder was pressed into a one inch diameter pellet containing approximately 12 grams of sample. The pellet was then sectioned into four pieces and each piece was placed into a molybdenum crucible and covered with a ZrN disk. The crucible was mounted inside an RF induction heating furnace and the reaction chamber was evacuated to 3×10^{-4} mmHg. The sample was heated by induction to 1250°C for 18 hours. When cooled, the sample was dark grey which indicated that a partial reduction had occurred. A second firing of the sample at 1300°C was carried out in a sealed molybdenum crucible for 12 hours. The sample was heated in a Lindberg 54322 tube furnace under an argon atmosphere. This firing yielded the dark grey single phase $La_{.70}TiO_3$ product.

2.1.3 $La_{.75}TiO_3$

The starting materials for the preparation of $La_{.75}TiO_3$ were the same as those used for the preparation of $La_{.70}TiO_3$. The reactants were weighed out according to the following scheme, taking into account that an excess of Ti^{3+} had to be added to compensate for the oxidation taking place inside the reaction chamber of the furnace.

$$.375\ La_2O_3 + .17\ Ti_2O_{3.024} + .66\ TiO_2 \longrightarrow La_{.75}TiO_3$$

The sample mixture was prepared in the same way as that of the $La_{.70}TiO_3$. The pellets were heated by induction in the RF furnace for one hour at a temperature of 1470°C under a vacuum of 4×10^{-4} mmHg.

When the sample was cooled, the Guinier pattern showed a slight impurity phase in the product. A second grinding and firing at a temperature of 1465°C under a 2.5×10^{-4} mmHg vacuum for one hour yielded a black single phase product which was identified as $La_{.75}TiO_3$ by Guinier analysis.

2.1.4 $La_{.80}TiO_3$, $La_{.88}TiO_3$, and $La_{.92}TiO_3$ Powders

The preparations of $La_{.80}TiO_3$, $La_{.88}TiO_3$, and $La_{.92}TiO_3$ were carried out by a coworker. In each case, the starting materials used were La_2O_3, TiO_2, and $Ti_2O_{3.024}$. The La_2O_3 was fired to 900°C for 24 hours to remove any hydroxides or carbonates present. The preparations for these products is the same as

outlined previously for the other samples. The starting materials were ground in acetone and the powder mixtures were pressed to pellets. The pellets were placed in a molybdenum crucibles and heated by induction under the conditions outlined in the Tables 2.1a and 2.1b.

Each product was analyzed by Guinier powder diffraction and each was determined to be single phase. The products were all black in color which indicated that a reduction had occurred in each product.

The ratios of starting materials used are given in the following reactions for the preparations of each of the products.

$$.40\ La_2O_3 + .28\ Ti_2O_{3.024} + .45\ TiO_2 \longrightarrow La_{.80}TiO_3$$

$$.44\ La_2O_3 + .43\ Ti_2O_{3.024} + .15\ TiO_2 \longrightarrow La_{.88}TiO_3$$

$$.46\ La_2O_3 + .50\ Ti_2O_{3.024} \longrightarrow La_{.92}TiO_3$$

2.1.5 $La_{.67}TiO_3$ Single Crystals

Single crystals of $La_{.67}TiO_3$ were grown by Hania Dabkowski using a flux method. The composition used was similar to that used by Yokoyama et al.[19]

The starting materials were weighed, mixed, and placed in a $20cm^3$ platinum crucible with a close fitting lid. The best

Table 2.1a Conditons for the preparations of $La_{.80}TiO_3$, $La_{.88}TiO_3$, and $La_{.92}TiO_3$ during the first firing.

Compound	Temp.(°C)	Pressure(mmHg)	Time(Hours)
$La_{.80}TiO_3$	1480	3×10^{-4}	1.1
$La_{.88}TiO_3$	1470	3×10^{-4}	1.0
$La_{.92}TiO_3$	1450	1×10^{-4}	2.0

Table 2.1b Conditions for the preparations of $La_{.80}TiO_3$, $La_{.88}TiO_3$, and $La_{.92}TiO_3$ during the second firing.

Compound	Temp.(°C)	Pressure(mmHg)	Time(Hours)
$La_{.80}TiO_3$	1500	3×10^{-4}	1.1
$La_{.88}TiO_3$	1480	3×10^{-4}	1.0
$La_{.92}TiO_3$	1420	1×10^{-4}	2.0

results were obtained when the starting composition was:

TiO_2 = 2.4 grams

La_2O_3 = 1.6 grams

KF = 13.4 grams

$Na_2B_4O_7$ = 4.0 grams

The mixture was heated in a 1000°C furnace for 48 hours. The weight loss was high, on the order of 20%. Rectangular, yellow crystals were formed on the walls of the crucibles. Removal of these crystals was difficult due to the hardness of the crystals. The crystals that were separated were portions of larger single crystals which were broken due to the removal process.

2.1.6 $La_{.75}TiO_3$ Single Crystals

The $La_{.75}TiO_3$ single crystal was grown from the $La_{.75}TiO_3$ powder sample. A single crystal of approximately $0.3cm^3$ was produced from a tri-arc melting technique conducted by Mr.Jim Garrett.[22]

2.1.7 $La_{.80}TiO_3$ Single Crystal

The $La_{.80}TiO_3$ single crystal was grown from the $La_{.80}TiO_3$ powder sample. A single crystal of approximately $0.5cm^3$ was produced from a tri-arc melting technique conducted by Mr. Jim Garrett.[22]

2.2 Instrumentation

2.2.1 Guinier Powder Diffraction

An IRDAB model XDC 700 Guinier-Haag camera was used for initial analyses of the powder samples.

This diffraction technique uses a bent single crystal of quartz between the Cu x-ray source and the sample. The orientation of this crystal is adjusted as to diffract the incident x-ray beam and convert it to a convergent beam. As a result, the focussed beam is very intense and monochromatic, with only the $CuK_{\alpha 1}$ radiation being used. By using such a radiation beam, the result is excellent resolution of the lines in the diffraction pattern, and exposure times are kept to a minimum, generally between ten minutes and one hour.

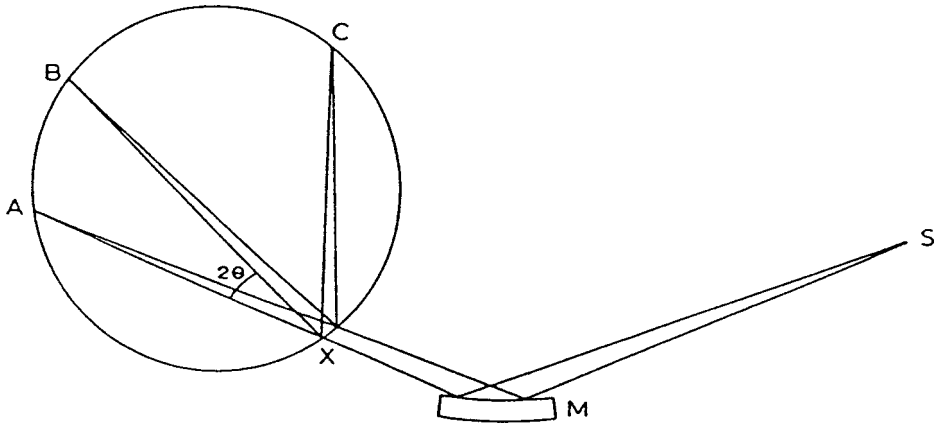

Figure 2.1 Schematic for Guinier-Haag camera

After beam convergence, the monochromatic radiation passes through the sample at X, Figure 2.1.[23] Radiation that is not diffracted by the sample comes into focus at A, where 2θ

= 0°. At this point a beamstop is placed in front of the film to keep the film from blackening. Other diffracted beams become focussed at various positions along the film (B&C). Since A, B, C, and X must all lie on a circle, a piece of film approximately 2×18 cm is placed inside the cassette to lie on this circle forming a cylinder. The scale of the film is linear in 2θ, where $2\theta = 0$ corresponds to the undiffracted beam at A which is used as a reference point on the film.

The length of the arc AB = $2\times2\theta\times r$, where r is the radius of the film cylinder with a value of 50.20mm. Therefore, the diffraction angle $2\theta = 180\times AB/2\pi r = 0.573\times AB°$. The maximum diffraction angle for the Guinier-Haag camera is 90° in 2θ.

Sample preparation for Guinier analysis involved placing a finely ground sample powder with a small amount of silicon powder onto a piece of transparent tape. The tape was then attached to a small metal disk which was mounted onto the sample holder of the camera. Typical exposure times were 40 to 60 minutes.

The diffraction lines present on the film were then measured for position and intensity with a KEJ Instruments, model LS20, line scanner. This scanner uses a laser with λ=950nm to detect the diffraction lines present on the film. Since the scanner is computer automated, a digital file with the diffraction data is created.

The obtained data were then entered into a program called

SCANPI to calculate accurate d-spacings. The measured lines were assigned values based on the positions of six reference lines obtained through the use of an internal silicon standard. Cell constants were refined by a least squares unit cell refinement and indexing program called LSUDF. This program uses a proposed cell and tries to expand the set of indexed reflections by a least squares refinement.

2.2.2 Diffractometer Powder Data Collection

A Nicolet I2 automated diffractometer was used to collect x-ray powder diffraction data. This diffractometer used $CuK_{\alpha 1}$=1.5406Å and $CuK_{\alpha 2}$=1.5448Å radiation. The diffraction data were collected over the range $8° \leq 2\theta \leq 90°$.

The diffraction data were then refined with the x-ray version of the Rietveld Profile Refinement program DBWS 9600PC.[24]

2.2.3 Diffractometer Single Crystal Data Collection

Single crystal x-ray diffraction data were collected on a Seimen's PV/3 automated diffractometer. This diffractometer uses $AgK_{\alpha 1}$ = 0.56086Å. Data were collected over a range of $3° \leq 2\theta \leq 110°$ for the $La_{.67}TiO_3$ sample and over a range of $3° \leq 2\theta \leq 80°$ for the $La_{.75}TiO_3$ sample. The data from each collection were indexed and refined with the aid of SHELXTL PC Release 4.1, a compilation of computer programs used for structure solution and refinement.

2.2.4 Single Crystal Precession

A Charles Supper Company, USA, model 3310 precession camera was used for the single crystal diffraction measurements on $La_{.67}TiO_3$ and $La_{.75}TiO_3$. The radiation used was $MoK_{\alpha 1}$, with λ=0.70926Å. The distance between the film and the crystal was 60mm for the zero level diffraction patterns. A 20mm radius screen and 30° precession angle were used to obtain the zero layer precession photographs.

The lattice constants were calculated by measuring the distance in millimeters between adjacent reciprocal lattice points on the film. For more accurate measurements, distances between n points can be used.

$$d^* = 1/(CF \times \lambda)$$

where d^* = reciprocal lattice constant

l = distance between reciprocal lattice points in mm

CF = crystal to film distance = 60mm

λ = wavelength of the radiation = 0.70926Å

Therefore,

$$d^* = 1(mm)/(60mm \times 0.70926Å)$$

$$d = 42.56/1 = \text{cell constant in Å}$$

The remaining cell constants can be obtained by collecting the diffraction patterns of the upper layers of diffraction spots. This is done by moving the film closer to the crystal and obtaining a new pattern. The cell constants are calculated in

the same way as shown above.

2.2.5 Electron Diffraction

A Philips CM-12 transmission electron microscope (TEM) was used to collect the electron diffraction pattern of a single crystal $La_{.67}TiO_3$ sample.

This technique makes use of the wave properties of electrons. Because the scattering efficiency of electrons is high, small samples can be used whereas in x-ray analysis the sample sizes have to be much larger.[23]

During the analysis, electrons are emitted from a tungsten filament and accelerated through a high voltage, 50 to 100 Kv. The wavelength of the emitted electrons is related to the accelerating voltage, v, by;[23]

$$\lambda = h(2mev)^{-1/2}$$

where m = the mass of the electron

e = the charge of the electron.

Electrons are focussed by an electric or magnetic field, usually an electromagnetic lens or condenser lens. The electron beam then passes through the sample which is placed on a graphite disk. The beam travels through a series of lenses, objective,intermediate,and projector to form a magnified image of the sample on a fluorescent screen, Figure 2.2.[23]

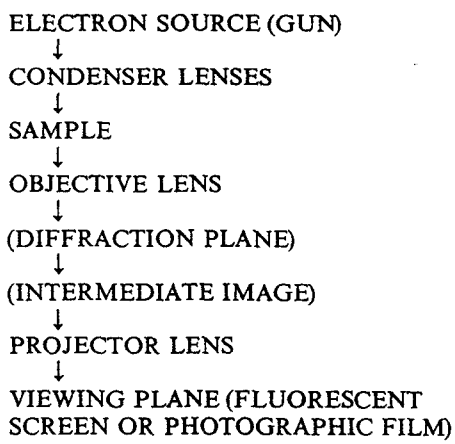

Figure 2.2 Basic components of a transmission electron microscope.

Changing the relative position of the viewing screen causes the diffraction pattern of the sample to become focussed and photographs of the diffraction pattern or image can be taken.

2.2.6 Powder Neutron Diffraction

Powder neutron diffraction studies were carried out at the McMaster University Nuclear Reactor.

Radiation obtained from the (200) reflection of a copper single crystal monochromator, giving a neutron wavelength of 1.3925Å was used for the data collection. The diffracted neutron beams were detected with a position sensitive detector (PSD) which is capable of detecting scattered neutrons over

32° in 2θ.

Data were collected in a series of frames, each covering a range of 20° to 25°. A typical data set consisted of five frames and the maximum scattering angle was approximately 120° in 2θ. The acquisition time for each frame was on the order of eight hours.

A thin walled vanadium can was used to contain the sample during the diffraction experiment. The can was 8mm in diameter and filled with approximately 8 grams of sample to a total volume of 1.5cm^3. All of the data were collected at room temperature under a vacuum of $\approx 10^{-3}$ Torr.

Data were refined using a version of the Rietveld Profile Refinement program DBWS 9600PC.

2.2.7 Magnetic Susceptibility

Magnetic susceptibility measurements were carried out on a Quantum Design superconducting quantum interference device (SQUID) magnetometer. All of the samples were sintered pellets with a typical sample size of 200mg. Susceptibility measurements were taken in the temperature range of 5K to 300K with an applied magnetic field strength of 2000 Oe.

2.2.8 Electrical Resistivity

Electrical resistivity measurements were taken on a number of samples. All of the samples except $La_{.80}TiO_3$ were sintered rectangular pellets with a typical sample height of

0.8 cm. The $La_{.80}TiO_3$ sample was a cylindrical single crystal with a height of 0.85cm.

All the measurements were taken by a four probe Van der Pauw method in the temperature range of 300K to 5K by lowering the sample into a dewar of liquid helium.

Chapter 3

Structure Determination

3.1 Basic Diffraction Theory

Diffraction of x-rays by crystals was discovered by Max von Laue in 1912. In the same year, W. L. Bragg noticed the similarity of diffraction to ordinary reflection and deduced a simple equation in which he treated diffraction as reflection from planes of a lattice.[25]

The Bragg approach regards crystals as being built up in layers or planes such that each acts as a semi transparent mirror. Some x-rays are reflected off a plane at an angle equal to the angle of incidence. The rest are transmitted to be reflected off succeeding planes.

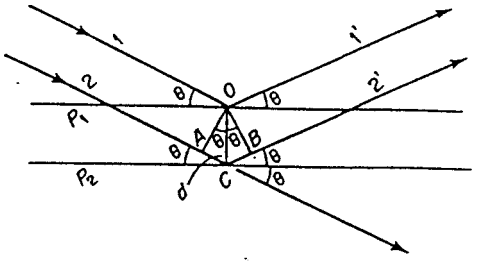

Figure 3.1 Bragg's Law

Two x-ray beams, 1 and 2, are reflected from adjacent planes, A and B, Figure 3.1.[25] Beam 22′ has to travel the extra distance, xyz, as compared to the beam 11′. In order for 1′ and 2′ to be in phase the distance xyz must be equal to a whole number of wavelengths. The perpendicular distance between pairs of adjacent planes is the d-spacing, d. This d-spacing and the angle of incidence or Bragg angle, θ, are related to the distance, xy, by;

$$xy = yz = d\sin\theta$$

$$xyz = 2d\sin\theta \quad \text{and} \quad xyz = n\lambda$$

Therefore:

$$n\lambda = 2d\sin\theta$$

When the Bragg condition is satisfied, the reflected beams are in phase and interfere constructively. By rewriting Bragg's Law to;

$$\sin\theta = n\lambda/2 * (1/d)$$

we see that $\sin\theta$ is inversely proportional to d, the interplanar spacing.

Therefore, by measuring the deviation of the diffracted beam from the incident beam, we can determine the spacing between planes in the crystal. In turn, cell constants and angles can be determined.[23]

The von Laue equations are derived from a simple static atomic model of a crystal system and provide a more general

approach to diffraction than Bragg.[26]

This approach sees the crystal as being composed of identical microscopic objects such as sets of atoms or ions. These objects are placed at sites R in a Bravais lattice where they reradiate the incident radiation in all directions.[26] At wavelengths and directions for which the rays scattered from all the lattice points interfere constructively, sharp peaks arise. Therefore, a condition must be found where constructive interference exists.

Consider two scatterers separated by a displacement vector **d**. If an x-ray beam approaches from a direction **n** with a wavelength λ, a wave vector, **k**, can be assigned where $\mathbf{k} = 2\pi\mathbf{n}/\lambda$. If the path difference between the rays scattered by each of the two objects is an integral number of wavelengths, a scattered ray will be observed in a direction **n**′ with a wavelength λ. A wave vector for the scattered ray can then be given as;

$$\mathbf{k}' = 2\pi\mathbf{n}'/\lambda$$

The path difference can then be written as,

$$d*\cos\theta + d*\cos\theta' = \mathbf{d}\bullet(\mathbf{n}-\mathbf{n}')$$

The condition for constructive interference then becomes

$$\mathbf{d}\bullet(\mathbf{n}-\mathbf{n}') = m\lambda \quad \text{for integral } m.$$

Rewriting yields a condition on the incident and scattered wave vectors.

$$\mathbf{d}\bullet(\mathbf{k}-\mathbf{k}') = 2\pi m \quad \text{for integral } m$$

Now this has been applied to an array of scatterers at sites of a Bravais lattice. For the condition of constructive interference to hold for the array, it must hold simultaneously for all values of **d** that are Bravais lattice vectors, **R**, since the lattice sites are displaced from one another by the Bravais lattice vectors, **R**,[26]

$$\mathbf{R}\bullet(\mathbf{k}-\mathbf{k}') = 2\pi m$$

for integral m and all Bravais lattice vectors **R**. Equivalently; $e^{i(\mathbf{k}-\mathbf{k}')\bullet\mathbf{R}} = 1$ for all Bravais lattice vectors, **R**. If we call **K** a reciprocal lattice vector equal to the change in the wave vectors, $\mathbf{K} = (\mathbf{k}-\mathbf{k}')$ then,

$$e^{i\mathbf{K}\bullet\mathbf{R}} = 1$$

Because the incident and scattered rays have the same wavelength, **k** and **k**′ have the same magnitude. Therefore, **k** and **k**′ make the same angle, θ, with the plane perpendicular to the reciprocal lattice vector **K**. The scattering can be viewed as a Bragg reflection, with the Bragg angle, θ, for the family of direct lattice planes perpendicular to the reciprocal lattice vector **K**. Therefore, von Laue's formulation is equivalent to Bragg's Law.[26]

If a Bragg peak is associated with a reciprocal lattice vector, **K**, the path difference between the rays scattered at $\mathbf{d}_i$ and $\mathbf{d}_j$ can be written as;

$$\mathbf{K}\bullet(\mathbf{d}_i-\mathbf{d}_j)$$

and the phase difference can be represented by the factor;

$$\exp(i\mathbf{K}\bullet(\mathbf{d}_i-\mathbf{d}_j)).$$

The net amplitude of the rays scattered can be found by summation of the factors to which all of the various **d** values for the array contribute.[26]

$$F = \Sigma\exp(i\mathbf{K}\bullet\mathbf{d}_j)$$

This summation is referred to as the geometrical structure factor. For polyatomic crystals, the atomic scattering factors, f_o, should be considered. The overall structure factor becomes;

$$F = \Sigma f_o \exp(i\mathbf{K}\bullet\mathbf{d}_j)$$

where $\mathbf{K}\bullet\mathbf{d}_j$ = the phase with respect to the origin of the unit cell.[26] This can be rewritten to express the phasing in terms of the Miller indices, hkl, and the fractional atomic positions.[23]

$$F = \Sigma f_o \exp(i*2\pi(hx_j + ky_j + lz_j))$$

When dealing with scattering factors, thermal motion must also be considered. The effect of such thermal motion is to spread the electron density over a large volume and thus to cause the scattering power of the real atom to fall off more rapidly than that of the ideal or stationary model. The change in scattering power can be given by;[23]

$$\exp(-2\beta(\sin^2\theta/\lambda^2)$$

The proper scattering factor for a real atom should then be given as;

$$f_j = f_o \exp(-2\beta(\sin^2\theta/\lambda^2)$$

Extending this to the entire array, the structure factor becomes;

$$F = \Sigma f_j \exp(i*2\pi(hx_j + ky_j + lz_j)$$

$$= \Sigma f_o \exp(i*2\pi(hx_j + ky_j + lz_j) \exp(-2\beta(\sin^2\theta/\lambda^2)$$

Although the structure factor can not be measured directly, it is proportional to the square root of the intensity of the scattered rays.[23]

$$I = |F|^2$$

Measurements of the relative intensity can be made and in turn these provide information about the structure factors. If enough information is available, the positions of the atoms within a unit cell can be determined.

Neutron diffraction follows the same principles. Differences occur in the calculation of the structure factors. The structure factor for a non-magnetic material may be given by;

$$F = \Sigma b_j \exp(2\pi i(hx_j + ky_j + lz_j) \exp(-2\beta_j \sin^2\theta/\lambda^2)$$

where b_j is the neutron coherent scattering length of the atom j derived from the mean scattering power of the element, averaged over all of the isotopes and spin orientations.[27]

Electron diffraction principles are the same as those for

x-ray and neutron diffraction. The scattering factors for electron diffraction are given by;[27]

$$f_e = 2\ me^2/h^2\ ((Z-f)/|s|^2)$$

$$\approx (me^2\lambda^2/2h^2\theta^2)\ (Z-f)$$

where $(Z-f)/\theta^2$ = the scattering factor of an atom for electrons,

f = the x-ray scattering factor in electron units, and

m = the mass of the electron.

Therefore, the structure factor used in electron diffraction is;

$$F = \Sigma(me^2\lambda^2/2h^2\theta^2)\ (Z-f_j)\ \exp(2\pi i(hx_j + ky_j + lz_j))\exp(-2\beta_j\sin^2\theta/\lambda^2)$$

where Z = the total number of electrons in atom j

f_j = the scattering factor from x-ray diffraction.

3.2 Profile Analysis

The primary objective of profile fitting is to fit a numerical function, specifically referred to as a profile shape function, to a measured diffraction pattern. These profile shape functions are typically described by three parameters; the line position, $(2\theta_k)$, the peak or integrated line intensity, (I_o), and the line width expressed as the full width at half of the maximum intensity, (FWHM or H_k).[28]

To insure that the differences between measured and

calculated patterns are minimized, an optimization algorithm is used. It is necessary for the profile shape function to accommodate asymmetry and it should be applicable over the entire angular range of the instrument. A profile shape function should utilize angle dependent shape related parameters that vary smoothly as a function of angle.[28] These parameters should reflect the characteristics of the instrument and the sample. The shape related parameters should allow the profile width to be expressed in terms of a full width at half maximum to afford compatibility with previous profile and sample characteristics, i.e. crystallite size and strain.

Rietveld developed a technique for fitting a diffraction pattern with a profile shape function (PSF).[29] For a model of the diffracted line intensity and profile shape function for neutron data, the following equation was employed;[30]

$$I_{ik} = tS_k^2 j_k L_k \, 2(\ln 2)^{1/2}/H_k \exp[-4\ln 2((2\theta_i - 2\theta_k)/H_k)^2]$$

where I_{ik} = the intensity at the i^{th} point in the pattern due to the k^{th} line

t = the stepwidth of the detector

$S_k^2 = F_k^2 + J_k^2$, the sum of the nuclear and magnetic structure factors

j_k = the multiplicity of the k^{th} reflection

L_k = the Lorentz factor

$2\theta_k$ = the calculated Bragg angle

$2\theta_i$ = the angle at the i^{th} point in the pattern, and

H_k = the full width at half maximum intensity for the reflection.

To simplify things, let $I_k = tS_k^2 j_k^2 (\ln 2)^{1/2}/H_k$

and $c_k = 4\ln 2/H_k^2$.

The profile shape function can then be written as;

$$I_{ik} = I_k \exp[-c_k(2\theta_i - 2\theta_k)^2]$$

Therefore, the profile shape function is a Gaussian function having an amplitude, I_k, calculated from the structure. The shape of the Gaussian profile is matched to an observed reflection whose line positions are fixed by the lattice parameters.[28]

Slight asymmetry of the line shape can be accommodated with a modification accounting for the vertical divergence of the neutrons from the source.[28]

$$I_{ik} = I_k \exp[-c_k(2\theta_i-2\theta_k)^2] \; [1-P(2\theta_i-2\theta_k)^2 \; S/\tan\theta_k]$$

where P = the asymmetry parameter and

S = +1, 0, or -1 if $(2\theta_i-2\theta_k)$ is +'ve, 0, or -'ve respectively.

The variation of the breadth of the neutron diffraction line profile with scattering angle can be represented as;

$$H_k^2 = U\tan^2\theta_k + V\tan\theta_k + W.$$

Now the angular dependence of the line width is a function of

the parameters U, V, and W.[31]

The primary goal of the Rietveld refinement technique is to obtain values for the structure related parameters, i.e. positions, occupancies, and thermal parameters of individual atoms.[28]

The most statistically meaningful indicator of a calculated to an observed pattern fit is R_{wp}.[28]

$$R_{wp}=[\Sigma[w(2\theta_i)\times(I(2\theta_i)_{obs}-I(2\theta_i)_{calc})^2]/\Sigma[w(2\theta_i)\times(I(2\theta_i)_{obs})^2]]^{1/2}$$

The weighting parameter, $w(2\theta_i)$, is used to reduce the contribution to the error due to the misfit between the calculated and the observed patterns at the tops of the peaks. In contrast, the misfit of the regions near the tails will contribute significantly. Therefore it is not unusual to observe discrepancies near the tops of the peaks and better fits near the tails of the profiles.[28]

To gauge the quality of the fit, a comparison should be made between the final R_{wp} value and the expected error value. The expected error value is derived from the statistical error associated with the measured intensities.

$$R_{exp} = [(N-P)/\Sigma I(2\theta_i)]^{1/2}$$

where N = the number of observations

P = the number of variable parameters

The denominator contains the sum of the observed intensities. Therefore, the higher the intensity in the range

being analyzed, the lower the expected error.

The calculation of the goodness-of-fit (GOF) parameter includes the number of variables undergoing refinement. The GOF may help in determining whether a change in the number of parameters, e.g. a change to a profile shape function having a different number of parameters, or the addition of another line to a peak group, has significantly decreased the residual error.[28] The GOF is calculated from the following equation;

$$GOF = [\Sigma[w(2\theta_i) \times (I(2\theta_i)_{obs} - I(2\theta_i)_{calc})^2]/(N-P)]^{1/2}.$$

3.3 Structure Solutions

3.3.1 $La_{.67}TiO_3$ Powder

The $La_{.67}TiO_3$ powder sample was analyzed for oxygen content by thermogravimetric analysis (TGA). The increase in weight of the sample was measured while heating the sample in air to 800°C. The actual composition of the sample was then determined to be $La_{.67}TiO_{3.00}$ as calculated from an observed weight gain of 0%.

A Guinier powder pattern was taken of the $La_{.67}TiO_3$ sample. Comparing the observed pattern with a recorded pattern of $LaTiO_3$, there is a noticeable difference in the number and position of diffraction peaks. The $La_{.67}TiO_3$ sample no longer has the symmetry present in the $LaTiO_3$ compound. The

diffraction line at the d-spacing value of 7.755Å was evidence to believe that the cell had similar unit cell parameters, but a reduction in symmetry from Pbnm.

The lines of the Guinier diffraction pattern were refined and indexed in an orthorhombic space group Pmnm, Table 3.1, based on the results obtained from the single crystal, Section 3.3.6. The refined cell parameters are given in Table 3.40. This model was derived from the same type of orthorhombic distortion of the perovskite structure where $a \approx c \approx \sqrt{2}a_o$ and $b \approx 2a_o$, where a_o is the unit cell edge of an ideal cubic perovskite structure.[7]

Neutron diffraction experiments on the $La_{.67}TiO_3$ powder sample also showed evidence for a distorted perovskite structure. Reitveld refinement of the powder pattern was successful in the orthorhombic space group Pmnm. The refined cell parameters found for this proposed cell are given in Table 3.41, and compare well with those found from Guinier analysis. Refined atomic positions and temperature factors are given in Table 3.2, and compare well with those found for the single crystal x-ray diffraction refinement for $La_{.67}TiO_3$ found in Table 3.30. The bond angles and distances calculated from neutron diffraction results show that distortions arise from misalignments in the oxygen positions, Tables 3.3 and 3.4.

The powder x-ray diffraction pattern was also taken on the

Table 3.1 Observed and calculated Guinier powder patterns of $La_{.67}TiO_3$ in Pmnm.

D_{obs}	D_{calc}*	HKL
7.755	7.759	0 1 0
3.463	3.462	1 1 1
2.742	2.740	1 2 1
2.238	2.239	2 2 0
1.946	1.940	0 4 0
1.936	1.935	2 0 2
1.585	1.583	2 4 0
1.581	1.582	0 4 2
1.444	1.440	1 5 1
1.372	1.371	2 4 2
1.367	1.365	0 0 4
1.230	1.227	1 6 1
1.228	1.225	4 0 2
1.225	1.224	3 2 3
1.222	1.222	2 0 4
1.157	1.156	3 5 1
1.119	1.119	4 4 0

* a=5.482(1)Å, b=7.759(3)Å, c=5.461(1)Å

Table 3.2 Atomic positions refined from $La_{.67}TiO_3$ neutron diffraction data in Pmnm.

Atom	x	y	z	B(Å^2)	occ†
La1 (2a)	¼	-.5169(17)	¼	.735(64)	.123(2)
La2 (2a)	¼	.0048(14)	¼	.735(64)	.210(3)
Ti1 (2b)	¼	.2516(30)	¾	1.12(10)	.2500
Ti2 (2b)	¼	-.2564(28)	¾	1.12(10)	.2500
O1 (8g)	.012(1)	-.233(1)	-.516(1)	1.63(6)	1.00
O2 (2b)	¼	-.0088(21)	¾	1.96(20)	.2500
O3 (2b)	¼	-.4876(13)	¾	.21(12)	.2500

R-p = 6.34%
R-wp = 8.37%
R-exp = 2.70%
R-Bragg = 10.16%

† occ = occupation *(site multiplicity/general point multiplicity)

Table 3.3 Bond distances calculated from neutron diffraction refinement results for $La_{.67}TiO_3$ in Pmnm.

Bond	Distance(Å)	Multiplicity
La1 - O1	2.861(12)	4×
La1 - O1	2.817(11)	4×
La1 - O3	2.7400(20)	2×
La1 - O3	2.7367(15)	1×
La1 - O3	3.0584(14)	1×
La2 - O1	2.596(10)	4×
La2 - O1	2.703(10)	4×
La2 - O2	2.7325(17)	2×
La2 - O2	2.7367(15)	1×
La2 - O2	3.0583(14)	1×
Ti1 - O1	1.926(6)	4×
Ti1 - O2	2.02(3)	1×
Ti1 - O3	2.02(3)	1×
Ti2 - O1	1.960(6)	4×
Ti2 - O2	1.92(3)	1×
Ti2 - O3	1.795(24)	1×

Table 3.4 Bond angles calculated from neutron diffraction results for $La_{.67}TiO_3$ in Pmnm.

Bonds	Angle
La1-O1-La2	95.7(3)
La1-O3-La1	170.5(6)
La2-O2-La2	175.6(8)
Ti1-O2-Ti2	179.9(0)
Ti1-O3-Ti2	180.0(0)
O2-Ti1-O3	179.9(0)
O2-Ti2-O3	179.9(0)
O1-Ti1-O2	85.7(7)
O1-Ti2-O2	84.7(7)
O1-Ti1-O3	94.3(7)
O1-Ti2-O3	95.3(7)

$La_{.67}TiO_3$ sample with the Nicolet I2 powder x-ray diffractometer. The pattern observed here can also be indexed on the orthorhombic unit cell with cell parameters of a = 5.468(1)Å, b = 7.778(1)Å, and c = 5.467(1)Å with a cell volume of 232.51(6)$Å^3$.

A listing of the atomic positions and temperature factors can be found in Table 3.5. The errors listed are standard deviations calculated from a least squares refinement. Strong correlations between parameters make the refinement of those parameters difficult due to fluctuations in the least squares cycles. The least squares refinement will not converge if the correlations between parameters are too strong. To counteract the effects of the correlations, parameters were refined individually. This process leads to an underestimate of the actual errors involved. Therefore, the errors listed in the tables for the refinement in the space group Pmmn are based on individual refinements for each parameter and represent the case where no strong correlations would exist.

The x-ray data obtained also showed a small impurity. Peaks arising from this impurity were excluded from the refinement. Excluded peaks are marked as such on the refinement profile. The impurity phase was not identified. The calculated bond distances and angles are given in Tables 3.6 and 3.7.

Table 3.5 Atomic parameters for $La_{.67}TiO_3$ in Pmnm based on powder x-ray diffraction.

Atom	x	y	z	B(Å^2)	occ.
La1(2a)	¼	-.5000(36)	¼	1.09(6)	.106(1)
La2(2a)	¼	.0020(15)	¼	1.09(6)	.241(2)
Ti1(2b)	¼	.2687(15)	¾	1.43(10)	.2500
Ti2(2b)	¼	-.2706(14)	¾	1.43(10)	.2500
O1(8g)	.029(4)	-.2415(15)	-.529(4)	.94(25)	1.000
O2(2b)	¼	-.0071(154)	¾	2.41(71)	.2500
O3(2b)	¼	-.5042(57)	¾	.80(58)	.2500

R-p = 9.15%
R-wp = 12.41%
R-exp = 4.93%
R-Bragg = 12.30%

Table 3.6 Bond distances calculated from x-ray powder diffraction refinement results for $La_{.67}TiO_3$ in Pmnm.

Bond	Distance(Å)	Multiplicity
La1 - O1	2.64(3)	4×
La1 - O1	2.95(3)	4×
La1 - O3	2.7337(8)	2×
La1 - O3	2.7342(8)	1×
La1 - O3	3.0568(7)	1×
La2 - O1	2.551(19)	4×
La2 - O1	2.850(20)	4×
La2 - O2	2.734(3)	2×
La2 - O2	2.7343(18)	1×
La2 - O2	3.0569(16)	1×
Ti1 - O1	1.958(22)	4×
Ti1 - O2	2.15(12)	1×
Ti1 - O3	1.77(5)	1×
Ti2 - O1	1.959(22)	4×
Ti2 - O2	2.05(12)	1×
Ti2 - O3	1.82(5)	1×

Table 3.7 Bond angles calculated from x-ray powder diffraction results for $La_{.67}TiO_3$ in Pmnm.

Bonds	Angle
La1-O1-La2	97.6(9)
La1-O3-La1	178.6(20)
La2-O2-La2	178(5)
Ti1-O2-Ti2	180.0(0)
Ti1-O3-Ti2	180.0(0)
O2-Ti1-O3	180.0(0)
O2-Ti2-O3	180.0(0)
O1-Ti1-O2	83.8(5)
O1-Ti2-O2	84.4(5)
O1-Ti1-O3	92.6(5)
O1-Ti2-O3	96.6(5)

3.3.2. $La_{.70}TiO_3$ Powder

The $La_{.70}TiO_3$ sample was analyzed for oxygen content by TGA. The increase in weight of the sample was measured while heating the sample in air to 800°C. The composition of the sample was then determined to be $La_{.70}TiO_{3.005}$ calculated from an observed weight gain of 0.37%. The expected weight gain for the sample was 0.41%.

The Guinier powder diffraction results are very similar to those obtained from the $La_{.67}TiO_3$ powder sample. The same lines were present in the diffraction pattern with the only difference being the spacing between lines. The lines of the $La_{.70}TiO_3$ sample had larger d-spacing values as a result of increased cell parameters. Since the structure contains an increased level of lanthanum and therefore Ti^{3+}, the cell edges must expand to accommodate the increased volume. As compared with the proposed model for $La_{.67}TiO_3$, the unit cell volume was increased by approximately 1% for the $La_{.70}TiO_3$ sample.

The cell was indexed and refined using the model from the $La_{.67}TiO_3$ refinement. Observed d-spacings were compared with theoretical d-spacings calculated by LAZY-PULVERIX[32] based on the refined Guinier parameters, Table 3.8. The refined cell parameters from the Guinier data are given in Table 3.40.

Neutron diffraction studies were carried out to confirm

Table 3.8 Observed and calculated Guinier powder patterns for $La_{.70}TiO_3$ in Pmnm.

D_{obs}	D_{calc*}	HKL
7.766	7.777	0 1 0
3.887	3.889	0 2 0
3.473	3.472	1 1 1
2.747	2.747	1 2 1
2.589	2.592	0 3 0
2.243	2.245	220,022
1.944	1.944	0 4 0
1.885	1.883	2 1 2
1.736	1.736	2 2 2
1.587	1.589	240,042
1.444	1.444	1 5 1
1.374	1.373	2 4 2
1.230	1.230	4 0 2
1.227	1.227	3 2 3
1.173	1.173	4 2 2
1.124	1.124	4 4 0

* a=5.512(1)Å, b=7.777(2)Å, c=5.464(2)Å

the proposed structure of $La_{.70}TiO_3$. The neutron powder diffraction pattern was refined in the orthorhombic space group Pmnm, Table 3.9, the same as that for $La_{.67}TiO_3$. The calculated bond distances and angles are given in Tables 3.10 and 3.11. From these tables, it again can be seen that distortions from the ideal perovskite structure are a result of oxygen atom misalignment. Variations in the two models occurred in atomic positions and unit cell parameters. This is consistent with the idea of the cell having to expand to accommodate the increased Ti^{3+} content in going from $La_{.67}TiO_3$ to $La_{.70}TiO_3$. The refined cell parameters are given in Table 3.41.

3.3.3. $La_{.75}TiO_3$ Powder

The $La_{.75}TiO_3$ powder sample was analyzed for oxygen content by TGA. The final composition was determined to be $La_{.75}TiO_{2.985}$. This composition was calculated based on a 1.12% weight gain when the sample was heated to 800°C in air. The expected weight gain for $La_{.75}TiO_{3.000}$ was calculated to be 0.99%.

The Guinier powder diffraction pattern for $La_{.75}TiO_3$ was different from those obtained for $La_{.67}TiO_3$ and $La_{.70}TiO_3$. The d-spacing line present at a value of approximately 7.7Å found in the $La_{.67}TiO_3$ and $La_{.70}TiO_3$ diffraction patterns was not present in the $La_{.75}TiO_3$ sample. The absence of this line was evidence for a change in symmetry. The pattern was indexed to an

Table 3.9 Atomic positions refined from $La_{.70}TiO_3$ neutron diffraction data in Pmnm.

Atom	x	y	z	B(Å^2)	occ
La1 (2a)	¼	-.5158(11)	¼	.123(39)	.120(2)
La2 (2a)	¼	.0133(6)	¼	.123(39)	.227(2)
Ti1 (2b)	¼	.2610(18)	¾	.025(56)	.2500
Ti2 (2b)	¼	-.2558(20)	¾	.025(56)	.2500
O1 (8g)	.013(1)	-.235(1)	-.520(1)	.979(38)	1.00
O2 (2b)	¼	-.0060(25)	¾	1.21(12)	.2500
O3 (2b)	¼	-.4931(37)	¾	0.84(11)	.2500

R-p = 5.13%
R-wp = 6.76%
R-exp = 2.23%
R-Bragg = 7.15%

Table 3.10 Bond distances calculated from neutron diffraction refinement results for $La_{.70}TiO_3$ in Pmnm.

Bond	Distance(Å)	Multiplicity
La1 - O1	2.836(7)	4×
La1 - O1	2.833(3)	4×
La1 - O3	2.7397(20)	2×
La1 - O3	2.7489(9)	1×
La1 - O3	3.0700(8)	1×
La2 - O1	2.649(4)	4×
La2 - O1	2.694(4)	4×
La2 - O2	2.7381(12)	2×
La2 - O2	2.7486(6)	1×
La2 - O2	3.0698(6)	1×
Ti1 - O1	1.927(4)	4×
Ti1 - O2	2.078(24)	1×
Ti1 - O3	1.91(3)	1×
Ti2 - O1	1.975(4)	4×
Ti2 - O2	1.944(25)	1×
Ti2 - O3	1.85(3)	1×

Table 3.11 Bond angles calculated from neutron diffraction results for $La_{.70}TiO_3$ in Pmnm.

Bonds	Angle
La1-O1-La2	97.28(17)
La1-O3-La1	172.6(12)
La2-O2-La2	177.6(8)
Ti1-O2-Ti2	180.0(0)
Ti1-O3-Ti2	180.0(0)
O2-Ti1-O3	180.0(0)
O2-Ti2-O3	180.0(0)
O1-Ti1-O2	84.0(4)
O1-Ti2-O2	85.4(5)
O1-Ti1-O3	96.0(4)
O1-Ti2-O3	94.6(5)

orthorhombic cell in the space group Imma as determined later by neutron diffraction. The cell parameters were refined from Guinier data as given in Table 3.40. Observed d-spacings are compared with theoretical values in Table 3.12.

As in the $La_{.70}TiO_3$ the increased cell volume, 237.58(8)Å^3, is attributed to the increase of Ti^{3+} within the unit cell.

Neutron diffraction studies were used to determine the structure of the $La_{.75}TiO_3$ powder sample. The neutron diffraction data were refined in the orthorhombic space group Imma using a model proposed by Sunstrom et al.[11] where $La_{.5}Sr_{.5}TiO_3$ neutron powder data were refined in the space group Ibmm.[8]

The neutron powder diffraction data refined well in the space group Imma. Atomic positions and temperature factors can be found in Table 3.13. Bond angles and distances, Table 3.14, show that distortions arise in this sample from tilting of the octahedra along the b-axis. Refined cell parameters are given in Table 3.41.

3.3.4 $La_{.80}TiO_3$ Powder

Initial Guinier analysis on the $La_{.80}TiO_3$ powder sample showed a single phase product with the same symmetry as that of the $La_{.75}TiO_3$ powder sample. The structure was confirmed by neutron powder diffraction. The structure was refined in the orthorhombic space group Imma to a weighted R-factor of 6.30%

Table 3.12 Observed and calculated Guinier powder patterns for $La_{.75}TiO_3$ in Imma.

D_{obs}	D_{calc}*	HKL
3.900	3.904	1 0 1
2.758	2.758	1 2 1
2.356	2.355	112,211
2.254	2.254	220,022
1.952	1.952	2 0 2
1.748	1.747	301,103
1.592	1.592	240,042
1.381	1.382	400,004
1.379	1.379	2 4 2
1.301	1.301	143,341
1.234	1.234	3 2 3
1.232	1.232	1 6 1
1.176	1.176	224,422
1.126	1.126	044,440

* a=5.527(1)Å, b= 7.793(2)Å, c=5.516(1)Å

Table 3.13 Atomic positions refined from $La_{.75}TiO_3$ neutron diffraction data in Imma.

Atom	x	y	z	B(Å^2)	occ
La1 (4e)	0	¼	.9813(5)	.658(45)	.189(1)
Ti1 (4b)	½	0	0	.468(64)	.2500
O1 (4e)	½	¼	.0409(5)	1.312(68)	.2500
O2 (8g)	¼	-.0020(14)	¾	1.834(44)	.5000

R-p = 5.65%
R-wp = 7.47%
R-exp = 2.88%
R-Bragg = 7.76%

Table 3.14 Bond distances and angles calculated from neutron diffraction refinement results for $La_{.75}TiO_3$ in Imma.

Bond	Distance(Å)	Multiplicity
La1 - O1	2.778(3)	2×
La1 - O1	2.64(3)	1×
La1 - O1	2.88(3)	1×
La1 - O2	2.719(8)	4×
La1 - O2	2.800(8)	4×
Ti1 - O1	1.963(3)	2×
Ti1 - O2	1.9501(3)	4×

Bonds	Angle
La1-O2-La1	87.4(3)
O1-La1-O2	117.99(10)
Ti1-O1-Ti1	166.80(16)
Ti1-O2-Ti1	179.1(6)
O1-Ti1-O1	180.0(0)
O2-Ti1-O2	180.0(0)
O1-Ti1-O2	95.1(3) 84.9(3)

as compared with the expected R-factor of 2.00%, Table 3.15. The refined cell parameters were consistent with those found from Guinier results, Table 3.16. The bond angles and distances, Table 3.17, were again evidence that there was a tilt in the titanium octahedra giving rise to the distorted perovskite structure. Refined cell parameters from Guinier and neutron diffraction refinements can be found in Tables 3.40 and 3.41, respectively.

3.3.5 $La_{.88}TiO_3$ and $La_{.92}TiO_3$ Powders

Guinier analysis was carried out on these powder samples. The symmetry was different from that of all the other samples analyzed. There was a shift to a lower symmetry in both of the powders compared with the Guinier results of the $La_{.75}TiO_3$ and $La_{.80}TiO_3$ samples, but the symmetry was higher than that assigned to the $La_{.67}TiO_3$ and $La_{.70}TiO_3$ samples, Tables 3.18 and 3.21. Refined cell parameters are given in Table 3.40.

Neutron diffraction was used to determine the exact symmetry of the systems. A model based on the Sr^{2+} system was used in the refinement of the $La_{.88}TiO_3$ and $La_{.92}TiO_3$ structures, Tables 3.19 and 3.22. Both structures were assigned to the orthorhombic space group Pnma and refined cell parameters were consistent with the distorted perovskite structure, Table 3.41. Bond angles and distances, Tables 3.20 and 3.23 show

Table 3.15 Atomic positions and temperature factors for $La_{.80}TiO_3$ from powder neutron diffraction refinement in Imma.

Atom	x	y	z	B(Å^2)	occ
La1	0	¼	1.0181(24)	.364(99)	.20
Ti1	½	0	0	.918(121)	.25
O1	½	¼	.0527(24)	3.050(338)	.25
O2	¼	.0265(9)	¾	.933(104)	.50

R-wp = 6.30%
R-p = 5.84%
R-exp = 2.00%
R-Bragg = 8.22%

Table 3.16 Observed and calculated Guinier powder patterns for $La_{.80}TiO_3$ in Imma.

D_{obs}	D_{calc}*	HKL
3.915	3.921	1 0 1
2.767	2.768	1 2 1
2.364	2.366	2 1 1
2.265	2.265	2 2 0
2.258	2.258	0 2 2
1.960	1.960	2 0 2
1.955	1.954	0 4 0
1.750	1.750	1 0 3
1.602	1.602	2 4 0
1.598	1.597	0 4 2
1.390	1.389	4 0 0
1.306	1.306	3 4 1
1.242	1.242	4 0 2
1.239	1.239	3 2 3
1.236	1.236	1 6 1
1.180	1.180	4 2 2
1.133	1.132	4 4 0
1.130	1.129	0 4 4

*a=5.557(1)Å, b=7.817(1)Å, c=5.532(1)Å

Table 3.17 Bond distances and angles calculated from neutron diffraction refinement results for $La_{.80}TiO_3$ in Imma.

Bond	Distance(Å)	Multiplicity
La1 - O1	2.7836(16)	2×
La1 - O1	2.372(19)	1×
La1 - O1	3.155(19)	1×
La1 - O2	2.680(9)	4×
La1 - O2	2.873(8)	4×
Ti1 - O1	1.9781(21)	2×
Ti1 - O2	1.9698(9)	4×

Bonds	Angle
La1-O2-La1	89.69(20)
O1-La1-O1	172.1(7)
Ti1-O1-Ti1	163.1(8)
Ti1-O2-Ti1	167.9(4)
O1-Ti1-O1	180.0(0)
O2-Ti1-O2	180.0(0)
O1-Ti1-O2	90.00(3) 90.00(3)

Table 3.18 Observed and calculated Guinier powder patterns for $La_{.88}TiO_3$ in Pnma.

D_{obs}	D_{calc}*	HKL
3.941	3.941	0 2 0
3.524	3.523	1 1 1
2.789	2.791	1 2 1
2.277	2.276	2 2 0
1.972	1.970	0 4 0
1.764	1.762	2 2 2
1.720	1.722	3 1 1
1.610	1.610	2 4 0
1.442	1.440	3 2 2
1.394	1.393	2 4 2
1.315	1.315	420,341
1.231	1.231	2 5 2
1.189	1.189	4 2 2
1.139	1.139	4 4 0

*a=5.585(1), b=7.882(3), c=5.559(1)

Table 3.19 Atomic positions and temperature factors for $La_{.88}TiO_3$ from neutron powder diffraction refinement in Pnma.

Atom	x	y	z	B(Å^2)	occ
La1	.0288(9)	¼	.9970(18)	.842(77)	.44
Ti1	½	0	0	.120(97)	.50
O1	.4937(15)	¼	.0476(17)	.719(110)	.50
O2	.2776(15)	.0400(8)	.7154(13)	1.312(97)	1.00

R-wp = 8.62%
R-p = 5.31%
R-exp = 2.06%
R-Bragg = 7.19%

Table 3.20 Bond distances and angles calculated from neutron diffraction refinement results for $La_{.88}TiO_3$.

Bond	Distance(Å)	Multiplicity
La1 - O1	2.991(9)	1×
La1 - O1	2.603(9)	1×
La1 - O1	3.046(13)	1×
La1 - O1	2.549(13)	1×
La1 - O2	2.670(8)	2×
La1 - O2	2.806(7)	2×
La1 - O2	3.273(6)	2×
La1 - O2	2.470(8)	2×
Ti1 - O1	1.9887(13)	2×
Ti1 - O2	2.038(9)	2×
Ti1 - O2	1.98(1)	2×

Bonds	Angle
La1-O2-La1	99.2(3)
O1-La1-O2	127.9(3)
Ti1-O1-Ti1	164.5(5)
Ti1-O2-Ti1	157.0(3)
O1-Ti1-O1	180.0(0)
O2-Ti1-O2	180.0(0)
O1-Ti1-O2	86.8(5) 93.4(5) 86.4(4)

Table 3.21 Observed and calculated Guinier powder patterns of $La_{.92}TiO_3$ in Pnma.

D_{obs}	D_{calc}*	HKL
3.955	3.957	0 2 0
3.539	3.539	1 1 1
2.799	2.798	1 2 1
2.287	2.287	2 2 0
2.195	2.195	1 3 1
1.980	1.979	0 4 0
1.770	1.770	2 2 2
1.727	1.729	3 1 1
1.616	1.616	2 4 0
1.469	1.468	1 3 3
1.445	1.446	3 2 2
1.399	1.399	2 4 2
1.320	1.321	420,341
1.302	1.301	3 1 3
1.251	1.253	4 0 2
1.236	1.236	2 5 2
1.232	1.234	2 1 4
1.193	1.193	4 2 2
1.181	1.181	3 5 1
1.144	1.144	4 4 0
1.143	1.141	0 4 4
1.131	1.132	4 3 2
1.108	1.108	5 2 2

*a=5.606(1)Å, b=7.914(1)Å, c=5.584(1)Å

Table 3.22 Atomic positions and temperature factors for $La_{.92}TiO_3$ from powder neutron diffraction refinement in Pnma.

Atom	x	y	z	B(Å^2)	occ
La1	.0384(6)	¼	.9891(11)	.408(62)	.46
Ti1	½	0	0	.4000	.50
O1	.4885(11)	¼	.0829(15)	1.096(115)	.50
O2	.2848(8)	.0379(6)	.7116(8)	.574(71)	1.00

R-wp = 6.65%
R-p = 5.33%
R-exp = 2.60%
R-Bragg = 7.33%

Table 3.23 Bond distances and angles calculated from neutron diffraction refinement results for $La_{.92}TiO_3$.

Bond	Distance(Å)	Multiplicity
La1 - O1	3.121(6)	1×
La1 - O1	2.572(7)	1×
La1 - O1	3.22(1)	1×
La1 - O1	2.417(10)	1×
La1 - O2	2.672(5)	2×
La1 - O2	2.779(5)	2×
La1 - O2	3.358(5)	2×
La1 - O2	2.469(6)	2×
Ti1 - O1	2.033(2)	2×
Ti1 - O2	2.009(6)	2×
Ti1 - O2	2.039(5)	2×

Bonds	Angle
La1-O2-La1	97.78(23)
O1-La1-O2	130.98(16)
Ti1-O1-Ti1	153.31(45)
Ti1-O2-Ti1	156.21(23)
O1-Ti1-O1	180.0(0)
O2-Ti1-O2	180.0(0)
O1-Ti1-O2	89.15(26) 90.85(26) 88.88(33)

that the distorted perovskite structure is a result of tilting in the octahedra within the lattice.

3.3.6 $La_{.67}TiO_3$ Single Crystal

Guinier analysis was done on a ground single crystal of $La_{.67}TiO_3$. The lines of this diffraction pattern matched those of the one observed for the $La_{.67}TiO_3$ powder sample. The observed d-spacing value of 7.755Å in the $La_{.67}TiO_3$ powder was also present in the pattern recorded for the ground single crystal at d = 7.759Å. The lines in the ground single crystal diffraction pattern were indexed with LSUDF to the orthorhombic unit cell with the cell parameters as given in Table 3.40. These lattice parameters agree well with those assigned to the previous powder sample of $La_{.67}TiO_3$. Theoretical d-spacings were calculated with LAZY-PULVERIX[32] based on this refined model from the Guinier data, Table 3.24.

Single crystal x-ray diffraction experiments carried out on the Siemens PV/3 diffractometer yielded a similar result to that observed in the previous diffraction analyses for $La_{.67}TiO_3$. The conditions for data collection and refinement are given in Tables 3.25, 3.26, and 3.27. It should also be noted that the intensity of the three standards decreased by 6.7% over the data collection. A decay correction was made in the data used for refinement. The unit cell parameters in this

Table 3.24 Observed and calculated Guinier powder patterns of $La_{.67}TiO_3$ single crystal in Pmnm.

D_{obs}	D_{calc}	HKL
7.759	7.763	0 1 0
3.469	3.462	1 1 1
2.740	2.740	1 2 1
2.583	2.583	2 1 0
2.238	2.238	2 2 0
1.941	1.941	0 4 0
1.934	1.934	2 0 2
1.582	1.881	2 4 0
1.584	1.583	0 4 2
1.441	1.441	1 5 1
1.434	1.436	1 3 3
1.372	1.370	2 4 2
1.370	1.369	0 0 4
1.227	1.227	1 6 1
1.223	1.222	204,402
1.170	1.170	2 6 0
1.158	1.156	3 5 1
1.121	1.119	4 4 0

*a=5.477(1)Å, b=7.763(1)Å, c=5.461(1)Å

Table 3.25 Crystal data for $La_{.67}TiO_3$

Empirical Formula	$La_{2.6664}\ O_{12}\ Ti_4$
Color; Habit	Yellow, rectangle
Crystal size (mm)	.15 × .15 × .25
Crystal System	Orthorhombic
Space Group	Pmnm
Unit Cell Dimensions	a = 5.4850(10) Å
	b = 7.749(2) Å
	c = 5.4850(10) Å
Volume	233.13(9) $Å^3$
Z	1
Formula weight	754.0
Density(calc.)	5.370 Mg/m^3
Absorption Coefficient	15.254 mm^{-1}
F(000)	335.98

Table 3.26 Conditions for single crystal data collection for $La_{.67}TiO_3$.

Diffractometer Used	Siemens P3/V
Radiation	AgKα (λ = 0.56086 Å)
Temperature (K)	298
Monochromator	Highly oriented graphite crystal
2θ Range	3.0 to 110.0°
Scan Type	2θ-θ
Scan Speed	Variable; 1.50 to14.00°/min. in ω
Scan Range (ω)	1.00° plus Kα-separation
Background Measurement	Stationary crystal and stationary counter at beginning and end of scan, each for 25.0% of total scan time
Standard Reflections	3 measured every 97 reflections
Index Ranges	$0 \leq h \leq 11$, $-11 \leq k \leq 11$
	$-16 \leq l \leq 16$
Reflections Collected	5215
Independent Reflections	1417 (R_{int} =3.11%)
Observed Reflections	833 ($F \geq 4.0\sigma(F)$)
Absorption Correction	DIFABS

Table 3.27 Solution and refinement parameters for $La_{.67}TiO_3$ single crystal.

System Used	Siemens SHELXTL PLUS (PC Version)
Solution	Patterson Method
Refinement Method	Full-Matrix Least-Squares
Quantity Minimized	$\Sigma w(F_o-F_c)^2$
Extinction Correction	N/A
Weighting Scheme	$w^{-1} = \sigma^2(F) + 0.0005F^2$
Number of Parameters Refined	35
Final R Indices (obs. data)	R =5.07 %, wR =8.01 %
R Indices (all data)	R =9.94 %, wR = 10.07 %
Goodness-of-Fit	2.26
Largest and Mean Δ/σ	0.089,0.014
Data-to-Parameter Ratio	23.8:1
Largest Difference Peak	8.07 $eÅ^{-3}$
Largest Difference Hole	-4.59 $eÅ^{-3}$

case were determined to be a = 5.485(1)Å, b = 7.749(1)Å and c = 5.485(1)Å. These results were somewhat misleading at first since the unit cell appeared to be tetragonal. Refinement in a variety of space groups showed that there was actually no four fold axis which would give rise to tetragonal symmetry. There are three different Ti-O bond lengths around each of the central titanium atoms of individual octahedron, Table 3.28.

The four fold axis would show up if the distances between the four oxygens 1.936(4)Å from Ti1 and the four oxygens 1.954(4)Å from Ti2 were equally spaced from one another in the form of a square. This is not the case, however. The oxygens are arranged in rectangles around the central titaniums as determined by distances between oxygens. Therefore, the symmetry of the $La_{.67}TiO_3$ structure can not be tetragonal, consistent with the results found previously for the $La_{.67}TiO_3$ system being orthorhombic, Figure 3.2.

Since the Ti-O-Ti bond angles in the b-direction are 180.0°, Table 3.29, tilting of the octahedra can not be responsible for the doubling of the b-axis to give the orthorhombic distortion of the perovskite structure. X-ray analysis shows that there is a distortion in the individual Ti octahedron with a repeat distance of twice the ideal perovskite unit cell length. As can be seen from Figure 3.3, the titanium octahedra along the b-direction are different in

Table 3.28 Bond distances calculated from single crystal x-ray diffraction refinement results for $La_{.67}TiO_3$ in Pmnm.

Bond	Distance(Å)	Multiplicity
La1 - O1	2.724(5)	4×
La1 - O1	2.838(5)	4×
La1 - O3	2.7431(8)	2×
La1 - O3	2.7425(5)	1×
La1 - O3	3.0662(5)	1×
La2 - O1	2.635(5)	4×
La2 - O1	2.777(5)	4×
La2 - O2	2.7425(5)	2×
La2 - O2	2.7427(6)	1×
La2 - O2	3.0664(6)	1×
Ti1 - O1	1.936(4)	4×
Ti1 - O2	1.99(3)	1×
Ti1 - O3	1.89(3)	1×
Ti2 - O1	1.954(4)	4×
Ti2 - O2	1.94(3)	1×
Ti2 - O3	1.92(3)	1×

Bond distances between oxygens in rectangular planes of octahedra

Ti1	O1D-O1\L, O1[R-O1X	2.927Å
	O1\L-O1X, O1D-O1[R	2.589Å
Ti2	O1J-O1[J, O1[X-O1[B	2.896Å
	O1J-O1[X, O1[J-O1[B	2.558Å

Figure 3.2 Crystal structure for $La_{.67}TiO_3$ as determined from single crystal x-ray diffraction.

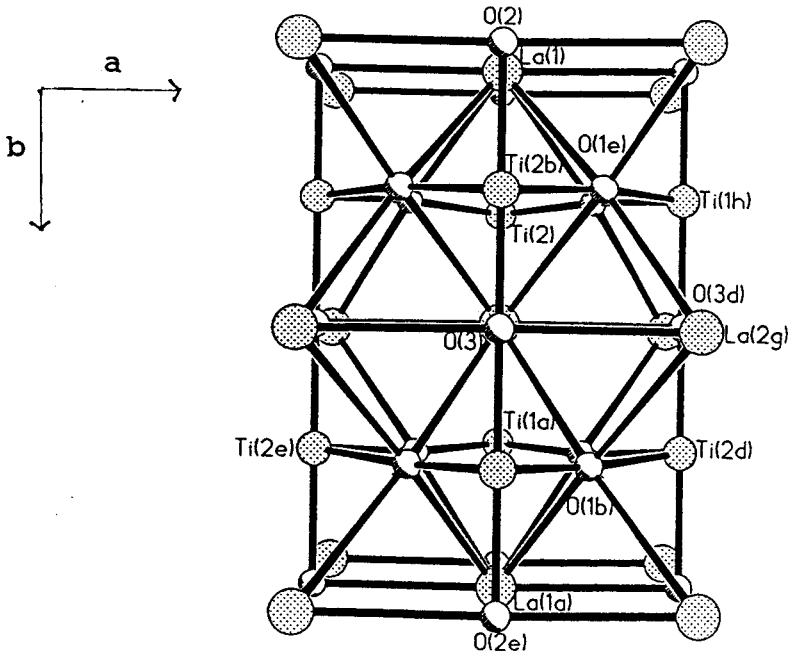

Unit cell of $La_{.67}TiO_3$

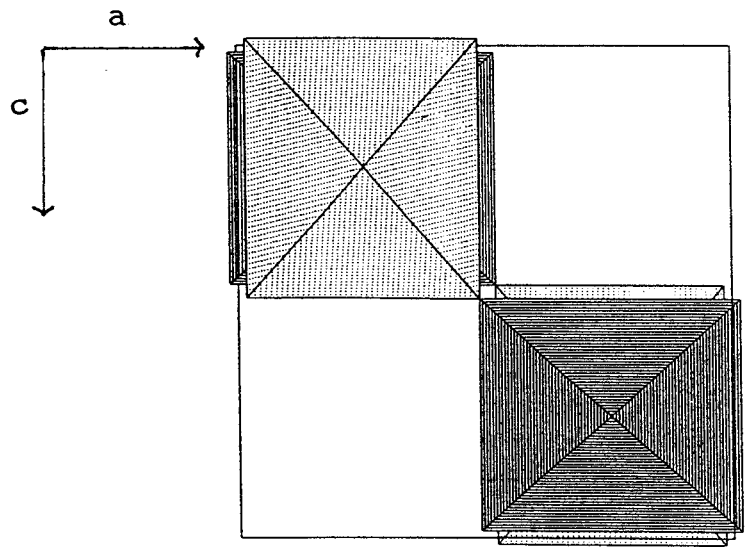

Octahedral distortions in $La_{.67}TiO_3$

Table 3.29 Bond angles calculated from single crystal x-ray diffraction results for $La_{.67}TiO_3$ in Pmnm.

Bonds	Angle
La1-O1-La2	94.40(13)
La1-O2-La1	177.5(13)
La2-O3-La2	179.5(14)
Ti1-O2-Ti2	180.0(0)
Ti1-O3-Ti2	180.0(0)
O2-Ti1-O3	180.0(0)
O2-Ti2-O3	180.0(0)
O1-Ti1-O2	86.47(21)
O1-Ti2-O2	88.50(23)
O1-Ti1-O3	93.53(21)
O1-Ti2-O3	91.50(23)

size. This difference in titanium octahedra shape and the staggered order is what causes the doubling in the b-axis. Since the oxygen positions are not aligned throughout the lattice as a result of distorted titanium octahedra, distortion in the ac plane occurs, giving rise to the orthorhombic distortion from the cubic perovskite structure.

Parameters from the single crystal x-ray refinement are given in Tables 3.30 and 3.31.

Lanthanum cations are distributed around the lattice in an ordered fashion as well. The two lanthanum sites, 2a and 2b, are both partially occupied, but not in a one to one ratio as would be expected for a disordered system.

The only apparent relationship evident is the occurrence of a distortion caused by the oxygen positioning, detected by weak reflections in x-ray diffraction data and confirmed by neutron diffraction, and an ordered distribution of lanthanum cations and vacancies. It seems reasonable that the ordering of the vacancies or cations has a direct effect on the oxygen positions throughout the lattice.

Precession photographs were taken of the diffraction patterns of the $La_{.67}TiO_3$ crystal in four different orientations. Although the zero layers were not photographed, the diffraction patterns obtained allowed confirmation of the unit cell parameters determined previously by other methods.

Table 3.30 Atomic parameters for $La_{.67}TiO_3$ in Pmnm based on single crystal x-ray diffraction.

Atom	x	y	z	occ.
La1(2a)	¼	-.5048(5)	¼	.1279(6)
La2(2a)	¼	.0027(3)	¼	.2054(6)
Ti1(2b)	¼	.2586(7)	¾	.25000
Ti2(2b)	¼	-.2498(8)	¾	.25000
O1(8g)	.0140(6)	-.2432(6)	-.5168(7)	1.00000
O2(2b)	¼	.0012(43)	¾	.25000
O3(2b)	¼	.5028(41)	¾	.25000

R = 5.07%
Rw = 5.67%
wR = 8.01%
GOOF = 2.26%

Table 3.31 Anisotropic temperature factors from single crystal x-ray diffraction refinement of $La_{.67}TiO_3$ in Pmnm.

	La1	La2	Ti1	Ti2
U11	.0084(3)	.0061(2)	.0044(6)	.0067(7)
U22	.0083(4)	.0060(2)	.0043(6)	.0062(6)
U33	.0073(5)	.0063(2)	.0040(9)	.0063(5)
U12	0	0	0	0
U13	0	0	0	0
U23	0	0	0	0
Ueq	.0080(2)	.0061(1)	.0042(4)	.0064(4)

	O1	O2	O3
U11	.0005(14)	.0397(53)	.0446(57)
U22	.0026(13)	.0390(53)	.0402(53)
U33	.0462(28)	.0054(21)	.0008(21)
U12	-.0001(10)	0	0
U13	-.0009(16)	0	0
U23	.0010(18)	0	0
Ueq	.0164(11)	.0280(26)	.0285(27)

The cell was found to be orthorhombic with unit cell parameters of a = 5.60Å, b = 7.74Å, and c = 5.50Å. This agreed well with the results obtained from the Guinier films.

Electron diffraction studies showed a comparable cell to those previously determined. However, electron diffraction also showed weak diffraction spots corresponding to another doubling of the b axis. Measurements of the photographs led to a b-axis length of 15.9Å. X-ray diffraction was used to look for the existence of this larger unit cell, but the corresponding diffraction pattern was not found. However, electron diffraction showed evidence for the cell previously assigned with axis lengths of a=5.5Å, b=7.8Å, and c=5.5Å. This confirms that there is a doubling of the b-axis from the ideal perovskite structure. The question remains as to whether or not the b-axis is doubled again in the structure to give the value of 15.6Å observed.

3.3.7 $La_{.75}TiO_3$ Single Crystal

A single crystal of $La_{.75}TiO_3$ was ground in order to do Guinier powder diffraction. The observed powder pattern matched that of the $La_{.75}TiO_3$ powder sample and was indexed in the space group Imma, Table 3.32. The refined unit cell parameters were slightly larger than those determined for the powder sample, Table 3.40. This may be a result of the method

Table 3.32 Observed and calculated Guinier powder patterns for a $La_{.75}TiO_3$ single crystal in Imma.

D_{obs}	D_{calc}*	HKL
3.914	3.914	1 0 1
2.761	2.731	1 2 1
2.362	2.361	2 1 1
2.357	2.358	1 1 2
2.257	2.258	2 2 0
1.954	1.957	2 0 2
1.950	1.948	0 4 0
1.597	1.598	2 4 0
1.594	1.595	0 4 2
1.385	1.385	4 0 0
1.381	1.381	2 4 2
1.236	1.237	3 2 3
1.234	1.233	1 6 1
1.181	1.180	4 2 2
1.128	1.129	4 4 0

*a=5.541(1)Å, b=7.793(1)Å, c=5.528(1)Å

used to obtain the single crystal.

Single crystal precession photographs show the unit cell parameters as being a = 5.46Å, b = 7.76Å, and c = 5.42Å. This is consistent with the parameters determined previously for both the powder and crystalline samples.

The unit cell determined from single crystal x-ray diffraction was indexed to an orthorhombic unit cell in Imma with cell parameters of a = 5.513(1)Å, b = 7.812(2)Å, and c = 5.513(1)Å. The conditions for the data collection and refinement are given in Tables 3.33, 3.34, and 3.35. A DIFABS[33] absorption correction was applied to the data.

The structure was determined to be of the distorted perovskite type like that of the previously analyzed samples. The distortion was a result of octahedral tilting within the lattice. The Ti-O-Ti bond angles in the b-direction were determined to be 175.9(5)°, Table 3.36. The tilting of the octahedra is staggered so that the repeat distance becomes twice the unit cell edge of the ideal perovskite structure. The oxygen atoms in the ac plane were also misaligned. This is possibly due to a second tilt system within the lattice, which is not unusal for compounds of this space group.[5,6]

These distortions explain why the structure is not cubic, but instead orthorhombic with $a \approx c \approx \sqrt{2}a_o$ and $b \approx 2a_o$, where a_o is the unit cell length in the ideal perovskite structure. The

Table 3.33 Crystal Data for $La_{.75}TiO_3$

Empirical Formula	$La_{3.1066}\ O_{12}\ Ti_4$
Color; Habit	Black, plate
Crystal size (mm)	.2 x .2 x .1
Crystal System	Orthorhombic
Space Group	Imma
Unit Cell Dimensions	$\underline{a}$ = 5.5130(10) Å
	$\underline{b}$ = 7.712(2) Å
	$\underline{c}$ = 5.5130(10) Å
Volume	234.39(9) $Å^3$
Z	1
Formula weight	815.1
Density(calc.)	5.775 Mg/m^3
Absorption Coefficient	17.125 mm^{-1}
F(000)	361.08

Table 3.34 Conditions for single crystal data collection on $La_{.75}TiO_3$.

Diffractometer Used	Siemens P3/V
Radiation	AgKα (λ = 0.56086 Å)
Temperature (K)	298
Monochromator	Highly oriented graphite crystal
2θ Range	3.0 to 80.0°
Scan Type	2θ-θ
Scan Speed	Variable; 1.50 to14.00°/min. in ω
Scan Range (ω)	1.00° plus Kα-separation
Background Measurement	Stationary crystal and stationary counter at beginning and end of scan, each for 25.0% of total scan time
Standard Reflections	3 measured every 97 reflections
Index Ranges	$-9 \leq h \leq 9$, $-19 \leq k \leq 19$
	$0 \leq l \leq 13$
Reflections Collected	2149
Independent Reflections	617 (R_{int} =4.73%)
Observed Reflections	387 ($F \geq 4.0\sigma(F)$)
Absorption Correction	DIFABS

Table 3.35 Solution and refinement paramters for $La_{.75}TiO_3$ single crystal

System Used	Siemens SHELXTL PLUS (PC Version)
Solution	Patterson Method
Refinement Method	Full-Matrix Least-Squares
Quantity Minimized	$\Sigma w(F_o-F_c)^2$
Extinction Correction	χ = 0.0000(3), where $F^* = F [\ 1 + 0.002\chi F^2/\sin(2\theta)\ ]^{-1/4}$
Weighting Scheme	$w^{-1} = \sigma^2(F) + 0.0007F^2$
Number of Parameters Refined	20
Final R Indices (obs. data)	R =3.47 %, wR =5.52 %
R Indices (all data)	R =6.81 %, wR =7.70 %
Goodness-of-Fit	1.34
Largest and Mean Δ/σ	0.006,0.000
Data-to-Parameter Ratio	19.4:1
Largest Difference Peak	1.90 eÅ^{-3}
Largest Difference Hole	-2.43 eÅ^{-3}

Bond lengths and angles for the $La_{.75}TiO_3$ structure are given in Table 3.36. The refined atomic positions and temperature factors are given in Tables 3.37 and 3.38.

3.3.8 $La_{.80}TiO_3$ Single Crystal

A single crystal of $La_{.80}TiO_3$ was ground to a powder in order to do Guinier powder diffraction. The observed powder pattern of this ground single crystal matched the observed for the powder sample and was indexed in the Imma space group, Table 3.40. Refinement in LSUDF gave slightly different cell parameters, as given in Table 3.39, but the unit cell volume remained the same as that of the powder sample.

No further analysis was done on the $La_{.80}TiO_3$ crystal for structural information since the structure was refined previously by neutron diffraction with the powder sample.

Table 3.36 Bond distances and angles calculated from single crystal x-ray diffraction refinement results for $La_{.75}TiO_3$ in Imma.

Bond	Distance(Å)	Multiplicity
La1 - O1	2.7720(6)	2×
La1 - O1	2.716(8)	1×
La1 - O1	2.812(8)	1×
La1 - O2	2.689(5)	4×
La1 - O2	2.797(6)	4×
Ti1 - O1	1.9495(4)	2×
Ti1 - O2	1.951(1)	4×

Bonds	Angle
La1-O2-La1	89.3(1)
O1-La1-O2	119.0(1)
Ti1-O1-Ti1	175.9(5)
Ti1-O2-Ti1	174.6(5)
O1-Ti1-O1	180.0(1)
O2-Ti1-O2	180.0(1)
O1-Ti1-O2	94.2(3) 85.8(3)

Table 3.37 Atomic parameters for $La_{.75}TiO_3$ in Imma based on single crystal x-ray diffraction.

Atom	x	y	z	occ.
La1(4e)	0	¼	.9961(1)	.1942(21)
Ti1(4b)	½	0	0	.25000
O1(4e)	½	¼	.0126(15)	.25000
O2(8g)	¼	-.0121(10)	¾	.50000

R = 3.47%
Rw = 4.07%
wR = 5.52%
GOOF = 1.34%

Table 3.38 Anisotropic temperature factors from single crystal x-ray diffraction refinement of $La_{.75}TiO_3$ in Imma.

	La1	Ti1	O1	O2
U11	.0073(3)	.0063(6)	.0408(163)	.0345(85)
U22	.0077(1)	.0058(3)	.0047(15)	.0367(41)
U33	.0077(1)	.0062(3)	.0521(65)	.0359(31)
U12	0	0	0	0
U13	0	0	0	-.0308(43)
U23	0	-.0001(3)	0	0
Ueq	.0076(1)	.0061(2)	.0326(59)	.0357(33)

Figure 3.3 Crystal structure of $La_{.75}TiO_3$ as determined from single crystal x-ray diffraction.

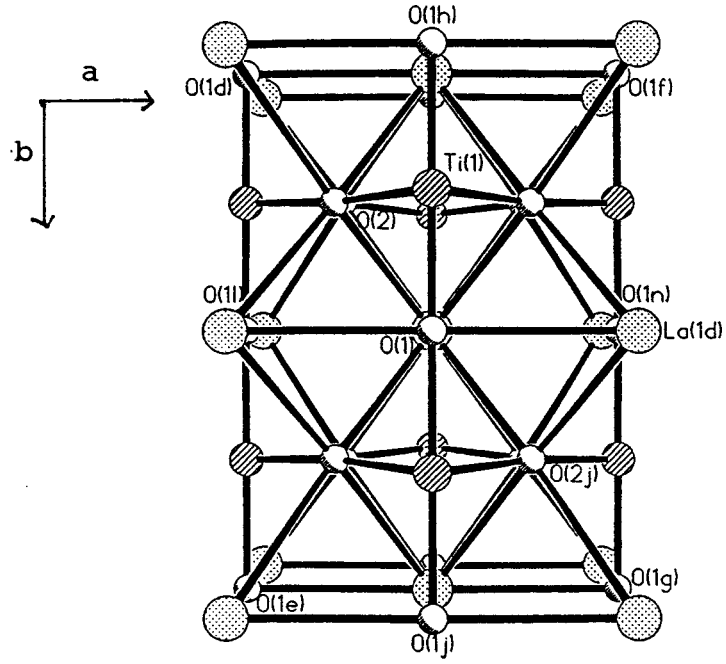

Unit cell of $La_{.75}TiO_3$

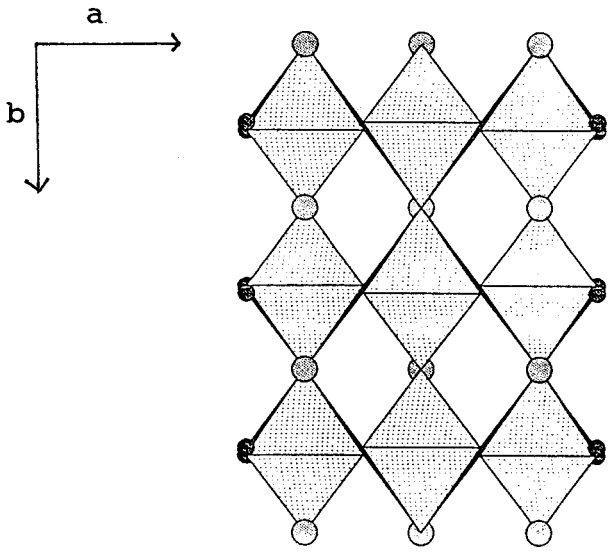

Tilts in the titanium octahedra

Table 3.39 Observed and calculated Guinier powder patterns for a $La_{.80}TiO_3$ single crystal in Imma.

D_{obs}	D_{calc}*	HKL
3.914	3.913	1 0 1
2.765	2.768	1 2 1
2.357	2.356	2 1 1
2.261	2.265	2 2 0
2.257	2.256	0 2 2
1.958	1.958	2 0 2
1.596	1.596	2 4 0
1.382	1.384	4 0 0
1.238	1.238	4 0 2
1.235	1.236	3 2 3
1.133	1.133	4 4 0
1.099	1.099	3 4 1

*a=5.556(1)Å, b=7.826(4)Å, c=5.518(2)Å

Table 3.40 Cell parameters calculated from Guinier powder diffraction.

Comp.	Space Group	a(Å)	b(Å)	c(Å)	Vol(Å^3)
$La_{.67}TiO_3$	Pmnm	5.482(1)	7.759(3)	5.461(1)	232.28(9)
$La_{.67}TiO_3$	Pmnm	5.477(1)	7.763(1)	5.461(2)	232.19(8)*
$La_{.70}TiO_3$	Pmnm	5.464(2)	7.777(2)	5.512(1)	234.22(10)
$La_{.75}TiO_3$	Imma	5.527(1)	7.793(2)	5.516(1)	237.58(8)
$La_{.75}TiO_3$	Imma	5.541(1)	7.793(1)	5.528(1)	238.70(6)*
$La_{.80}TiO_3$	Imma	5.557(1)	7.817(1)	5.532(1)	240.30(6)
$La_{.80}TiO_3$	Imma	5.556(1)	7.826(4)	5.518(2)	239.93(13)*
$La_{.88}TiO_3$	Pnma	5.582(1)	7.882(3)	5.559(1)	244.58(9)
$La_{.92}TiO_3$	Pnma	5.606(1)	7.914(1)	5.584(1)	247.74(7)
$La_{1.0}TiO_3$	Pnma	5.63(1)	7.940(8)	5.614(9)	251.1(9)†

* data obtained from ground single crystal.

† Ref. 7

Table 3.41 Cell parameters calculated from neutron powder profile refinement.

Comp.	Space Group	a(Å)	b(Å)	c(Å)	Vol(Å^3)
$La_{.67}TiO_3$	Pmnm	5.473(3)	7.763(2)	5.461(3)	232.02(16)
$La_{.70}TiO_3$	Pmnm	5.496(1)	7.784(1)	5.468(1)	233.93(5)
$La_{.75}TiO_3$	Imma	5.516(1)	7.798(3)	5.515(1)	237.22(9)
$La_{.80}TiO_3$	Imma	5.554(2)	7.826(3)	5.527(2)	240.23(14)
$La_{.88}TiO_3$	Pnma	5.581(2)	7.882(2)	5.564(2)	244.76(12)
$La_{.92}TiO_3$	Pnma	5.609(1)	7.912(2)	5.594(1)	248.25(8)
$La_{1.0}TiO_3$†	Pnma	5.63(1)	7.940(8)	5.614(9)	251.1(9)

† Ref. 7

Chapter 4

Electrical and Magnetic Properties

4.1 Electrical Resistivity

Resistivity measurements were made on the samples $La_{.70}TiO_3$, $La_{.75}TiO_3$, and $La_{.80}TiO_3$. The $La_{.70}TiO_3$ and $La_{.75}TiO_3$ samples were sintered pellets of rectangular shape. The average volume of these samples was approximately $0.2cm^3$. The $La_{.80}TiO_3$ sample was a single crystal, cylindrical in shape. The level surface where contacts were made was normal to the b-axis as determined from Laue photographs.

The $La_{.70}TiO_3$ sample has a Ti^{3+} concentration of 9%, and as can be seen in Figure 4.1, has a room temperature resistivity of 4.31 Ωcm. As the temperature is decreased from 300K to 5K, the resistivity increased to 93.74 Ωcm. An exponential increase in resistivity with a decreasing temperature is expected for semiconductors, but this behavior was not observed for the $La_{.70}TiO_3$ sample. The plot of $\ln(1000/\rho)$ versus inverse temperature, Figure 4.2 shows that the resistivity data is complex for this material and can not be fitted by a single activation energy.

The $La_{.75}TiO_3$ sample has a Ti^{3+} concentration of 28% and as can be seen from Figure 4.3, has a room temperature resistivity of 8.24 mΩcm. As the temperature was decreased from 300K to 5K the resistivity increased linearly to a maximum of 16.09 mΩcm at 81K. The resistivity then decreased to 14.33 mΩcm as the temperature was decreased to 5K. This behavior is very unusual and could mark a transition point between a semiconducting state and a metallic state. The plot of $\ln(1000/\rho)$ versus inverse temperature, Figure 4.4, shows that the data is again complex for this material and can not be fit by a single activation energy.

The $La_{.80}TiO_3$ single crystal has a Ti^{3+} concentration of 40% and a room temperature resistivity of 1.08 mΩcm as can be seen from Figure 4.5. As the temperature was decreased from 300K to 5K, the resistivity decreased almost linearly to 0.75 mΩcm, in accordance with that expected for a metallic compound.

The resistivity data for the $La_{.80}TiO_3$ single crystal were not as well defined as that obtained for the $La_{.70}TiO_3$ and $La_{.75}TiO_3$ sintered samples. High contact resistance was believed to be the cause, so the crystal face was polished and the resistivity measurements were taken again. The quality of the results did not improve with the polished crystal, so the results obtained originally were used in this study.

Previous work on the $La_{.88}TiO_3$ and $La_{.92}TiO_3$ samples[21] has

shown a decrease in room temperature resistivity at the Ti^{3+} concentration above 64%. This agrees well with the structural transition found to a lower symmetry group.

Throughout the series we have seen a progression from a semiconducting state to a metallic state. The transition was assigned at a Ti^{3+} concentration of 28%. This transition is coincident with that observed in the structural data where the symmetry changed from Pmmn to Imma. This may be indicative of a dependence of electrical and structural properties on the Ti^{3+} concentration present in the individual materials.

4.2 Magnetic Susceptibility

Magnetic susceptibility measurements were done on sintered samples of $La_{.70}TiO_3$, $La_{.75}TiO_3$, $La_{.80}TiO_3$, $La_{.88}TiO_3$, and $La_{.92}TiO_3$. Each of these samples was approximately 200mg in size. The samples were run under an applied field strength of 2000 Oe in the temperature range 300 K to 5K.

Most of the samples showed a temperature independent region from 300K to 50K. Below this temperature, the susceptibility was temperature dependent resulting in each of the samples having a paramagnetic tail.

The $La_{.70}TiO_3$ sample, Ti^{3+} = 9%, had a room temperature magnetic susceptibility of 0.047×10^{-2} emu/mol, Figure 4.6, and a paramagnetic tail below 50K. Since this sample had the lowest Ti^{3+} concentration of the samples measured, it should

have the lowest magnetic susceptibility values. The magnetic data was fitted to the Curie-Weiss Law,

$$\chi = (C/T-\theta) + \chi_{TIP}$$

where C = Curie constant

T = temperature

θ = Weiss constant

χ_{TIP} = temperature independent magnetic susceptibility. The values for these constants and temperature independent susceptibility are given in Table 4.1.

The $La_{.75}TiO_3$ sample, Ti^{3+} = 28%, had a room temperature magnetic susceptibility of 0.0148×10^{-2}emu/mol, Figure 4.7, and a paramagnetic tail. This magnetic susceptibility was lower than that observed for the $La_{.70}TiO_3$ sample. Since the concentration of Ti^{3+} is increased, a decrease in the magnetic susceptibility could be due to a change in the symmetry from that of the $La_{.70}TiO_3$ sample. Magnetic susceptibility data was fit to the Curie-Weiss Law as given previously. The constants and temperature independent susceptibility are given in Table 4.1. From the structural data, it has been observed that a structural transition occurs for this Ti^{3+} concentration where the symmetry changes from Pmmn like that of the $La_{.70}TiO_3$ structure to Imma found for the $La_{.75}TiO_3$ sample. The electrical resistivity data also shows a transitions from a semiconducting state to a metallic state at this composition.

Table 4.1 Constants from Curie-Weiss fit of magnetic susceptibility data.

	$La_{.70}TiO_3$	Sigma	$La_{.75}TiO_3$	Sigma
C	.002569	19.2E-03	.000523	15.6E-03
θ	-4.16495		-.69992	
χ_{TIP}	.000434	.260E-06	.000138	.416E-06

The $La_{.80}TiO_3$ sample has a Ti^{3+} concentration of 40% and a room temperature magnetic susceptibility of 0.026×10^{-2} emu/mol, Figure 4.8. This is consistent with the data obtained for the $La_{.75}TiO_3$ sample where an increased Ti^{3+} content leads to a higher magnetic susceptibility. Below 50K the susceptibility was temperature dependent resulting in a paramagnetic tail.

The $La_{.88}TiO_3$ sample had a Ti^{3+} concentration of 64% and a room temperature magnetic susceptibility of 0.0573×10^{-2} emu/mol, Figure 4.9. This sample had a slight temperature dependence in the temperature range 300K to 50K. The susceptibility was very temperature dependent below 50K resulting in a paramagnetic tail. This temperature dependence above 50K marks another transition in the series. The transition occurs at the same composition as that for the structural transition from Imma to Pnma.

The $La_{.92}TiO_3$ sample, Ti^{3+} = 76%, was different from the

rest of the samples analyzed, Figure 4.10. The magnetic susceptibility at room temperature was 0.0788×10^{-2} emu/mol. The susceptibility data showed a temperature independent region between 300K and 110K and a weak antiferromagnetic peak arising at 70K.

The results found for the magnetic properties of the $La_{1-x}TiO_3$ series are in agreement with what was expected based on the structural and electrical data. These properties are all dependent upon the Ti^{3+} concentration present in the individual materials, with transitions occurring at critical Ti^{3+} concentrations of 28% and 64%.

The magnetic susceptibility plots for the $La_{.80}TiO_3$ and $La_{.92}TiO_3$ samples have peaks arising at 50K. These peaks are a result of solid oxygen forming in the sample tube, giving a paramagnetic signal.

Figure 4.1 Resistivity versus temperature plot for $La_{.70}TiO_3$.

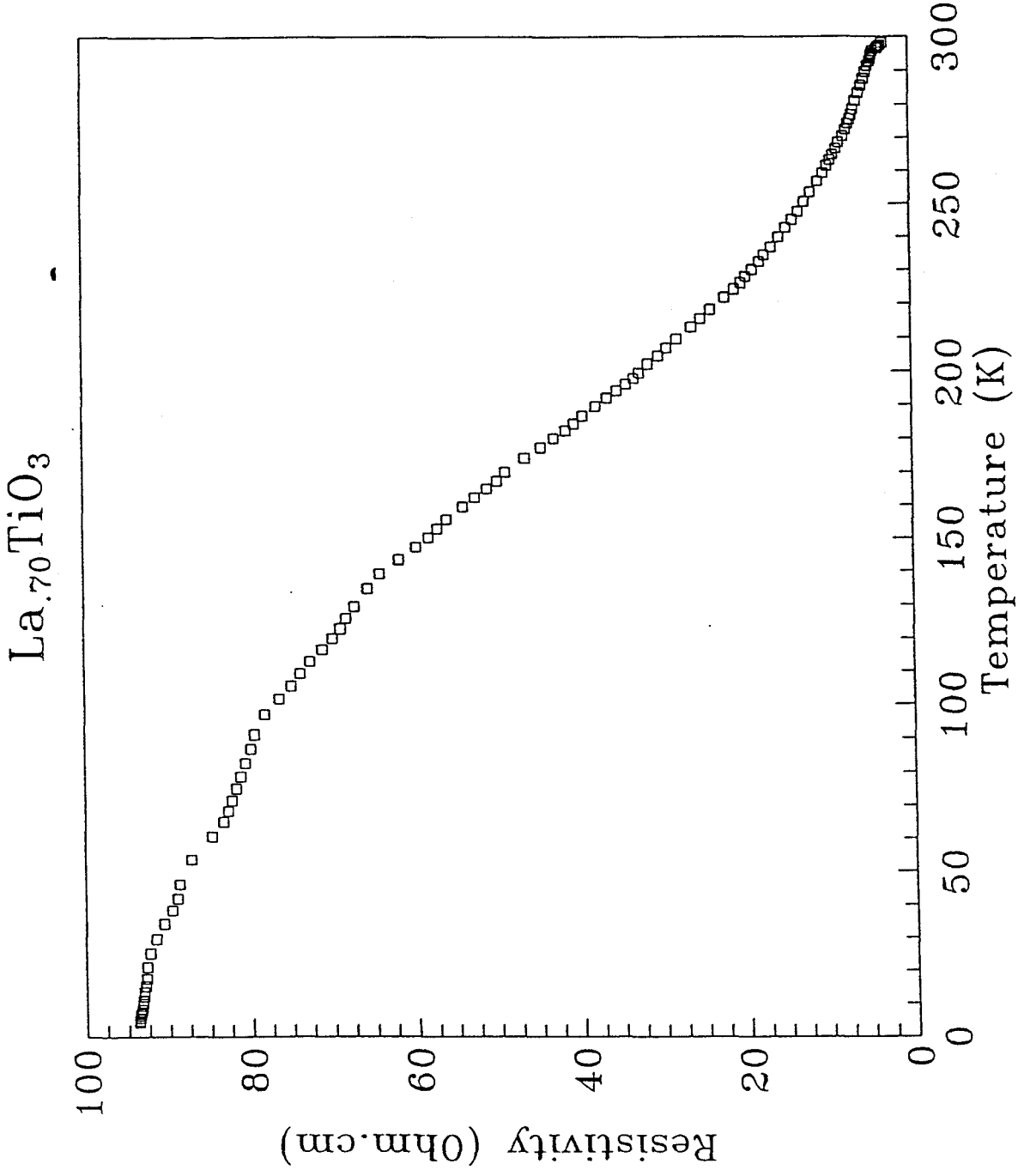

Figure 4.2 Plot of ln(1000/ρ) versus 1/temperature for $La_{.70}TiO_3$.

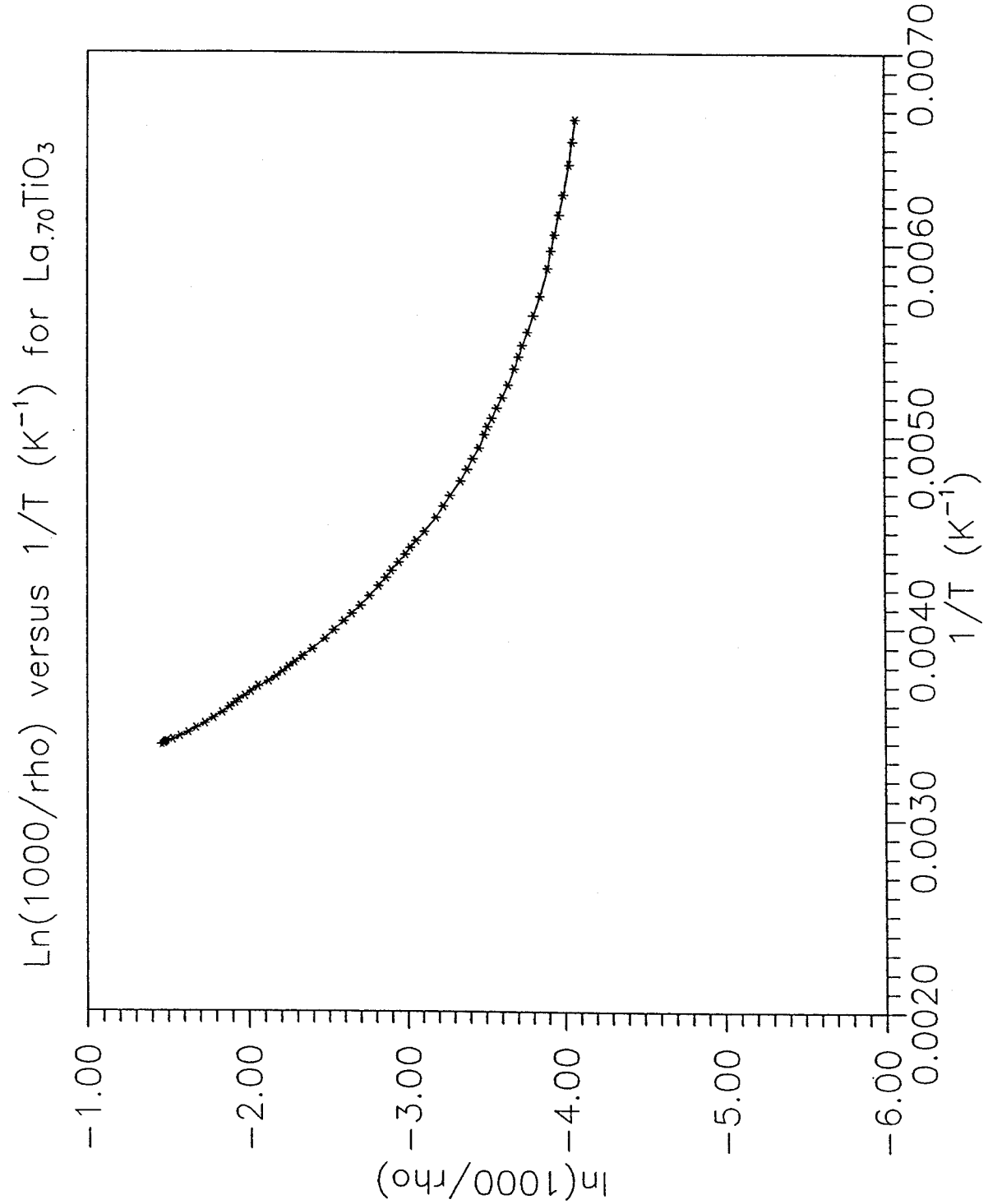

Figure 4.3 Resistivity versus temperature for $La_{.75}TiO_3$.

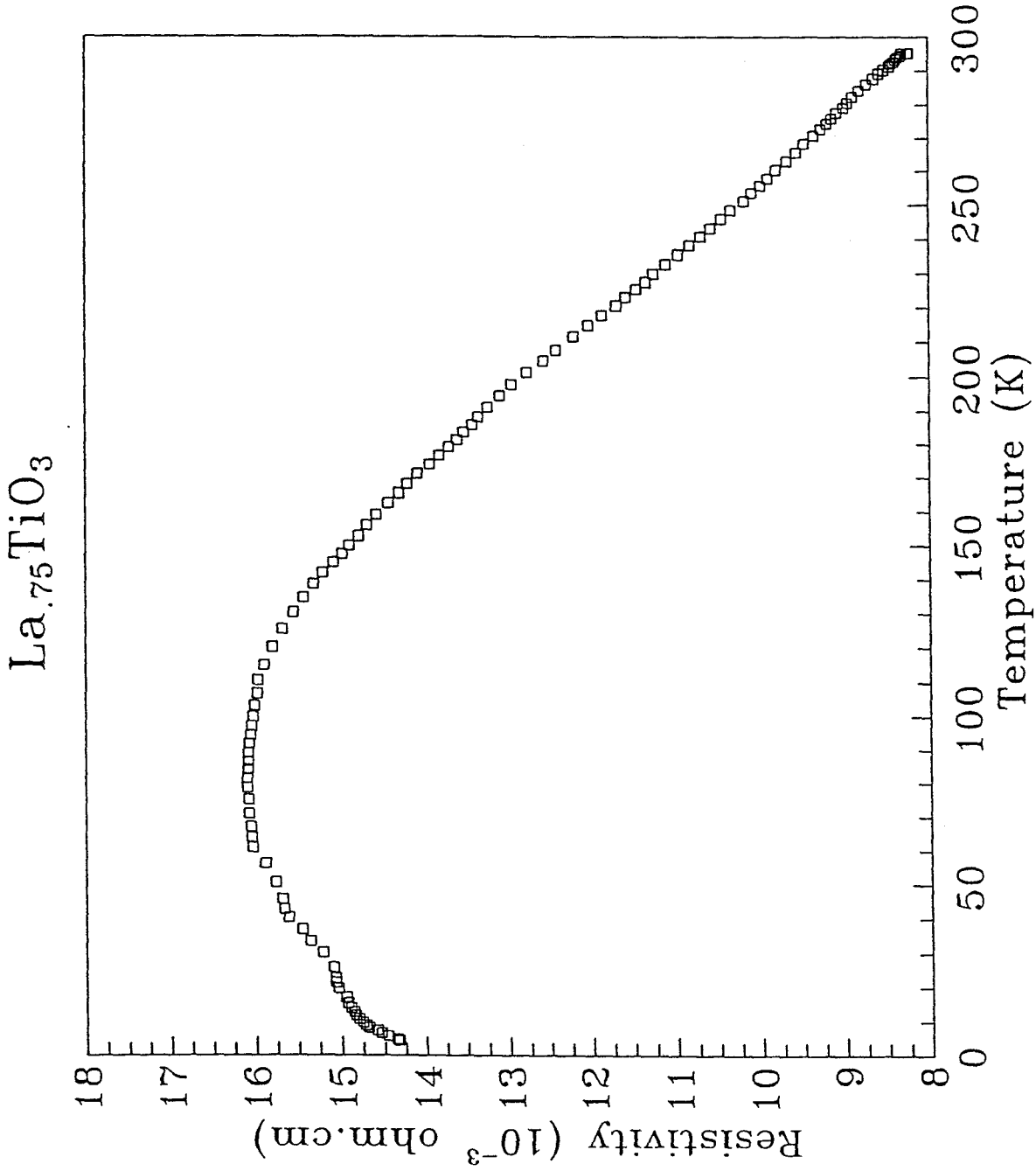

Figure 4.4 Plot of ln(1000/ρ) versus 1/temperature for $La_{.75}TiO_3$.

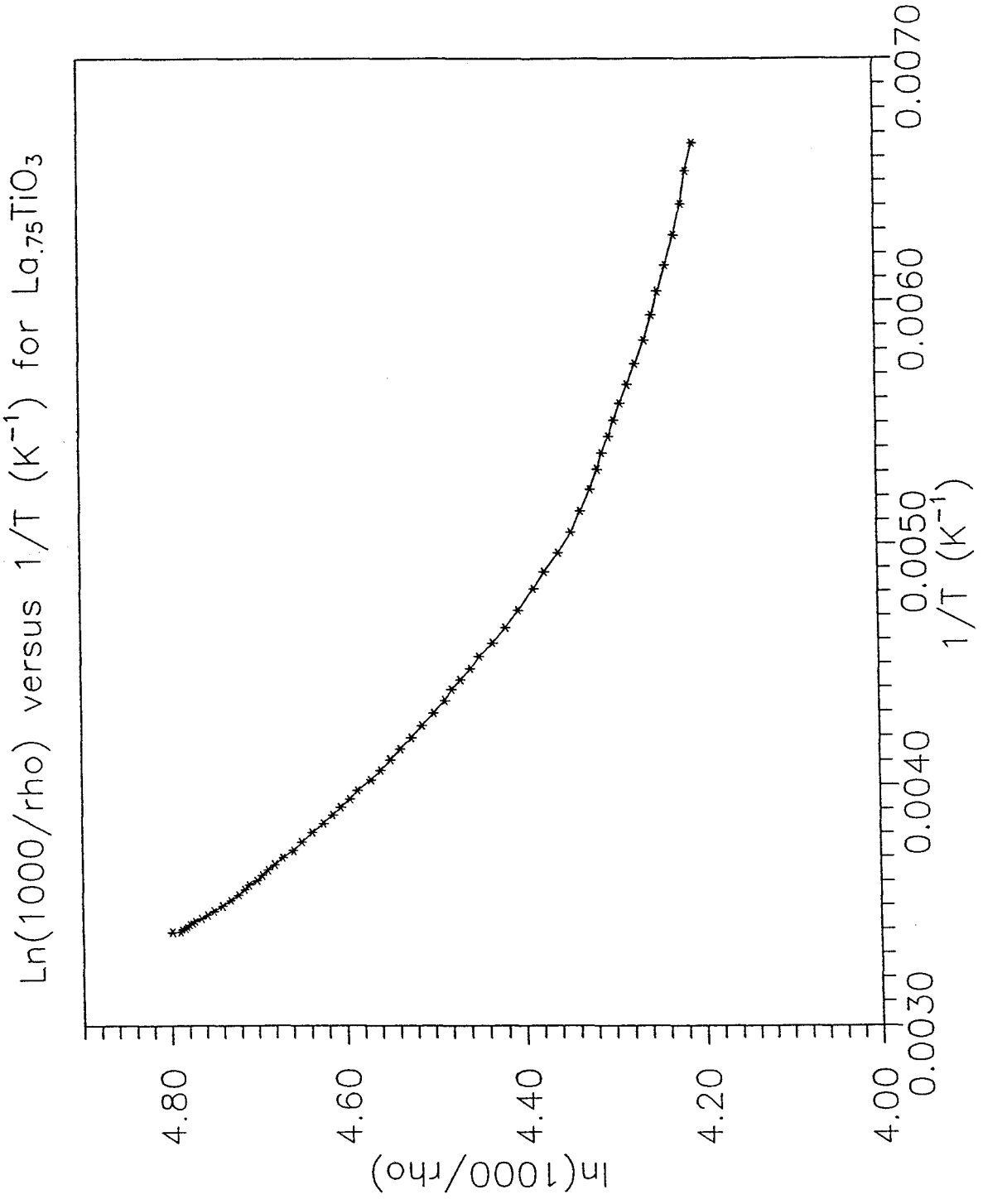

Figure 4.5 Resistivity versus temperature for $La_{.80}TiO_3$.

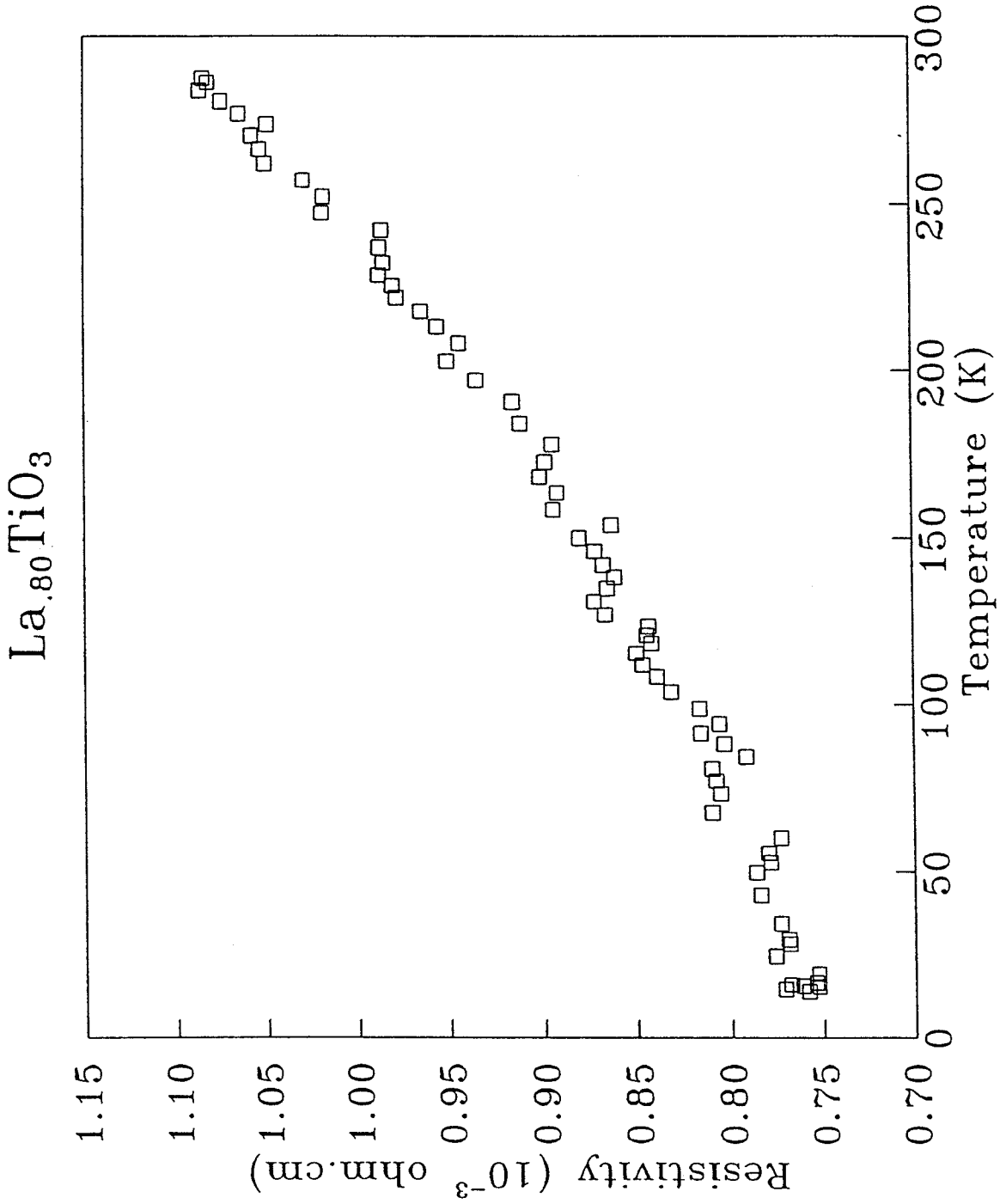

Figure 4.6 Magnetic susceptibility versus temperature for $La_{.70}TiO_3$.

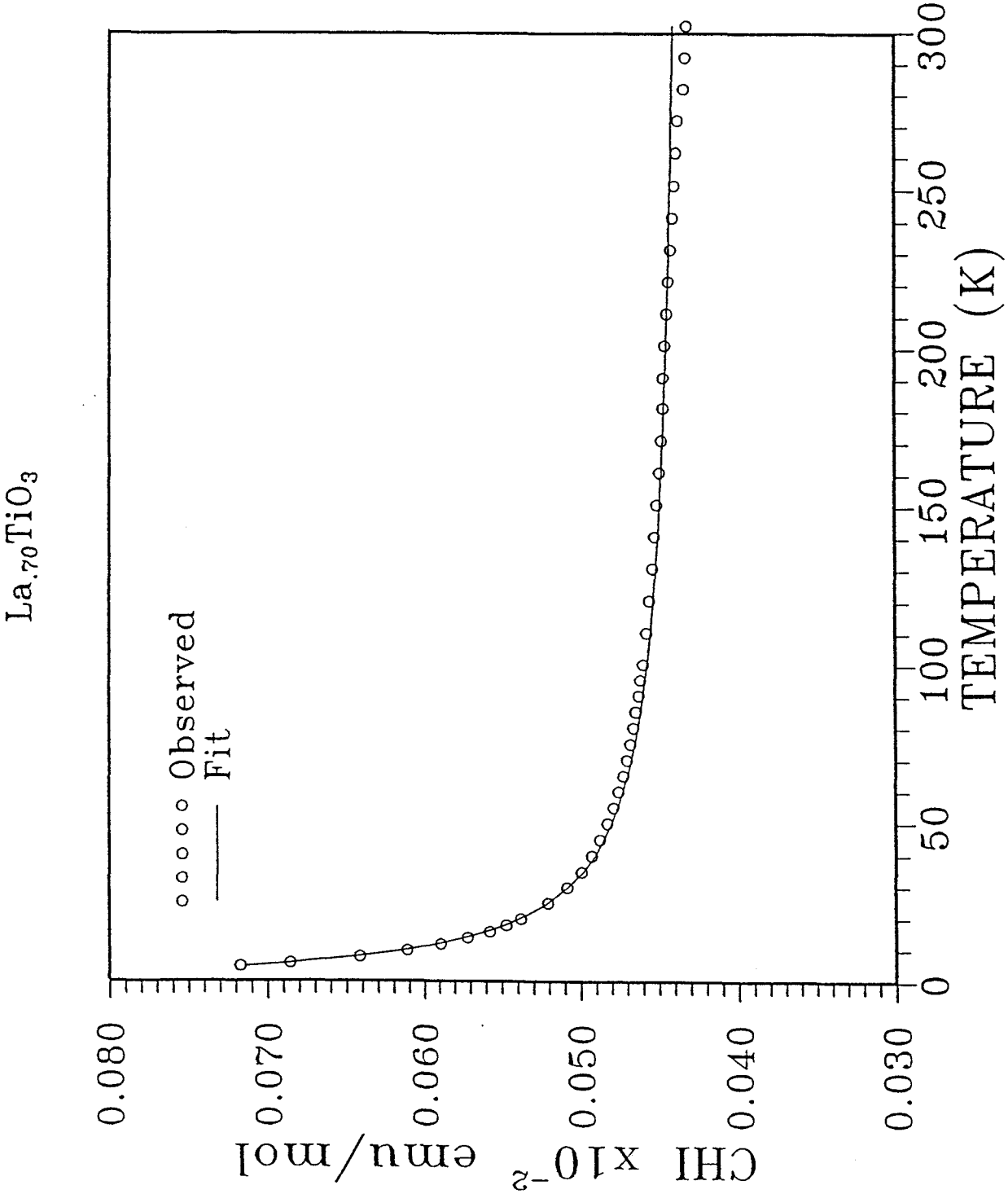

Figure 4.7 Magnetic susceptibility versus temperature for $La_{.75}TiO_3$.

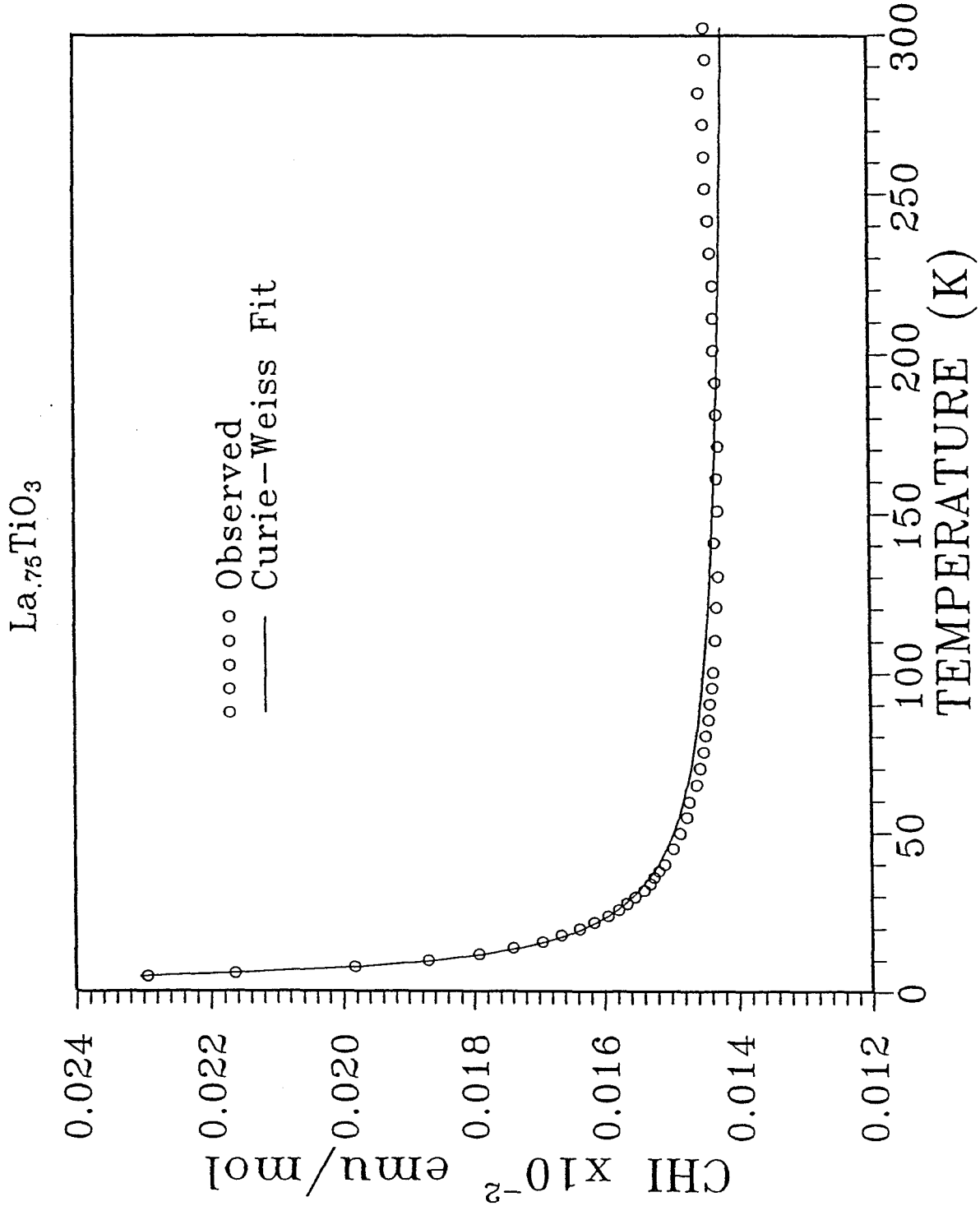

Figure 4.8 Magnetic susceptibility versus temperature for $La_{.80}TiO_3$.

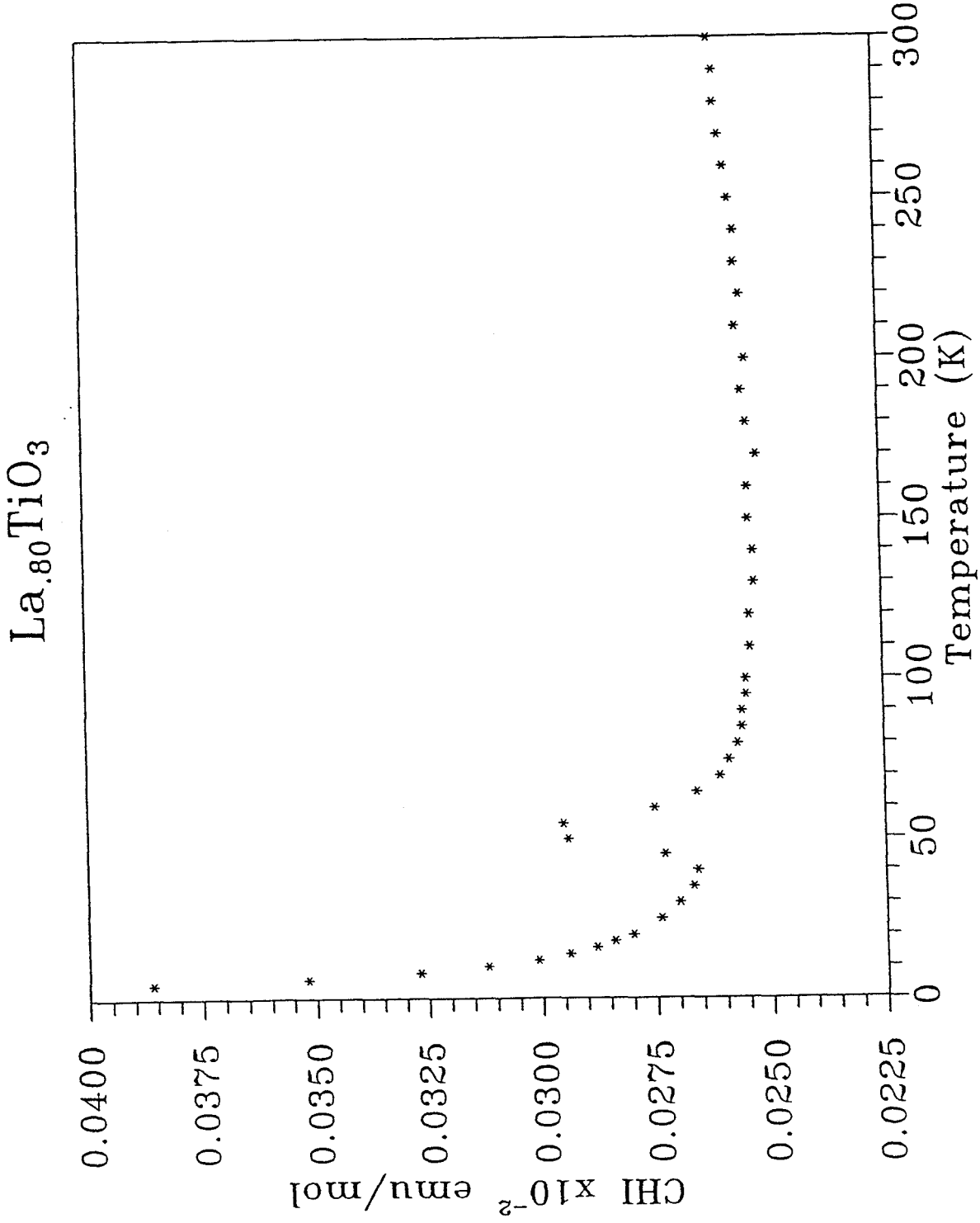

Figure 4.9 Magnetic susceptibility versus temperature for $La_{.88}TiO_3$.

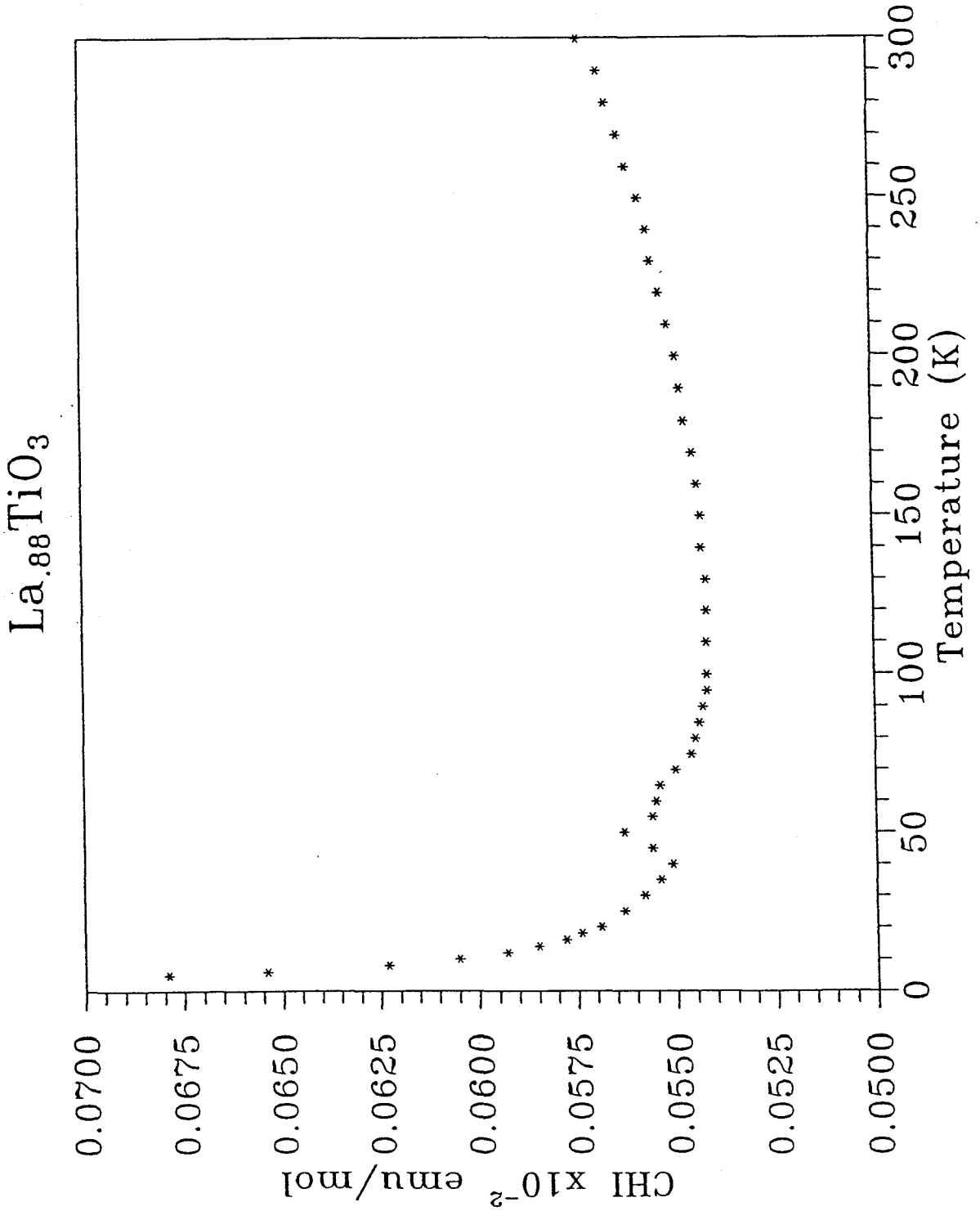

Figure 4.10 Magnetic susceptibility versus temperature for $La_{.92}TiO_3$.

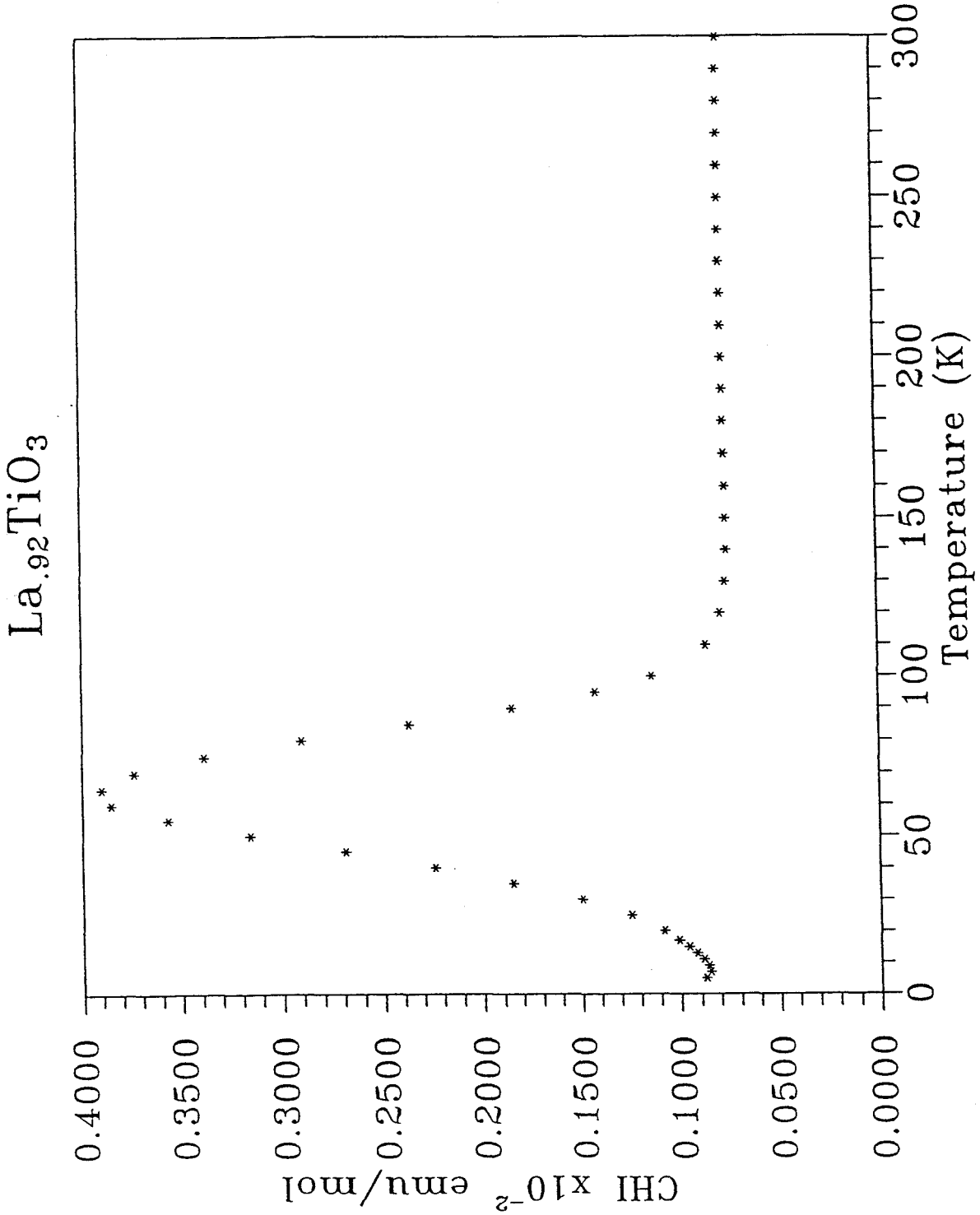

Chapter 5

Conclusions

It has been shown that compounds in the series $La_{1-x}TiO_3$ with $x \leq \frac{1}{8}$ can be prepared as single phases. Single crystals of $La_{.67}TiO_3$ can be grown from a KF-Borax flux, and $La_{.75}TiO_3$ and $La_{.80}TiO_3$ can be prepared by tri-arc melting of the powder materials. All of the samples studied, x = 0.08, 0.12, 0.20, 0.25, 0.30, and 0.33 were characterized by x-ray and neutron diffraction techniques.

All of the samples analyzed had a distorted perovskite type structure where the a and c axes were equivalent to the face diagonals and b was twice the length of the ideal cubic perovskite structure. An ordering of the lanthanum cations and A-site cation vacancies was the cause of the distortion for the compounds of the Pmnm space group. Octahedral tilting was the cause of the distortions in both the Imma and Pnma space groups due to accommodation of the larger Ti^{3+} cations.

Throughout the series, two structural transitions were

observed, Figure 5.1. The first transition occurred at a Ti^{3+} concentration of 28%, where the symmetry changed from the Pmnm of the $La_{.67}TiO_3$ and $La_{.70}TiO_3$ samples to Imma. The second transition occurred at a Ti^{3+} concentration of 64%. At this point, the symmetry changed from the Imma of $La_{.75}TiO_3$ and $La_{.80}TiO_3$ to Pnma. The remaining compounds in the series, $La_{.88}TiO_3$ and $La_{.92}TiO_3$, were of the Pnma symmetry class.

Figure 5.1 Structural transition points in $La_{1-x}TiO_3$.

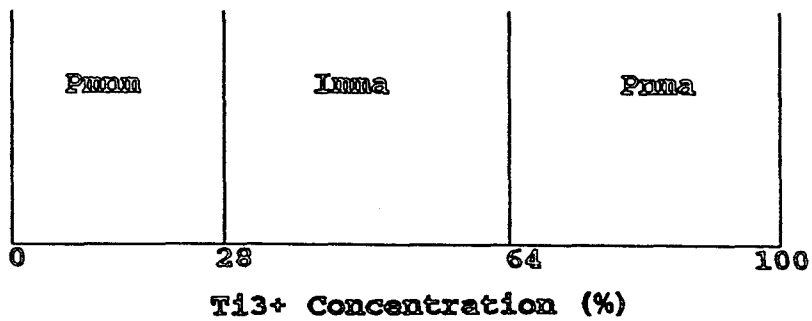

These transitions in the $La_{1-x}TiO_3$ system arise from lack of space within the unit cell. As the Ti^{3+} concentration increases, distortions occur to accommodate the larger cation. As a result of these distortions, Ti-O bond lengths were found to increase throughout the series, Table 5.1. It was also found that distortion of the unit cell increases as Ti^{3+} increases. This can be seen by looking at the decrease in the Ti-O-Ti bond angles on moving from $La_{.67}TiO_3$ to $LaTiO_3$, Table 5.1.

Most of the bond lengths for samples analyzed by both single crystal x-ray diffraction and powder neutron

diffraction were comparable to within 3σ. A few bond lengths beyond this limit were observed. The Ti2-O3 bond lengths calculated for the $La_{.67}TiO_3$ sample and the Ti-O1 bond lengths for the $La_{.75}TiO_3$ sample were found to have the greatest deviation. This problem can be explained by looking at the variations in refined atomic positions of the oxygen atoms from both the x-ray diffraction and neutron diffraction results. The refined positions for the oxygen atoms vary considerably between the two studies. The calculated precision in fractional atomic coordinates was found to be higher in the refined positions for the single crystal x-ray diffraction results, and these atomic positions may better describe the actual geometry of the structure. The variations in certain bond lengths do not affect the overall trends found for the structural properties of the compounds analyzed, Table 5.1.

This result was similar to that observed in the $LaTiO_3$ system doped with strontium as reported by Sunstrom et al.[11] In the strontium doped system, transitions occurred are Ti^{3+} levels of 26% and 80%, Figure 5.2.

Figure 5.2 Structural transition points in $La_{1-x}Sr_xTiO_3$.[11]

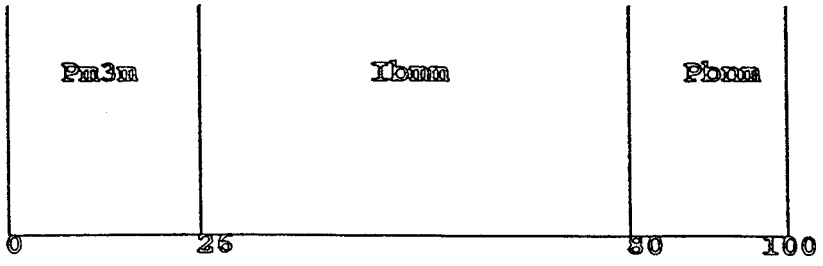

The unit cell parameters for this series were also found to fit the distorted perovskite structure. The cause for the distortions were attributed to octahedral tilting within the lattice, with angles between octahedra ranging from 156.24(1)° to 161.91(1)° in the c-direction, and between 154.32(1)° and 170.47(1)° in the ab plane. Samples below a Ti^{3+} concentration of 26% were analyzed by Guinier diffraction and were assigned to cubic symmetry.

The barium doped system of Sunstrom et al.[13] was very similar to the strontium doped system. Two structural transitions were observed at Ti^{3+} concentrations of 30% and 80%, Figure 5.3. At 30%, the structural transition was found to be between the cubic Pm3m symmetry and the orthorhombic Ibmm symmetry. At 80%, the transition was found to be between that of Ibmm and Pbnm. The unit cells were assigned based on a distorted perovskite structure, but no structural data was given to account for the distorted structure.

Figure 5.3 Structural transition points in $La_{1-x}Ba_xTiO_3$.[13]

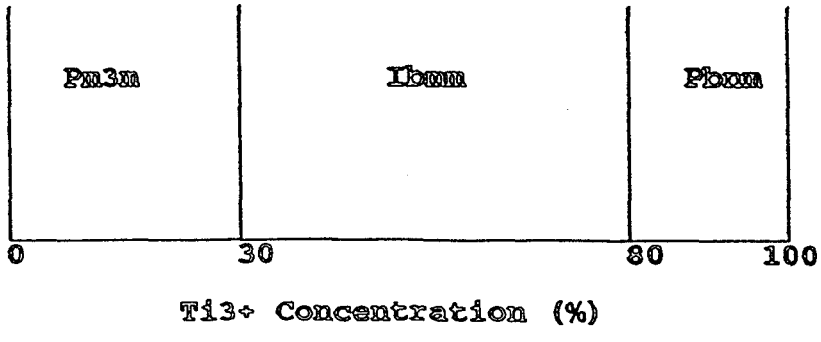

The barium doped system of Eylem et al.[14] behaved quite differently than that of Sunstrom et al.[13] Two transition points were observed, but the assigned symmetry of the compounds was different. Eylem et al.[14] observed a symmetry change between P4mm and Pm3m at a Ti^{3+} concentration of 15%. A second transition was found at 80% between Pm3m and Pbnm, Figure 5.4.

Figure 5.4 Structural transition points in $La_{1-x}Ba_xTiO_3$.[14]

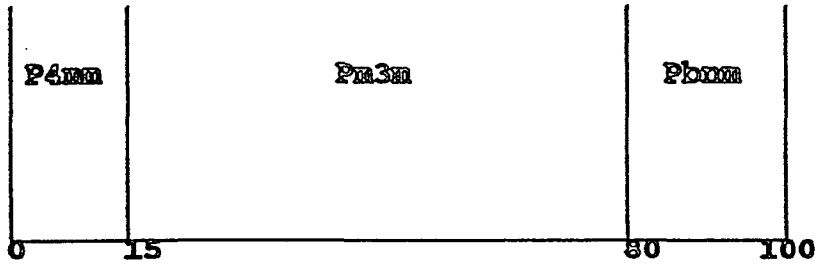

The only distorted perovskite structures observed were those belonging to the Pbnm space group. A detailed structural analysis was not reported.

The $LaTiO_{3+x}$ system of Lichtenberg et al.[20] also had two structural transition points, Figure 5.5. At a Ti^{3+} concentration of 21% there is a transition from a monoclinic phase to a mixed phase involving the orthorhombic phase and a 2D monoclinic phase, where samples with the orthorhombic

symmetry have unit cell parameters expected for the distorted perovskite structure. The second transition occurs at Ti^{3+} concentration of 57%. Here, the mixed phase state becomes a single phase of orthorhombic symmetry. The 2D monoclinic structure is described as being made up of perovskite slabs connected by lanthanum cations.

Figure 5.5 Structural transition points in $LaTiO_{3+x}$.[20]

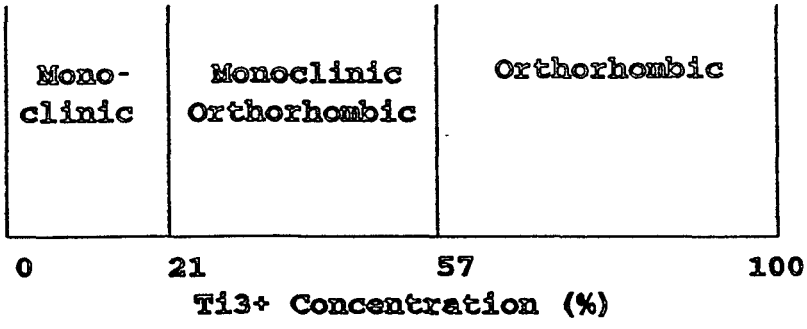

The results obtained for the $La_{1-x}TiO_3$ system in the present study are similar to each of the studies done previously in the fact that a number of structural transitions occur throughout the series of compounds as a function of Ti^{3+} concentration.

Electrical measurements on the $La_{1-x}TiO_3$ series of compounds show an unexpected behavior which may be indicative to a transition point at a critical Ti^{3+} concentration of 28%. Here the properties observed were not characteristic of a

resistivity decreases. This is expected since there is an

semiconductor or a metal. As the temperature was decreased from 300K, the resistivity increased to a maximum and then decreased slightly as the temperature was lowered to 5K.

At a Ti^{3+} concentration above 64%, the room temperature resistivity began to rise.[21] This is in agreement with the structural change to a lower symmetry at this Ti^{3+} concentration. At a Ti^{3+} concentration approaching 100%, the electrical properties become semiconducting again[2], Figure 5.6.

Figure 5.6 Electrical transition points in $La_{1-x}TiO_3$.

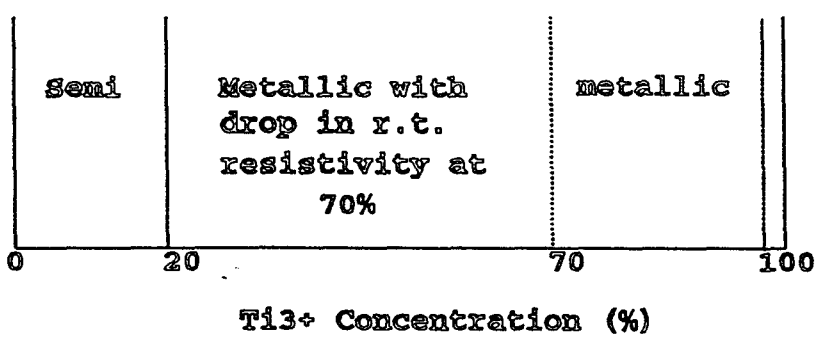

These transitions in electrical properties can be explained by looking at the Ti-O-Ti bond angles as well as the Ti^{3+} concentrations.

As the concentration of Ti^{3+} is increased, the resistivity decreases. This is expected since there is an increase in the carrier concentration. Further in the series it was found that on going from the Imma class of compounds to

the Pnma class, the resistivity increased. This can be explained by looking at the degree of overlap between titanium t_{2g} and oxygen $2p_{\pi}$ orbitals within the structure. It was found that the Ti-O-Ti bond angles decreased at these higher Ti^{3+} concentrations. This minimizes the orbital overlap necessary for conductivity within the material. Although the carrier concentration is high, resistivity values increase due to the reduced π overlap between orbitals.

These results are in agreement with those reported by Sunstrom et al.[11] for the strontium doped system. A semiconductor - metal transition was found at a Ti^{3+} concentration of approximately 20%. Another feature of the strontium doped system was the occurrence of a drop in the room temperature resistivity in compounds with a Ti^{3+} concentration greater than 70%. This is coincident with the structure change from the Pbnm structure to the Ibmm structure, Figure 5.7

Figure 5.7 Electrical transition points in $La_{1-x}Sr_xTiO_3$.[11]

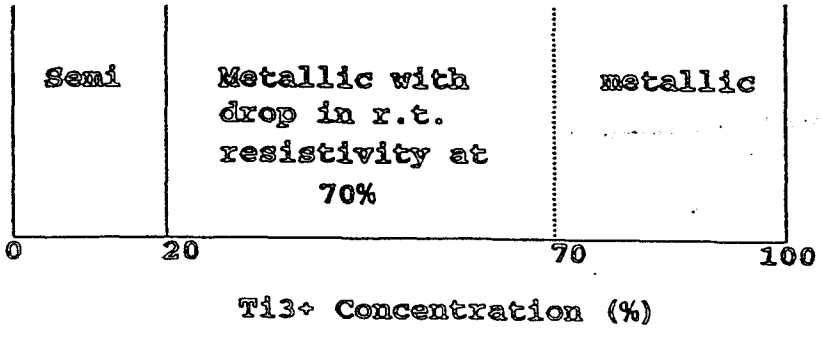

The work of Eylem et al.[14] on the barium doped system shows a semiconductor - metal transition at a Ti^{3+} concentration of approximately 20%. This transition is coincident with the structural transition noted for this series. Figure 5.8. This was the only transition in electrical properties noted in this report for the $La_{1-x}Ba_xTiO_3$ system.

Figure 5.8 Electrical transition points in $La_{1-x}Ba_xTiO_3$.[14]

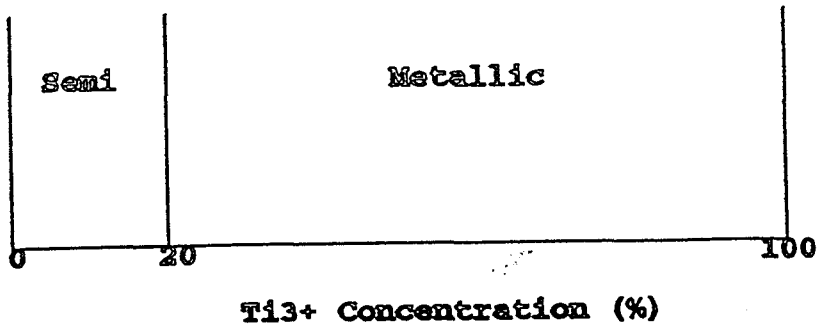

Two transitions were observed in the $LaTiO_{3+x}$ system reported by Lichtenberg et al.[20], Figure 5.9. The first being a semiconductor - metal transition occurring at a Ti^{3+} concentration of 45%. This transition was not coincident with any structural transitions observed, and does not correlate well with the reports on the strontium and barium doped systems. Another transition from a metallic state to a semiconducting state was observed at a Ti^{3+} concentration of 84%. Again, this transition does not correspond to a structural transition, and is the only transition in this Ti^{3+} composition range to be reported for the $LaTiO_3$ system doped

with vacancies or basic cations.

Figure 5.9 Electrical transition points in $LaTiO_{3+x}$.[20]

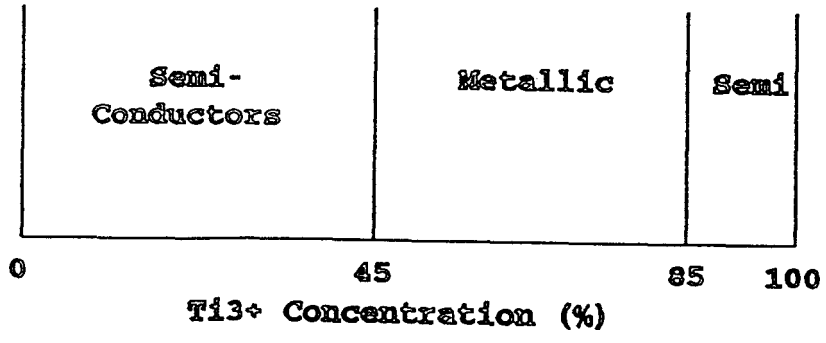

The results obtained for the semiconductor - metal transition in the $La_{1-x}TiO_3$ system agree well with studies conducted on strontium and barium doped systems, where the transition point is coincident with the transition point observed in structural properties.

The magnetic properties were also found to be dependent upon the Ti^{3+} concentration of the individual samples. Variations in magnetic properties were found to coincide with structural and electrical transitions, Figure 5.10. At a Ti^{3+} concentration of 28%, there was a notable drop in the measured room temperature magnetic susceptibility on moving from the Pmnm symmetry to the Imma symmetry. At a Ti^{3+} concentration of 64%, the magnetic susceptibility became temperature dependent over the entire temperature range studied, as opposed to those

samples where the susceptibility was temperature dependent only below 50K. Antiferromagnetic coupling was observed at a Ti^{3+} concentration of 76%. This feature does not coincide with a structural or electrical transition, but does show that the magnetic ordering of $LaTiO_3$ is not totally destroyed at this composition.

Figure 5.10 Magnetic transition points in $La_{1-x}TiO_3$.

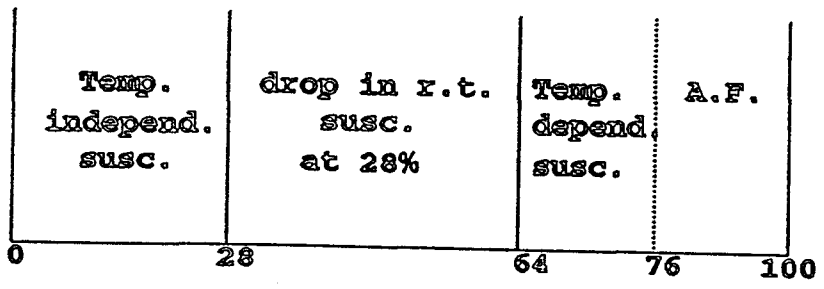

The magnetic properties of the strontium doped system were similar to the results found for the $La_{1-x}TiO_3$ system. Reports from Sunstrom et al.[11] show that the samples are paramagnetic in the low temperature range, and temperature independent in the high temperature range. No obvious transitions were reported except for the occurrence of ferromagnetism at a Ti^{3+} concentration of 95%. The magnetic ordering of the $LaTiO_3$ system is preserved until this point, but is destroyed at lower Ti^{3+} concentrations.

The barium doped system of Sunstrom et al.[13] is more like the $La_{1-x}TiO_3$ system studied. There is an increase in the room temperature magnetic susceptibility for a Ti^{3+} concentration of approximately 30%, Figure 5.11. This is coincident with the structural transition reported on the shift from cubic to orthorhombic symmetry. It has also been found that the magnetic ordering of $LaTiO_3$ is destroyed at a Ti^{3+} concentration of 80%. This corresponds to the same Ti^{3+} concentration at which the second structural transition takes place.

Figure 5.11 Magnetic transition points in $La_{1-x}Ba_xTiO_3$.[13]

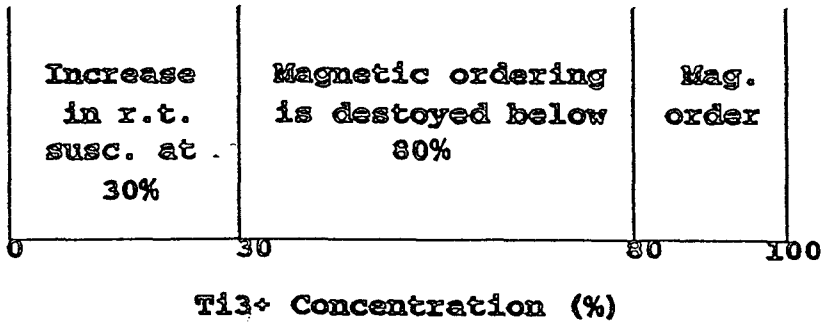

The reports on magnetic properties by Eylem et al.[14] for the barium doped system show all of the samples to have Pauli like temperature independent susceptibilities where the susceptibility values increase with increasing Ti^{3+} content.

The $LaTiO_{3+x}$ system reported by Lichtenberg et al. showed paramagnetic susceptibilities in the low temperature regions

when the Ti^{3+} concentrations were above 80%. Below this composition, the magnetic properties became complex and were neither reported nor explained. The transition at 80% corresponds to the transition found for the electrical properties, and compares well with results found for the present $La_{1-x}TiO_3$ system.

The transitions found in structural, electrical, and magnetic properties can all be related to a single parameter, the Ti^{3+} concentration, as determined from the present study. Figure 5.12 shows the correlation between properties as a function of the Ti^{3+} concentration, and Tables 5.1 and 5.2 summarize the structural, electrical and magnetic results found throughout this study.

It has also been found that the Ti^{3+} concentration has a direct effect on the size of the unit cell. As the Ti^{3+} concentration is increased, the size of the unit cell increases proportionally, Figure 5.13.

Although these transitions can be traced to the Ti^{3+} concentration, other factors may also play a role in determining transition points within the series. Further studies could be carried out to determine whether or not other factors do effect the structural and physical properties of the $La_{1-x}TiO_3$ system.

Table 5.1 Bond distances and angles for the $La_{1-x}TiO_3$ series based on neutron diffraction.

Comp.	Space Group	Ti-O1 (Å)	Ti-O2 (Å)	Ti-O3 (Å)	<Ti-O> (Å)
$La_{.67}TiO_3$	Pmnm	1.93 1.96	2.02 1.92	2.02 1.80	1.94
$La_{.70}TiO_3$	Pmnm	1.93 1.98	2.08 1.94	1.91 1.85	1.95
$La_{.75}TiO_3$	Imma	1.96	1.95	--	1.95
$La_{.80}TiO_3$	Imma	1.98	1.97	--	1.97
$La_{.88}TiO_3$	Pnma	1.99	2.04 1.98	--	2.00
$La_{.92}TiO_3$	Pnma	2.03	2.01 2.04	--	2.02
$La_{1.0}TiO_3$	Pnma	2.03	2.03 2.04	--	2.03

Bond angles around titanium octahedra

Comp.	Space Group	Ti-O1-Ti (°)	Ti-O2-Ti (°)	<Ti-O-Ti> (°)
$La_{.67}TiO_3$	Pmnm	180.0	180.0	180.0
$La_{.70}TiO_3$	Pmnm	180.0	180.0	180.0
$La_{.75}TiO_3$	Imma	166.8	179.1	173.0
$La_{.80}TiO_3$	Imma	163.0	167.9	165.5
$La_{.88}TiO_3$	Pnma	164.5	157.1	160.8
$La_{.92}TiO_3$	Pnma	153.3	156.2	154.8
$La_{1.0}TiO_3$	Pnma	154.8	154.0	154.4

Table 5.2 Structural, electrical, and magnetic properties of the $La_{1-x}TiO_3$ compounds.

Compound	Symmetry	Resistivity $(\Omega.cm)^{300k}$	Magnetic Susceptibility χ^{300K} (emu/mol)
$La_{.67}TiO_3$	Pmnm	N/A	N/A
$La_{.70}TiO_3$	Pmnm	4.31	$.047\times10^{-2}$
$La_{.75}TiO_3$	Imma	8.24×10^{-3}	$.015\times10^{-2}$
$La_{.80}TiO_3$	Imma	1.08×10^{-3}	$.026\times10^{-2}$
$La_{.88}TiO_3$	Pnma	4.5×10^{-4}	$.057\times10^{-2}$
$La_{.92}TiO_3$	Pnma	1.1×10^{-3}	$.078\times10^{-2}$
$LaTiO_3$	Pnma	$4.\times10^{-2}$	N/A

Figure 5.12 Plots of 300K resistivity, temperature independent susceptibility, and symmetry as a function of Ti^{3+} concentration.

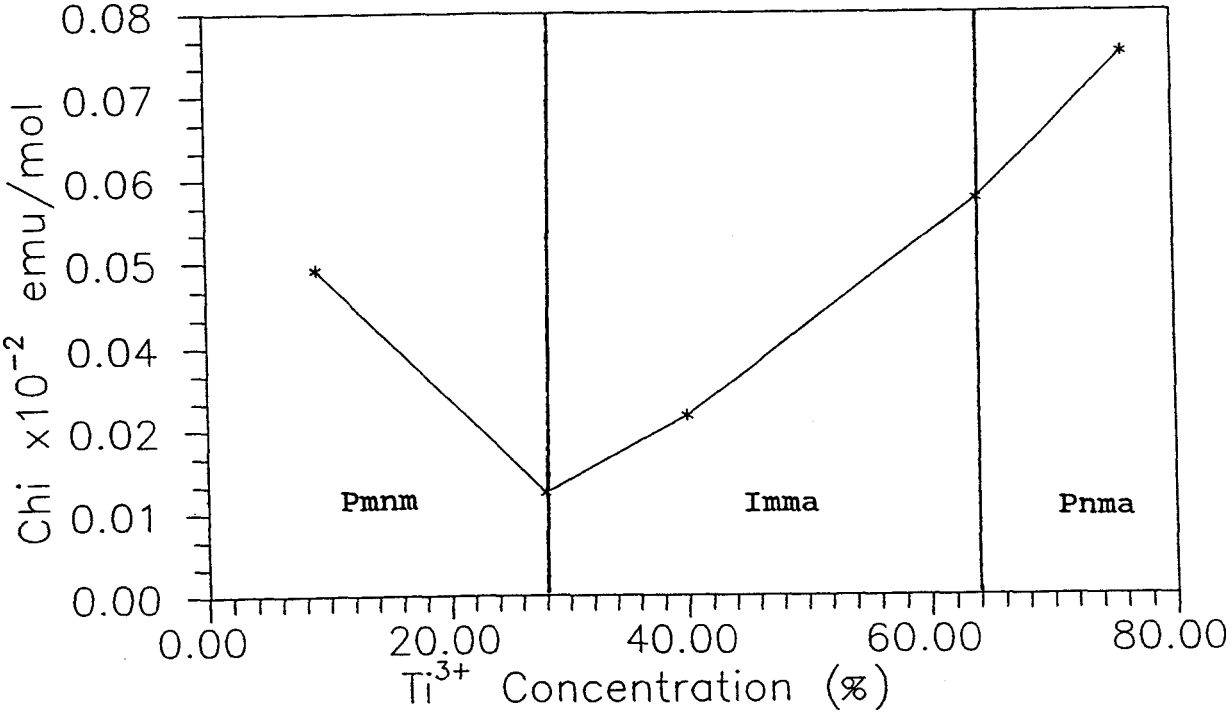

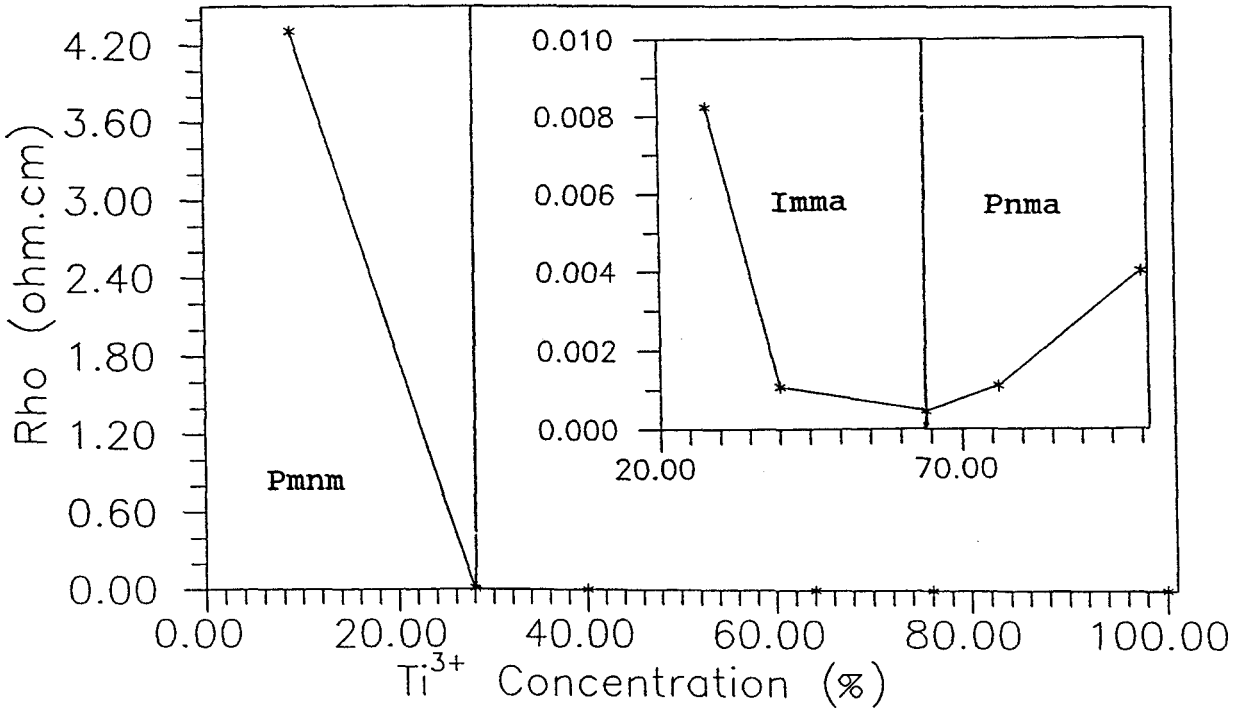

Figure 5.13 Unit cell volume as a function of Ti^{3+} concentration

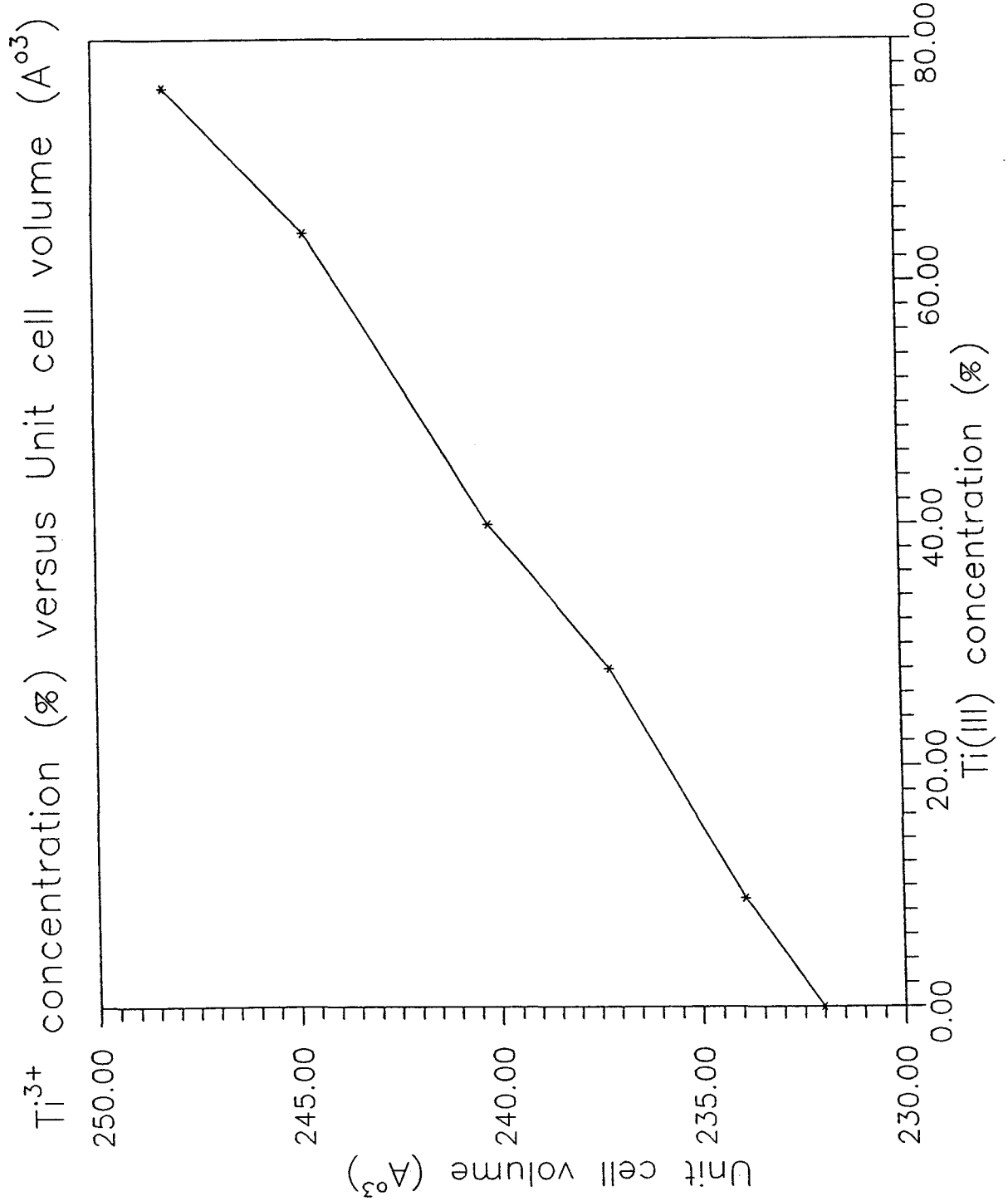

References

1. Wenhe Gong, McMaster University, Master's Thesis, 1990.

2. David Crandles, McMaster University, Ph.D. Thesis, 1992.

3. David MacLean, Hok-Nam Ng, and J.E. Greedan, *Journal of Solid State Chemistry*, **30**, 1979, 35-44.

4. Atsushi Okazaki and Yosutaka Suemune, *Journal of the Physical Society of Japan*, Vol **16**, No.2, 1961, 176-183.

5. A.M. Glazer, *Acta. Cryst.* **A31**, 1975, 756-762.

6. A.M. Glazer, *Acta. Cryst.* **B28**, 1972, 3384-3392.

7. Manfred Eitel and J.E.Greedan, *Journal of the Less Common Metals*, **116**, 1986, 95-104.

8. E.J.W. Verwey, P.W. Haaijman, F.C. Romeijn, and G.W. van Oosterhout, *Philips Res. Rep.*, **5**, 1950, 173-187.

9. Michael Kestigan, John G. Dickinson, and Roland Ward, *JACS*, **79**, 1957, 5598-5601.

10. T.Y. Tien and L.E. Cross, *Japanese Journal of Applied Physics*, Vol.**16**, No.3, 1967, 459-468.

11. Joseph E. Sunstrom IV, Susan M. Kauzlarich, and Peter Klavins, *Chem. Mater.*, Vol.**4**, No.2, 1992, 346-353.

12. W.D. Johnston and D. Sestrich, *J. Inorg. Nucl. Chem.*, Vol.**20**, 1961, 32-38.

13. Joseph E. Sunstrom IV and Susan M. Kauzlarich, Better Ceramics Through Chemistry, MRS Spring 1992 Meeting, Proceedings in press, 1992.

14. Cahit Eylem, Gotthard Saghi-Szabo, Bai-Hao Chen, Bryan Eichhorn, Jian-Liang Peng, Richard Greene, Lourdes Salamanca-Riba, and Sahn Nahm, *Chem. Mater.*, **4**, 1992, 1038-1046.

15. Michael Kestigan and Roland Ward, *JACS*, **77**, 1955, 6199-

6200.

16. Masanori Abe and Kenji Uchino, *Mat. Res. Bull.*, Vol.**9**, 1974, 147-156.

17. A.M. Sych, D.I. Bilyk, V.G. Klenus, T.V. Novik, *Russian Journal of Inorganic Chemistry*, **21**(12), 1976, 1775-1777.

18. G.V. Bazuev, O.K. Makarova, and G.P. Shveikin, *Russian Journal of Inorganic Chemistry*, **23**(6), 1978, 800-802.

19. Mitsunori Yokoyama, *Journal of Crystal Growth*, **96**, 1989, 490-496.

20. F. Lichtenberg, D. Widmer, J.G. Bernorz, T. Williams, and A. Reller, *Z. Phys. B - Condensed Matter*, **82**, 1991, 211-216.

21. D. Crandles, McMaster University, Ph.D. Thesis, 1992.

22. A.L.Dawson, W.R. Datars, J.D. Garrett, and F.S. Razavi, *Journal of Physics - Condensed Matter*, Vol.**1**, No.38, 1989, 6817-6828.

23. Anthony R. West, Solid State Chemistry and Its Applications, John Wiley and Sons, 1984.

24. A. Sakthivel, and R.A. Young, School of Physics, Georgia Institute of Technology, Atlanta, Georgia, 30332, USA.

25. George H. Stout and Lyle H.Jensen, X-ray Structure Determination, A Practical Guide, John Wiley and Sons, 1989.

26. Neil W. Ashcroft and N. David Mermin, Solid State Physics, Holt Rinehart and Winston, 1976.

27. J.B. Cohen, Diffraction Methods in Materials Science, The McMillan Company, 1966.

28. D.L. Bish and J.E. Post, *Reviews in Mineralogy*, Vol.**20**, Modern Power Diffraction, Mineralogical Society of America, 1989.

29. A. Albinati and B.T.M. Willis, *J. Appl. Cryst.*, **15**, 1982, 362-374.

30. H.M. Reitveld, *J. Appl. Cryst.*, **2**, 1969, 65-71.

31. G. Cagliotti, A. Paoletti, and F.P. Ricci, *Nuclear Instruments*, **3**, 1958, 223-228.

32. LAZY-PULVERIX, *J.Appl. Cryst.*, **10**, 1977, 73-74.

33. N. Walker and D. Stuart, *Acta. Cryst.*, **A39**, 1983, 158.

Appendix

X-ray and neutron diffraction refinement profiles for

$La_{1-x}TiO_3$ where x = .67, .70, .75, .80, .88, and .92

Definitions for R-factors calculated during Reitveld profile refinements.

$Rp = 100\Sigma|y_i - y_{ci}|/\Sigma|y_i|$, the pattern R-factor

$Rwp = 100\{\Sigma w_i (y_i - y_{ci})^2/\Sigma w_i y_i^2\}^{1/2}$, the weighted pattern R-factor

$R\text{-exp} = 100\{(N-P+C)/\Sigma w_i y_i^2\}^{1/2}$

$R\text{-Bragg} = 100\Sigma|I_o - I_c|/\Sigma I_o$, R value for Bragg intensities

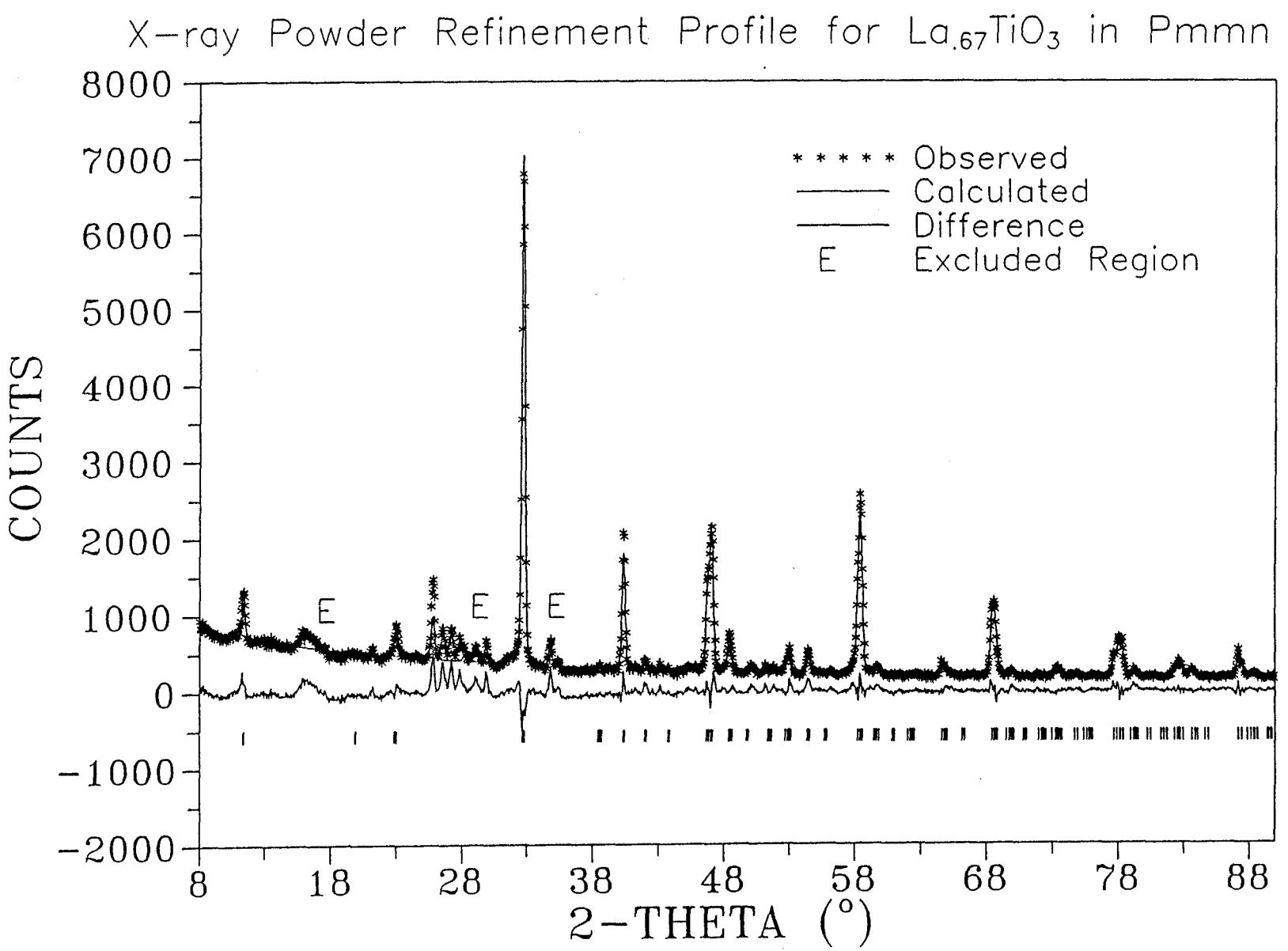
X-ray Powder Refinement Profile for La.67TiO3 in Pmmn
COUNTS
8000
7000
6000
5000
4000
3000
2000
1000
0
-1000
-2000
8
18
28
38
48
58
68
78
88
2-THETA (°)
* * * * * Observed
Calculated
Difference
E Excluded Region
E
E
E

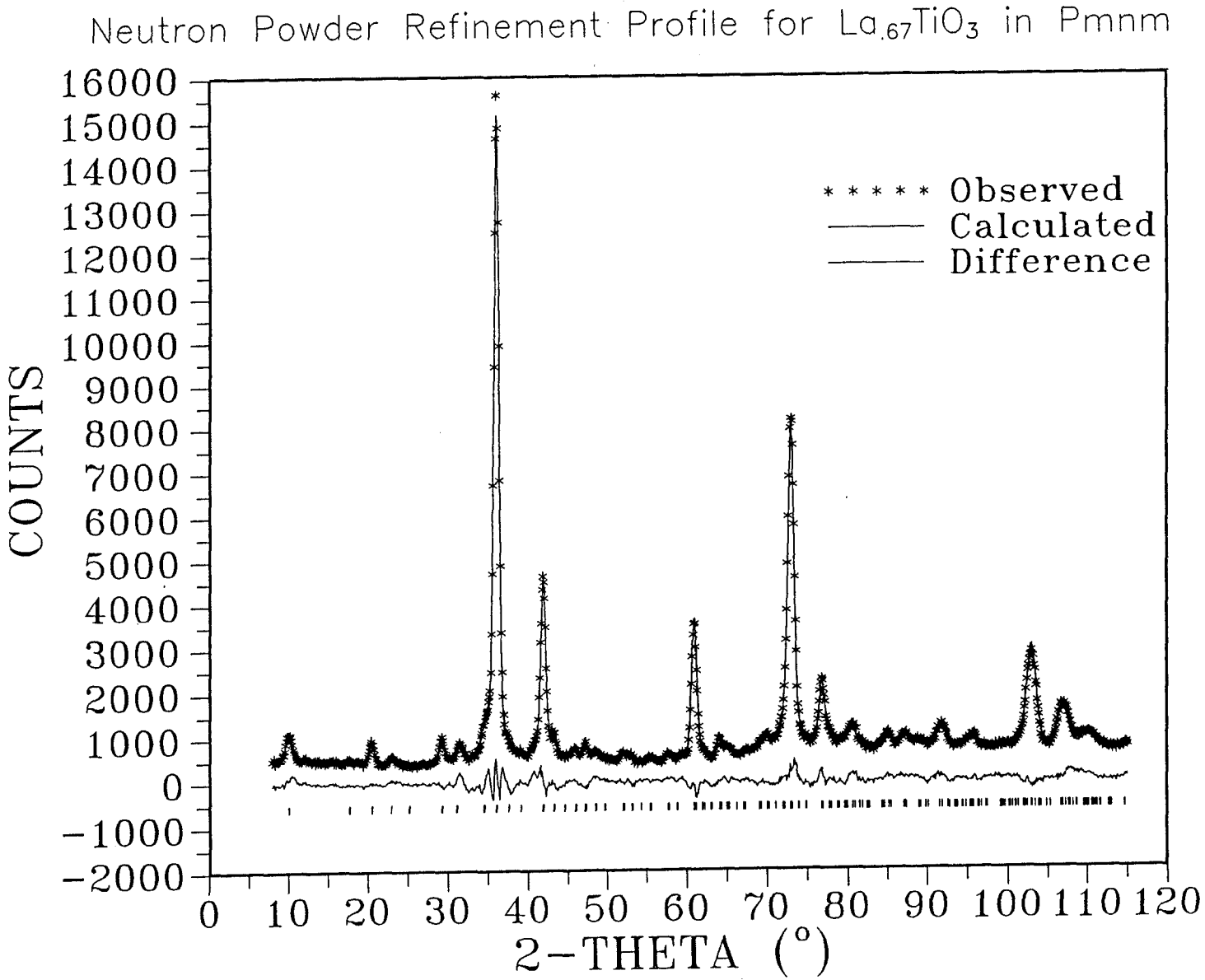
Neutron Powder Refinement Profile for La.67TiO3 in Pmnm
COUNTS
16000
15000
14000
13000
12000
11000
10000
9000
8000
7000
6000
5000
4000
3000
2000
1000
0
-1000
-2000
0 10 20 30 40 50 60 70 80 90 100 110 120
2-THETA (°)
***** Observed
Calculated
Difference

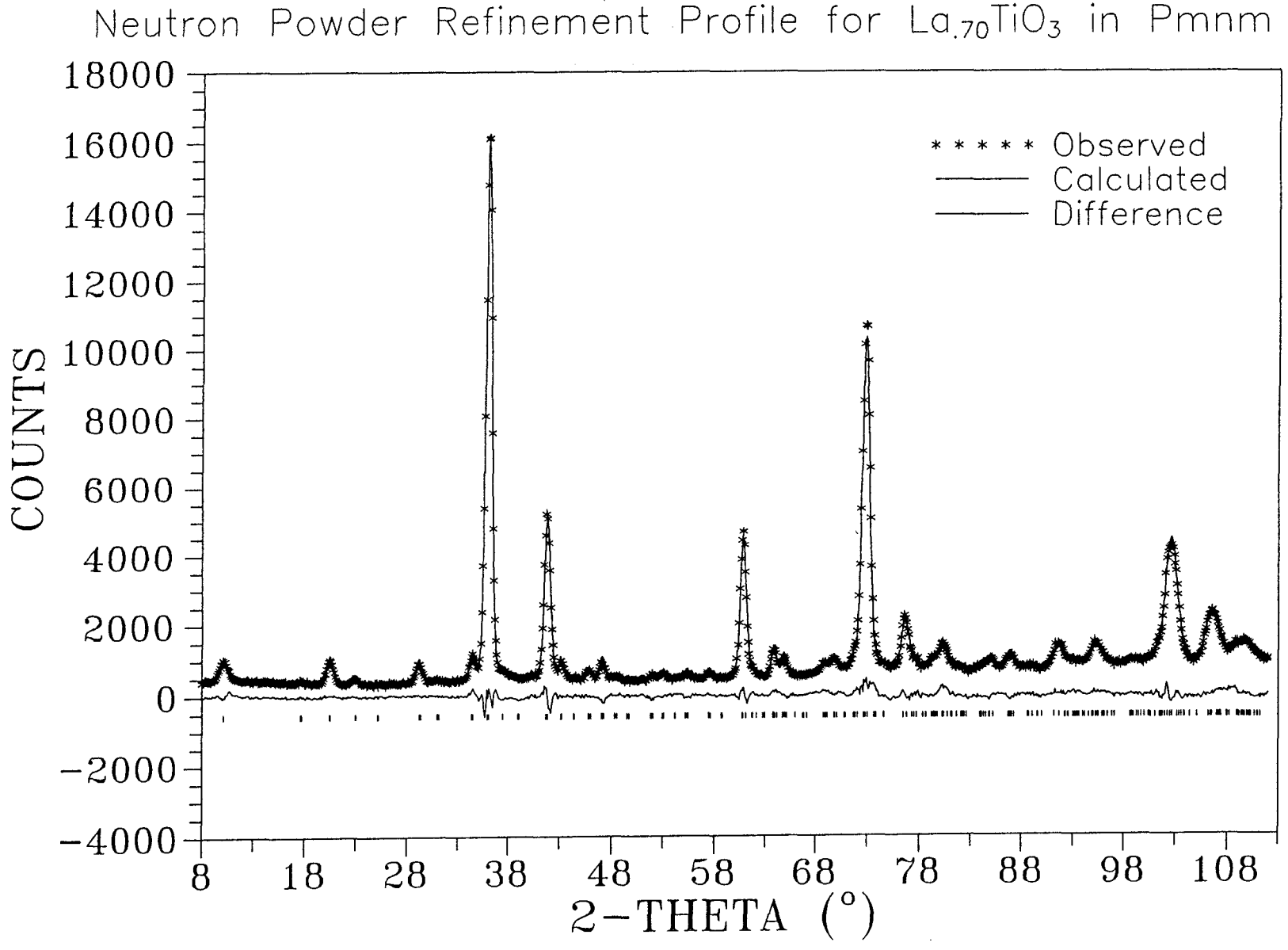
Neutron Powder Refinement Profile for La.70TiO3 in Pmnm
18000
16000
14000
12000
10000
8000
6000
4000
2000
0
-2000
-4000
COUNTS
8
18
28
38
48
58
68
78
88
98
108
2-THETA (°)
***** Observed
Calculated
Difference

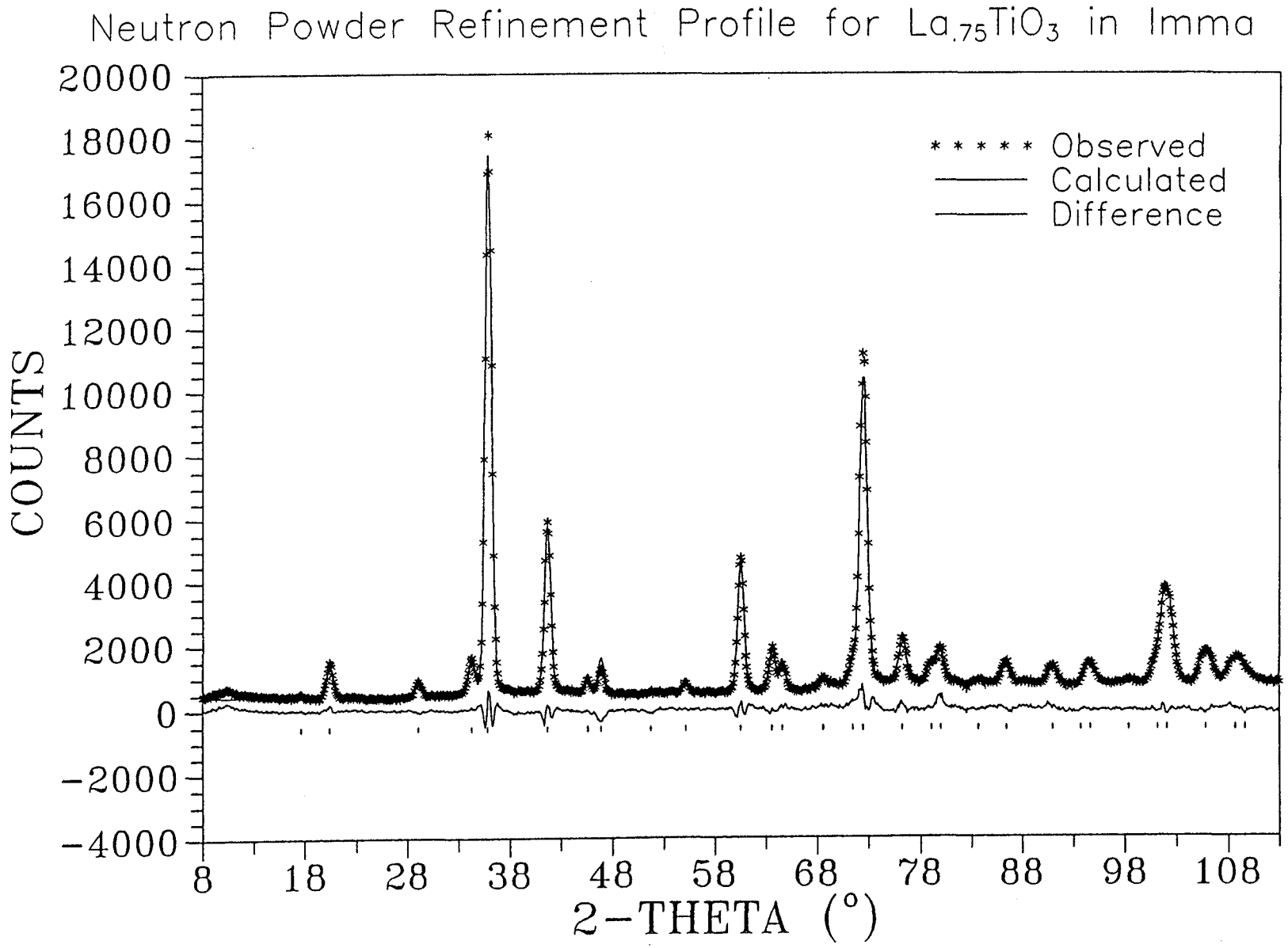
Neutron Powder Refinement Profile for $La_{.75}TiO_3$ in Imma
COUNTS
20000
18000
16000
14000
12000
10000
8000
6000
4000
2000
0
-2000
-4000
8
18
28
38
48
58
68
78
88
98
108
2-THETA (°)
***** Observed
Calculated
Difference

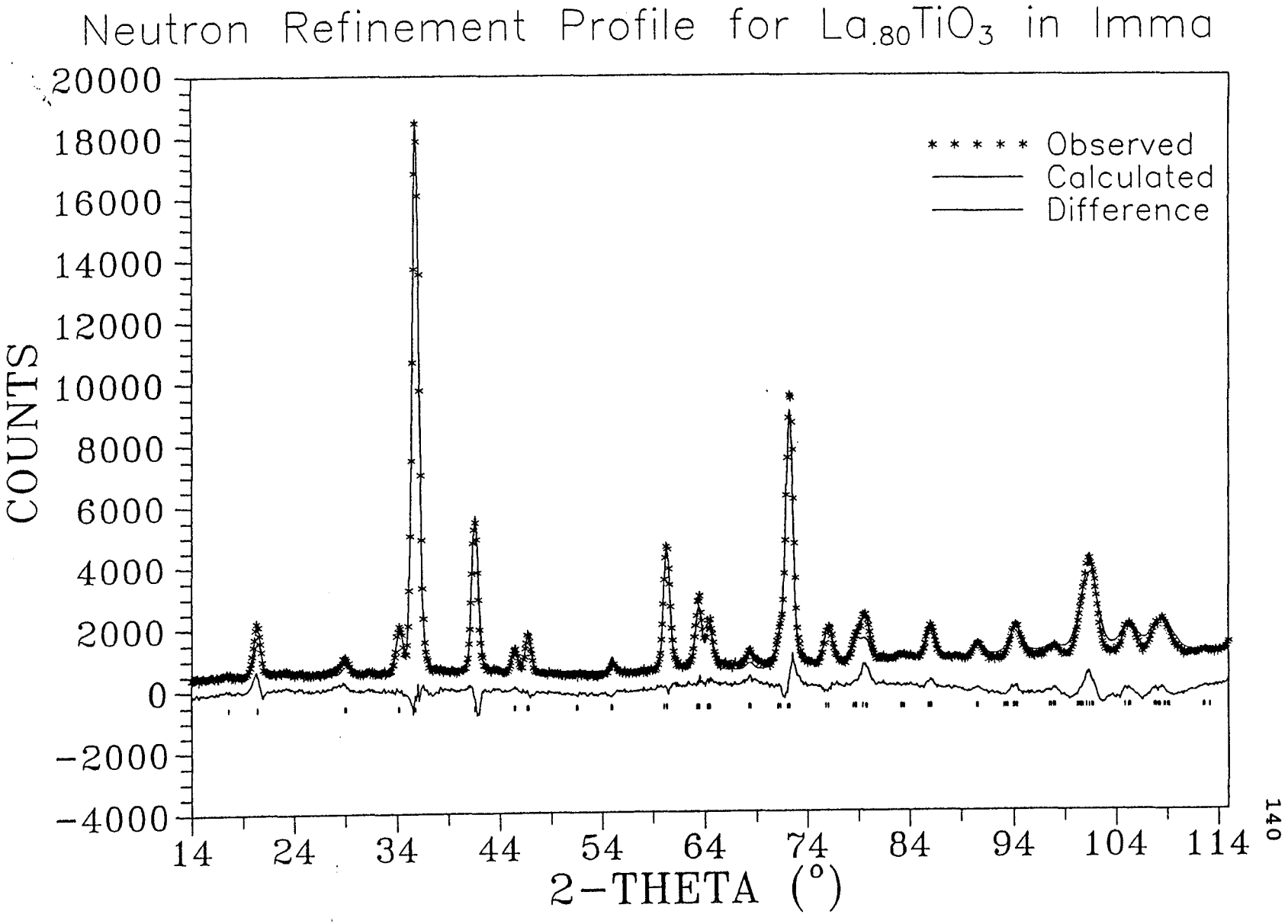
Neutron Refinement Profile for $La_{.80}TiO_3$ in Imma
COUNTS
20000
18000
16000
14000
12000
10000
8000
6000
4000
2000
0
-2000
-4000
14
24
34
44
54
64
74
84
94
104
114
2-THETA (°)
***** Observed
Calculated
Difference

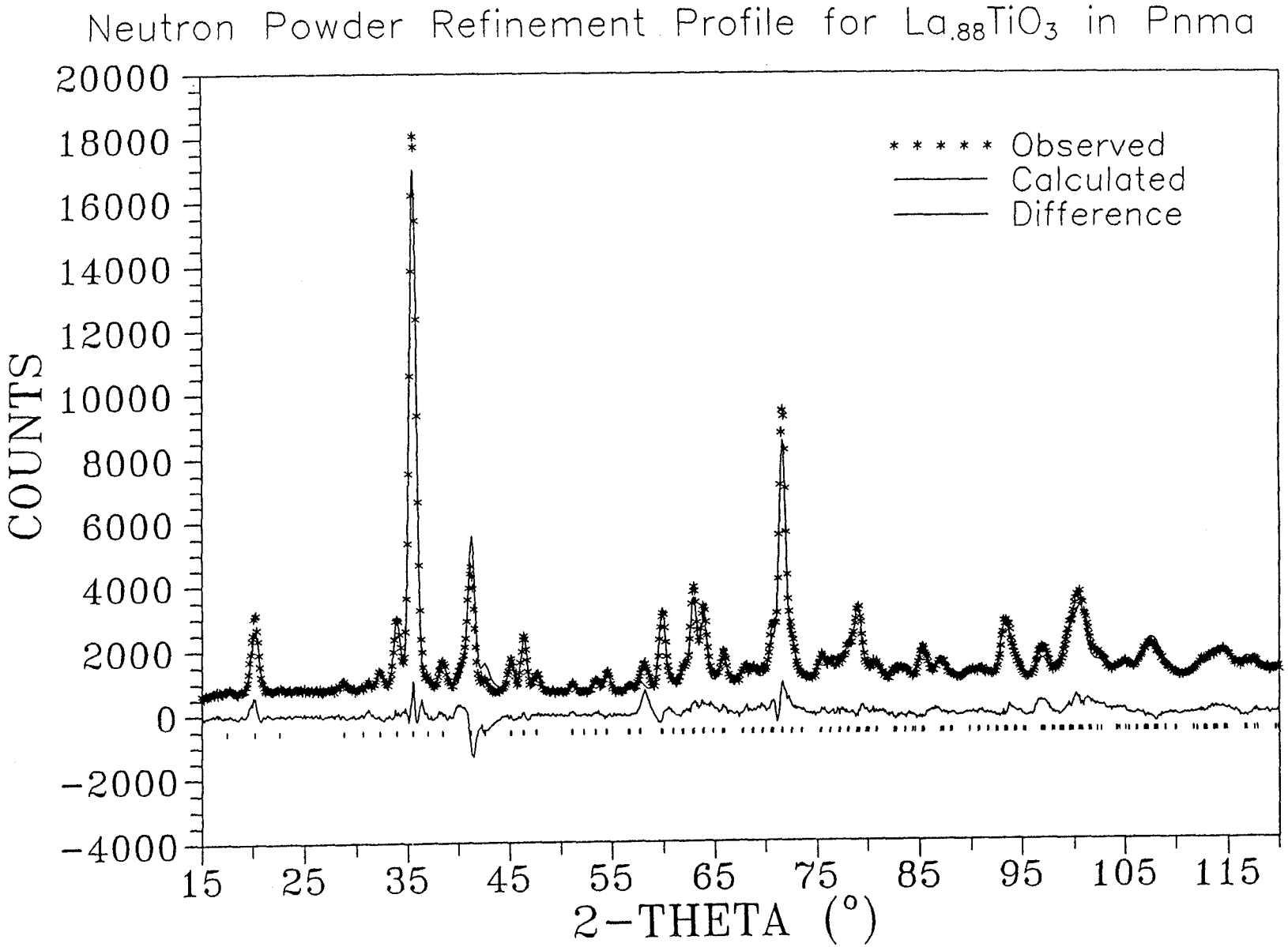
Neutron Powder Refinement Profile for $La_{.88}TiO_3$ in Pnma
COUNTS
20000
18000
16000
14000
12000
10000
8000
6000
4000
2000
0
-2000
-4000
15
25
35
45
55
65
75
85
95
105
115
2-THETA (°)
***** Observed
Calculated
Difference

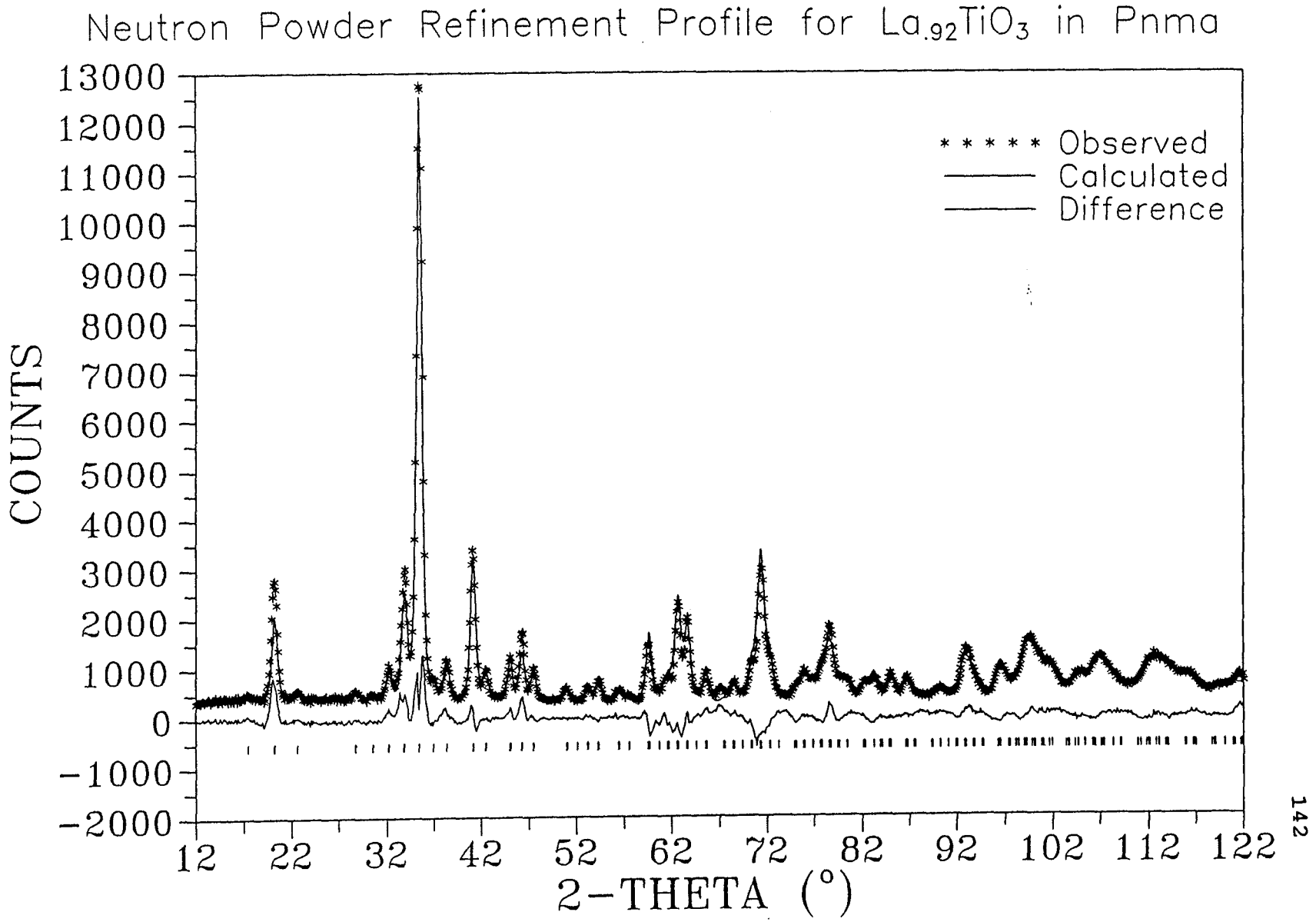
Neutron Powder Refinement Profile for $La_{.92}TiO_3$ in Pnma
COUNTS
13000
12000
11000
10000
9000
8000
7000
6000
5000
4000
3000
2000
1000
0
-1000
-2000
12
22
32
42
52
62
72
82
92
102
112
122
2-THETA (°)
***** Observed
Calculated
Difference